2019-02-27

Carbon Capture and Synergistic Energy Storage: Performance and Uncertainty Quantification

Christopher Stephen Russell
Brigham Young University - Provo

Carbon Capture and Synergistic Energy Storage:

Performance and Uncertainty

Quantification

Christopher Stephen Russell

A dissertation submitted to the faculty of
Brigham Young University
in partial fulfillment of the requirements for the degree of

Doctor of Philosophy

Larry L. Baxter, Chair
Randy S. Lewis
Dean R. Wheeler
Matthew J. Memmott
Joel D. Kress

Department of Chemical Engineering

Brigham Young University

ABSTRACT

Carbon Capture and Synergistic Energy Storage:
Performance and Uncertainty
Quantification

Christopher Stephen Russell
Department of Chemical Engineering, BYU
Doctor of Philosophy

Energy use around the world will rise in the coming decades. Renewable energy sources will help meet this demand, but renewable sources suffer from intermittency, uncontrollable power supply, geographic limitations, and other issues. Many of these issues can be mitigated by introducing energy storage technologies. These technologies facilitate load following and can effectively time-shift power. This analysis compares dedicated and synergistic energy storage technologies using energy efficiency as the primary metric.

Energy storage will help renewable sources come to the grid, but fossil fuels still dominate energy sources for decades to come in nearly all projections. Carbon capture technologies can significantly reduce the negative environmental impact of these power plants. There are many carbon capture technologies under development. This analysis considers both the innovative and relatively new cryogenic carbon capture™ (CCC) process and more traditional solvent-based systems. The CCC process requires less energy than other leading technologies while simultaneously providing a means of energy storage for the power plant. This analysis shows CCC is effective as a means to capture CO_2 from coal-fired power plants, natural-gas-fired power plants, and syngas production plants.

Statistical analysis includes two carbon capture technologies and illustrates how uncertainty quantification (UQ) provides error bars for simulations. UQ provides information on data gaps, uncertainties for property models, and distributions for model predictions. In addition, UQ results provide a discrepancy function that can be introduced into the model to provide a better fit to data and better accuracy overall.

Keywords: cryogenic, carbon capture, uncertainty quantification, energy storage, syngas

ACKNOWLEDGEMENTS

I would like to thank my amazing wife Chantelle and my adorable daughter Nickeline for their continued support and encouragement during these years of study and research. I would like to thank Dr. Larry Baxter for being a wonderful advisor and supporting me through all of our project changes and Dr. Joel Kress for being a great mentor at LANL and helping me navigate career paths. Additionally I would like to thank my parents and parents-in-law for their help and support in my education.

I acknowledge support from the Center for Non-Linear Studies at Los Alamos National Lab (LANL) and from the U. S. Dept. of Energy (DOE) through the Carbon Capture Simulation for Industry Impact (CCSI2) project. This work was supported by the US Department of Energy through the Los Alamos National Laboratory. Los Alamos National Laboratory is operated by Triad National Security, LLC, for the National Nuclear Security Administration of U.S. Department of Energy (Contract No. 89233218NCA000001).

TABLE OF CONTENTS

1 Introduction 1
1.1 Global Energy Demand 1
1.1.1 Growing Energy Demand 1
1.1.2 Renewable Electricity Generation 4
1.1.3 Grid-Scale Energy Storage 7
1.2 Meeting Global Energy Demand 8
2 Energy Storage Technology Reviews 10
2.1 Compressed Air 11
2.2 Molten Salt Thermal Storage 16
2.3 Liquefied Gas Energy Storage 20
2.4 Energy Storage Summary 27
3 Carbon Capture: Cleaning the Current-Generation Power Production 29
3.1 Overview 29
3.1.1 Competing Technologies 30
3.2 Cryogenic Carbon Capture 36
3.2.1 The CCC-ECL Process: Coal-Fired Power Plant 37
3.2.2 Model Validation 43
3.2.3 Validation Results 45
3.2.4 Model Predictions 48
3.2.5 CCC-ECL for Syngas 54
4 Solvent Systems: Improving Decades of Research 62
4.1 Uncertainty Quantification 63
4.1.1 Standard Practice 64
4.1.2 Bayesian Process: Uncertainty Quantification 64
4.1.3 Emulator 66
4.1.4 Discrepancy Function 68
4.2 UT Austin's Independence Model 69
4.2.1 Models and sub-models 70
4.2.2 Methodology 73
4.2.3 Results 76
4.2.4 Summary 80
4.3 CO_2BOLs System 81

4.3.1 Sub-Models 81
4.3.2 Results 84
4.3.3 Summary 90
5 Conclusions 91
5.1 Energy Storage Solutions 91
5.2 Carbon Capture 92
5.3 Uncertainty Quantification 93
6 Bibliography 95

LIST OF TABLES

Table 1-1: Estimated Levelized Cost (2016 $/MWh) 6

Table 3-1: Summary of Energy Demand for Several Technologies 31

Table 3-2: Energy Requirement by Unit for 550 MW_e Coal-Fired Power Plant 48

Table 3-3: Energy Balance 49

Table 3-4: Mass balance (Flow Rates in kg/hr) 50

Table 3-5: Economic Analysis of Process Variations and Resulting Cost of Electricity 52

Table 3-6: Syngas Composition for NETL Cases 58

Table 3-7: Energy Penalties for NETL Cases 58

Table 3-8: Base Syngas Composition 58

Table 3-9: Base Syngas Composition After 90.53% CCC 59

Table 4-1: Tier 1 Parameters 74

Table 4-2: Tier 2 Parameters 75

LIST OF FIGURES

Figure 1-1: Global Cumulative Power of Grid-Scale Energy Storage Systems 7

Figure 2-1: Brayton Cycle for Power Generation 11

Figure 2-2: Process for Advanced Adiabatic Compressed Air Storage 12

Figure 2-3: Compressed Air Energy Storage Process Flow[27] 14

Figure 2-4: Basic Layout of The Solar Two Project in Barstow, CA, USA[40]. 19

Figure 2-5: Simple ES-CCC Process Schematic 23

Figure 3-1: Simplified Schematic of CCC-ECL Process Flow 37

Figure 3-2: N-Pentane Isothermal Residuals (Liquid Phase) 45

Figure 3-3: Butane Isothermal Residuals (Liquid Phase) 46

Figure 3-4: Iso-Pentane PR SLE Residual Plot 47

Figure 3-5: N-Pentane PR SLE Residual Plot 47

Figure 3-6: Simplified PFD of Syngas Treatment Process 57

Figure 3-7: Energy Penalty [MJ_e/kg CO_2] for Different Inlets and Capture Percentages 60

Figure 4-1: Calibrated Predictions of Heat Capacity. 77

Figure 4-2: Calibrated Predictions of Henry's Constant 77

Figure 4-3: Calibrated Predictions of CO_2 Partial Pressure (a) and Loaded Heat Capacity (b). .. 79

Figure 4-4: Partial Pressure Parity Plot. 79

Figure 4-5: Loaded Heat Capacity Parity Plot. 80

Figure 4-6: Uniform Prior Distribution for an NRTL Binary Interaction Parameter 85

Figure 4-7: Posterior Distributions for 7 Key Parameters. 86

Figure 4-8: Bivariate Posterior Distributions for 3 Parameters 87

Figure 4-9: Calibrated Predictions for the Viscosity Sub-Model. 88

Figure 4-10: Calibrated Predictions for the Thermodynamics Sub-Model (PTx Data Shown). .. 89

Figure 4-11: Carbon Capture Percent Distribution from Model Calibration Results..... 90

1 INTRODUCTION

In recent years environmental, economic, and political motivations have led to uncertainty about how to meet energy demand now and in the future. Current energy challenges are diverse and require a multi-faceted approach to successfully meet increasing global energy demands. This research aims to address three issues: how to appropriately incorporate renewable resources into the electrical grid, how to continue using fossil fuels in an environmentally sustainable manner, and how to quickly improve simulations of carbon capture to prepare for pilot plant scale-up. A central focus of this work is the use of carbon capture technologies, primarily cryogenic carbon capture technologies. Cryogenic carbon capture will be shown to be effective energy storage for renewable sources and an efficient solution to clean fossil fuel-fired power plants. Uncertainty quantification is presented as a technique to identify shortcomings in the model and data of carbon capture technologies to speed their development. Section 1.1 discusses the current state of the energy sector followed by an outline and summary of this work.

1.1 Global Energy Demand

1.1.1 Growing Energy Demand

Global energy production and consumption steadily increases due to increasing world population, increasing economic standing (especially in developing nations), and an increasing role of energy in lifestyles. Global primary energy consumption increases are slower than in

years past[1, 2], but electricity consumption continues to grow in both Organization for Economic Co-operation and Development (OECD) countries and, especially, in developing countries. The same analyses predict increasing rates of electrical power consumption well into the future, with potentially large increases to the extent that transportation and space/water heating increasingly use electrical power, as is anticipated by many climate change mitigation scenarios.

New estimates show that global population will reach 9-10 billion people by 2050. The United Nations projects that a majority of this expansion will occur in under-developed and developing countries, which have growing energy demands, specifically electricity[3]. In addition to increasing population, recently improved economic conditions for much of the world's population bring an associated increase in energy demand of all types, including electricity. Since 1981, the global population living in abject poverty has decreased by over 1.13 billion people and from over 40% to about 11% of the world population[4], with about half of the change occurring since 2000. This exceeds the current population of every country except China and India by more than a factor of two.

To sustain this impressive economic improvement will require dramatic increases in energy availability and reliability even if global population were not increasing. According to the U.S. Energy Information Administration (EIA), global electricity demand will increase by 48% from 2012 to 2040[5]. This will result in an increase of current global electrical energy consumption from 160,896 TWh in 2012 to 238,853 TWh in 2040[5]. This will stretch the capability of power generators and transmissions systems well beyond current capacities.

Emerging economies such as China, Brazil, Indonesia, India, and Russia will continue to see increased electricity demand from their escalating middle class populations. According to the International Energy Agency (IEA), OECD countries accounted for 73.1% of the 6,115 TWh of

electricity generated in 1973[6]. In 2010, OECD countries accounted for 50.7% of the 21,431 TWh of global electricity generation[6]. These snapshots of consumer energy demand highlight that energy demands for both developed and developing economies will likely increase in the future, with disproportionate increases occurring in developing economies.

The projected increase in global electricity demand requires more and better base-load and peaking power sources and expanded capacity to meet demand, regulate frequency, and level loads. Environmental, economic, and reliability challenges associated with meeting this demand are formidable. Energy supplies also face natural and anthropogenic threats, the mitigation of which will also require innovation. Much focus in future utility development, regulation, and management will be devoted to securing an inexpensive, consistent power supply. Governments, corporations, and other organizations will struggle to meet future needs without innovative technologies and practices.

Inadequate or unreliable power has both social and economic effects. The two-day blackouts across India in July 2012 disrupted nearly every aspect of life. Facilities that did not operate for two days included hospitals, wastewater treatment plants, traffic lights, trains, businesses, and residential appliances including refrigeration and temperature control systems. Traffic jams, stranded passengers, and general confusion led to human casualty, protest and civil unrest[7]. Similar blackouts, affecting fewer people, have occurred in most regions, including a two-day event in the US and Canada in August 2003. The costs of unreliable electrical power to the US alone have been estimated at $80 billion annually, with a wide range of uncertainty[8], even though the US generates energy more reliably than essentially any other large-scale process. These events illustrate problems that arise with inadequate or unreliable electrical power.

In addition to these issues for grid-scale energy production the transportation sector has very limited options for fuel. Current transportation fuels are ~95%[9] fossil fuels. Vehicles from the nascent electric car industry emit no CO_2 directly, but renewable sources produced only 13% of electricity in the US in 2017[10] and 22% globally[11]. General use of electric vehicles is also quite low with only ~0.3% of transportation sector energy consumption being electric. Gasification and syngas production is an established process for producing both chemical and transportation fuel from solid feedstock. Syngas from biomass can be sustainable and CO_2 neutral, depending on the process by which it is produced[12].

1.1.2 Renewable Electricity Generation

Current trends indicate that renewable energy sources are becoming a larger part of energy production[13]. Increased renewable energy stems from concerns about sustainability and environmental impact along with increasing financial competitiveness and resource depletion. Renewable electricity technologies (i.e., hydro, solar, wind, biomass, geothermal) generate electricity from sustainable resources while producing less carbon emissions than traditional fossil-fuel sources. These environmentally friendly aspects of renewable electricity generation coupled with recent cost reductions establish at least some of these technologies among the most rapidly growing power sources. As of 2015, global wind energy capacity was 414 GW[14]. The global photovoltaic (PV) solar capacity in 2015 was 220 GW with an annual generation of 247 TWh[14,15]. Construction of these renewable energy sources will continue to increase if they prove to be commercially profitable and reliable. The intermittent generation and regional limitations of most renewable energies represent a primary barrier to substantial grid penetration.

Concerns about long-term effects of carbon emitting power sources have propelled investment in non-fossil-fuel-burning technologies. Conventional carbon emitting power sources, such as coal, natural gas, and oil, are abundant, inexpensive, and mature systems. New renewable power sources must compete and operate in a market dominated by these mature technologies. About 65% of the roughly 25,000 TWh of electricity consumed worldwide in 2015 came from coal/peat, natural gas, and oil[16]. By contrast, 22% of electricity generation came from renewables[16].

Relative costs of conventional fossil fuel and new renewable electricity depend on the region, facility age, operation costs, fuel costs, and financing details (Table 1-1). Costs depend strongly on time, especially for some new renewable energy sources, and prices, if not costs, further depend strongly on government regulation. Power supply intermittency and ability to dispatch energy on demand figures prominently in its value, though there are few clear ways to represent this in cost or price structures. These issues complicate economic comparisons as do the cost of capital, finance horizons and mechanisms, installation factors, and a host of similar considerations that affect project economics but vary substantially with project and project sponsor. Despite all of these issues, renewable energy costs have fallen significantly and currently compete in many contexts with some forms of fossil and nuclear energy.

Costs and technologies also depend on usage patterns. A capacity factor indicates the fraction of time the resource is used. Hence, the natural gas combustion turbine and advanced combustion turbine (both at 30%) most commonly supply peak demand while natural gas combined cycle most commonly supplies baseline power. The levelized capital cost indicates the building cost for each MWh of electricity produced. The total O&M indicates the operating and maintenance cost of the plant and the transmission investment indicates the cost of building

infrastructure to supply power to the grid. The total system levelized cost factors all of these costs into a summary cost.

Table 1-1: Estimated Levelized Cost (2016 $/MWh) Comparison of Electricity Generating Sources Entering Service in 2022[17]

Technology	Capacity Factor (%)	Levelized Capital Cost	Total O&M	Transmission Investment	Total System Levelized Cost
Coal 30% with carbon sequestration	85	94.9	43.9	1.2	140.0
Coal 90% with carbon sequestration	85	78.0	43.1	1.2	123.2
Natural Gas-fired					
Conventional Combined Cycle	87	13.9	42.2	1.2	57.3
Advanced Combined Cycle	87	15.8	39.4	1.2	56.5
Advanced CC with CCS	87	29.5	51.8	1.2	82.4
Combustion Turbine	30	40.7	65.2	3.5	109.4
Advanced Combustion Turbine	30	25.9	65.3	3.5	94.7
Advanced Nuclear	90	73.6	24.3	1.1	99.1
Geothermal	91	32.2	12.8	1.5	46.5
Biomass	83	44.7	56.4	1.3	102.4
Wind – Onshore	39	47.2	13.7	2.8	63.7
Wind – Offshore	45	133.0	19.6	4.8	157.4
Solar, Photovoltaic	24	70.2	10.5	4.4	85.0
Solar, Thermal	20	191.9	44.0	6.1	242.0
Hydroelectric	59	56.2	8.2	1.8	66.2

These numbers do not reflect the often-large differences in power generation costs at peak demand compared to those at low demand. The difference in these costs, especially for a utility or other major power producer, can be large.

Renewable electricity generation draws power from natural energy sources, primarily the wind and the sun for new renewables and hydro for most legacy renewable sources. These renewable energy sources have some environmental impacts that compare favorably with fossil energies, especially in the areas of air pollution and CO_2 emissions. Renewable energy

intermittency represents a significant challenge to its most effective use. This challenge increases with increased fraction of intermittent power. In one investigation, electric power generation in the southwestern United States varied month to month and year to year. Over the period of 2004-2006, total energy generation varied from 5,000 GWh to almost 12,000 GWh during 2004 through 2006[18]. However, the most challenging aspects of intermittent energy are the hour-by-hour or minute-by-minute variations in output.

1.1.3 Grid-Scale Energy Storage

Increasing use of intermittent energy supplies, such as wind and solar, escalate the need for energy storage exponentially. Historically, grid-scale energy storage started with pumped hydroelectric systems and grew rapidly through the late 1900's as seen in Figure 1-1.

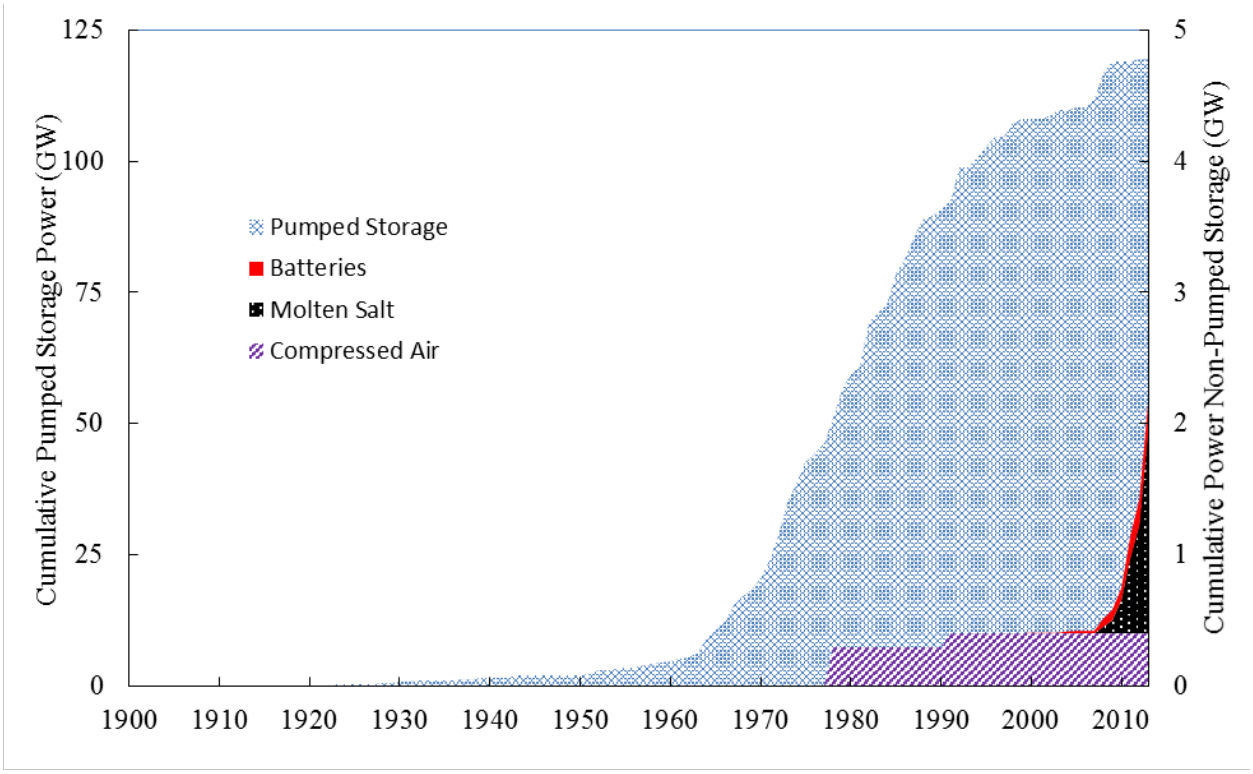

Figure 1-1: Global Cumulative Power of Grid-Scale Energy Storage Systems

Pumped storage accounts for 98.2% of all grid-scale energy storage as of 2013. Pumped storage seems to follow an s-curve with the rate of new installations declining in recent decades. This decline coincides with a rise in contributions from several alternative technologies for grid-scale energy storage: compressed air, molten salt, liquid air, and several varieties of batteries. Interestingly, the two compressed-air energy storage systems account for 22.6% of all non-pumped-storage systems.

Pumped storage systems are generally built with new hydropower installations, and the U.S. Energy Information Agency expects virtually no domestic growth of hydropower installations from 2017-2040[19]. While the outlook for pumped storage appears weak in the US, other countries may become important in continuing the growth of this historically dominant energy storage technology.

With global energy consumption expected to double by 2040, and the weak outlook for pumped storage, energy storage needs will rely, in part, on developing and new energy storage technologies and with increased responsiveness of electricity production. If pumped hydro remains at its current level and energy consumption doubles by 2040, it would result in every other energy storage option increasing at 16% annually. While this growth of energy storage may seem manageable, increasing non-dispatchable renewable energy production increases demand for innovative technologies. In particular, wind energy is expected to grow 9.80% annually to 2040[11] with most wind energy installations directly requiring an energy storage system.

1.2 Meeting Global Energy Demand

To successfully meet the expected growth[5] in global energy demand will require producing more electricity from almost every fuel source. In addition current infrastructure is not

sufficiently robust to handle the intermittencies of some renewable sources efficiently. Facilitating this growth, especially the accelerated growth of renewables, will require grid-level adaptations. This work proposes solutions to allow the grid to efficiently incorporate renewable energy sources, clean current and future fossil fuel-fired power to alleviate environmental concerns, and to quicken the scale-up of these cleaning technologies.

As stated previously, this research aims to address three issues: how to appropriately incorporate renewable resources into the electrical grid, how to continue using fossil fuels in an environmentally sustainable manner, and how to quickly improve simulations of carbon capture to prepare for pilot plant scale-up. Chapter 2 includes a novel analysis comparing synergistic and dedicated energy storage solutions. Synergistic energy storage provides an energy-efficient method of incorporating renewable energy sources into the grid while overcoming intermittency and load-following issues. The cryogenic carbon capture with external cooling loop system is proposed as an energy-efficient synergistic energy storage technology. Chapter 3 includes an overview of current carbon capture technologies with a sensitivity analysis of the cryogenic carbon capture process applied to a 550 MW power plant to address the issue of cleaning current fossil fuel-fired power sources. A novel application of the CCC process to syngas processing and a validation of the CCC process is also included in this chapter. Chapter 4 includes an overview of uncertainty quantification, its application to carbon capture, and how it can quicken development of new carbon capture technologies. Two case studies illustrate its effectiveness and the ability to handle complex models, such as those used for carbon capture, to reduce model uncertainty and improve data acquisition efforts. The novelty of the application of uncertainty quantification to models of this scale is discussed.

2 ENERGY STORAGE TECHNOLOGY REVIEWS

As stated previously, renewable energy sources are difficult to effectively integrate into the current electrical grid. Intermittency and lack of load following often require additional fossil fuel-fired power plants to be constructed as an alternative power source. The primary concern with these intermittencies is day-to-day power supply and demand so long-term storage, frequency regulation, and second-by-second energy storage are not the focus of this chapter. Energy storage technologies can provide a very efficient solution to load following and time manipulation to allow renewable energy sources to be effectively incorporated into the electrical grid.

Several innovative energy storage techniques benefit from integrating themselves into a plant and becoming synergistic. This chapter includes reviews for three energy storage technologies to give background on synergistic systems: compressed air, molten salt, and liquefied gas. These three technologies were chosen because they prominently feature both dedicated and synergistic storage systems. Energy storing cryogenic carbon capture (ES-CCC) is presented as one such technology that provides both carbon capture and energy storage in preparation for a later discussion of ES-CCC's carbon capture capabilities.

Each energy storage technology will first focus on dedicated systems before discussing the equivalent synergistic system. Several metrics are listed for each technology as well as a comparison between the dedicated and synergistic systems. Other reviews compare metrics of

each competing energy storage technology, whereas the novelty of this analysis is the direct comparison of synergistic and dedicated storage technologies of the same type. The primary metric used to compare these technologies is efficiency, i.e. the amount of power that is recovered after being stored.

2.1 Compressed Air

Compressed air energy storage [20] (CAES) is a well-understood and prominent energy storage technology. Compressed air storage installations are large scale and can store energy indefinitely in the form of compressed ambient air. Commercial installations of this technology exist in only a small number of locations, although these power plants have operated for more than thirty years.

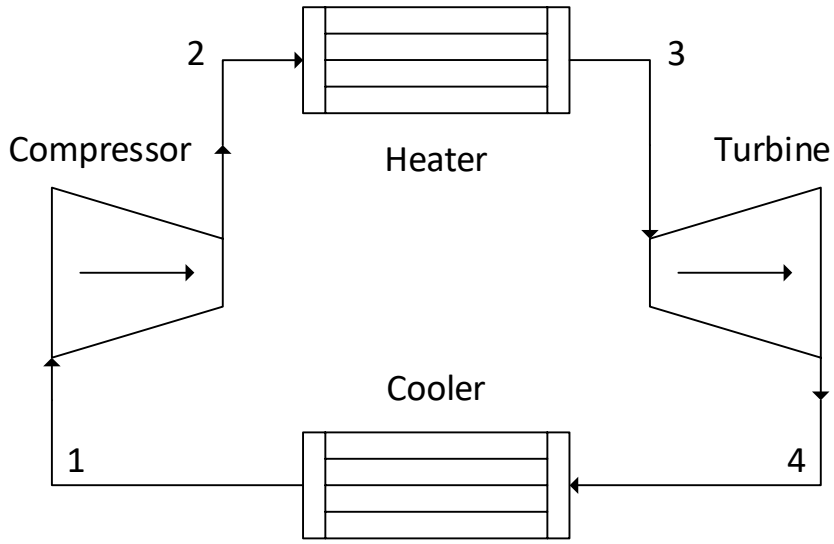

Figure 2-1: Brayton Cycle for Power Generation

When excess electricity is available on the grid, compressed air plants store energy by operating a compressor to pressurize air in underground natural caverns. The compressed air expands through a turbine to recover the stored energy. Compressed air storage is a perturbation

on conventional gas turbine (GT) generation. Compressed-air storage and gas turbine generation use the Brayton cycle, Figure 2-1. A traditional Brayton cycle compresses air adiabatically. The compressed air then moves to a combustion chamber where a fuel combusts isobarically and then expands adiabatically across the turbine.

2.1.1 Advanced Adiabatic CAES

Advanced adiabatic compressed air storage[21] (AA-CAES) is a relatively new technological innovation based on conventional compressed air storage design. Advanced adiabatic design eliminates combustion. Instead, it uses stored thermal energy from the compression of the air to reheat the air upon expansion, Figure 2-2.

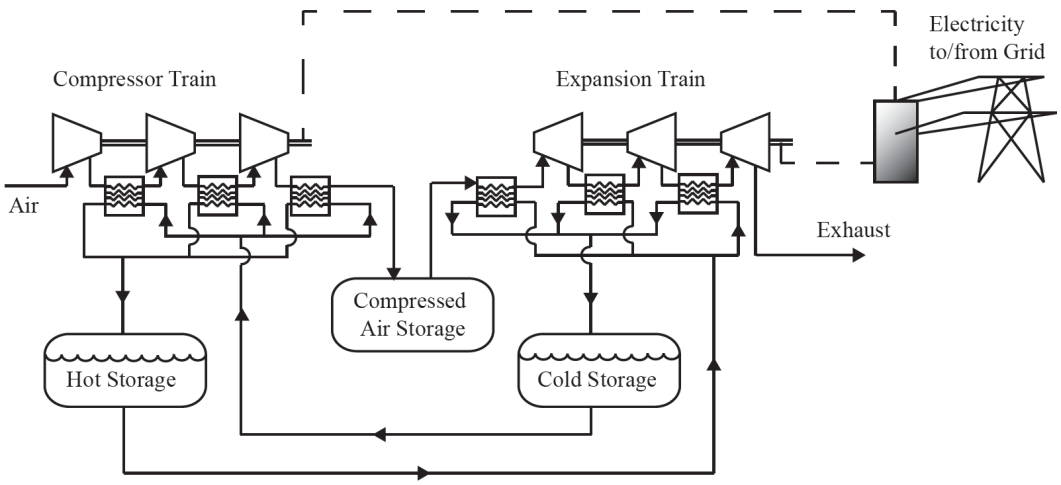

Figure 2-2: Process for Advanced Adiabatic Compressed Air Storage

Air compression increases air temperature. Heat exchangers transfer this energy to a thermal storage container. The compressed air also enters a storage cavern as in conventional compressed air storage. As the air exits the cavern through expansion turbines, the stored thermal energy heats it, usually in a series of expansions.

The advanced adiabatic compressed air storage system reports efficiencies as high as 70-76%, decreasing with increasing ambient air temperature[22, 23]. The Electric Power Research Institute (EPRI) and the US Department of Energy (DOE) report a roundtrip efficiency of 65%[23, 24]. However, capital and maintenance costs can be high for the typical six heat exchangers and two well-insulated thermal storage containers. This equipment also increases pressure loss as the air moves from the compressor train to the storage unit[24].

2.1.2 Isothermal CAES

Isothermal compressed air storage[25] is another modification of traditional compressed air storage technology. Water is injected as a heat transfer fluid to maintain an isotherm during compression and expansion and can possibly increase gas flow during expansion.

This technology is still in early stages of development by companies, such as SustainX [26]. These companies consider manufactured (as opposed to natural) pressure vessels for air storage in some implementations, which would increase pressure ratios and decrease footprints.

2.1.3 Synergistic Compressed Air

Gas turbine combustion[27] uses air pressurized from 40 to 80 bar (Figure 2-3). When coupled with compressed air storage this can lead to an increase in net electrical output and efficiency since the compression step is no longer required. During times of low electricity demand the compression step can store compressed air for use during peak hours at which time the compressor can be shut off, increasing the power output of the plant. This energy can come from renewables that typically have high outputs during off-peak hours, such as wind. Air compression often occurs comparatively slowly, in which case it is closer to isothermal and therefore more efficient than adiabatic compression.

The compressed air enters an underground cavern for storage[28]. These caverns include aquifers, abandoned mines, salt caverns, and rock caverns[29]. However, most natural storage systems cannot store air at turbine pressures without excessive leakage or catastrophic failure, so the stored air is only partially compressed.

The compression step is largely independent of the expansion step and can use excess power from low demand times or from intermittent renewables, as examples. This reduces the parasitic losses associated with traditional gas turbine power generation and places greater generated output to the grid when using partially compressed air from the cavern. This technology can decrease fuel consumption and pollutant generation by up to one-third if the compression energy does not come from the turbine and would otherwise be unusable. Even if the turbine supplies the compression energy, the system stores energy by shifting a portion of the parasitic load to times of low energy demand or cost[30].

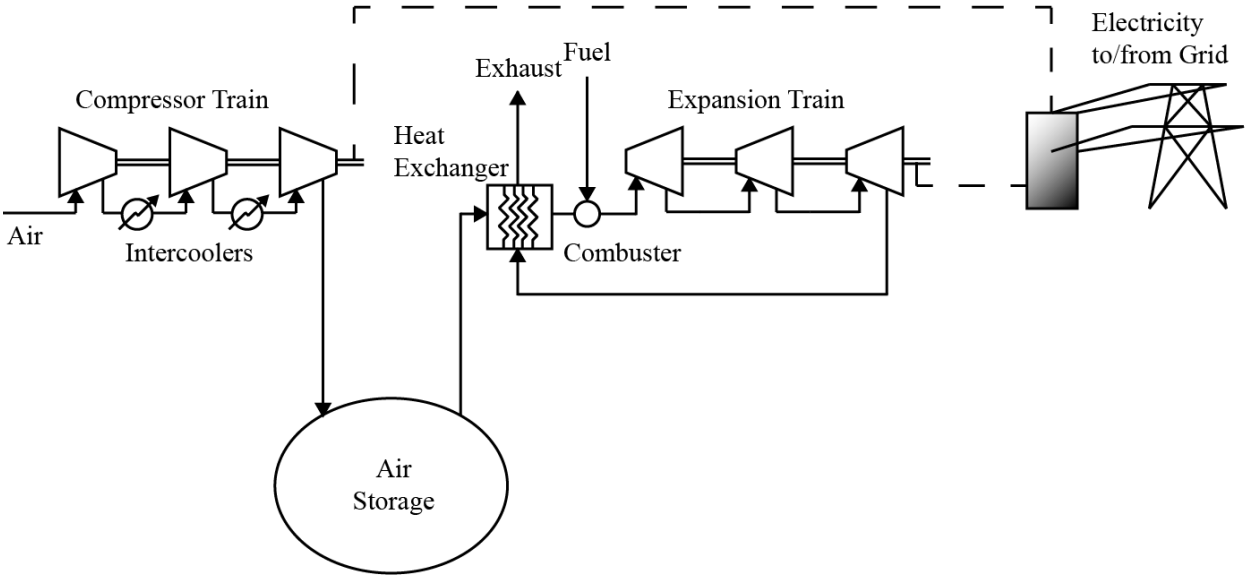

Figure 2-3: Compressed Air Energy Storage Process Flow[27]

2.1.4 Efficiency

Much has been said on measuring compressed air storage efficiency. Convention has been to determine efficiency as the ratio of energy generated by the turbine to the energy and fuel used by the compressor and turbine respectively. Elmegaard and Brix [23] make the distinction that compressed air storage efficiency is a measure of several components given the separate processes of compression, storage, and expansion. They also make the case for storage efficiency to be a real indication as to the overall compressed air storage system efficiency. They report an actual storage efficiency of 29-43% and an overall plant efficiency of 40-57%[23]. Theoretical round trip efficiency for the process is about 72-82%[27, 31, 32]. Energy lost due to leakage and heat loss in the cavern is estimated to be between 4-10% per daily cycle depending on various factors[33].

2.1.5 Dedicated vs. Synergistic Storage

The synergistic system discussed above has many advantages over the dedicated CAES systems. Because the compressors and turbines in the synergistic case would already be purchased as part of the plant, the main cost of CAES would be eliminated. In addition to cost, the necessity for compression means only storage losses affect the synergistic system. This 4-10% loss is a significant energy savings compared to the 18-28% loss of a dedicated system. Synergistic energy storage provides a significant efficiency advantage over its dedicated counterpart without the need for a complex and expensive energy storage system as in the case of advanced adiabatic compressed air.

2.2 Molten Salt Thermal Storage

Thermal energy storage (TES) techniques have been developed to increase efficiency and output of solar power plants. These thermal storage systems allow for excess energy to be stored for periods of low solar power generation. Molten salts are one such method that has been developed to reduce solar power intermittency.

Of the two most common types of solar power plants, concentrated solar power (CSP) and photovoltaic (PV) solar plants, molten-salt storage is typically used in conjunction with concentrated solar plants. Photovoltaic plants convert sunlight directly into electrical current through the photovoltaic effect. Concentrated solar plants, however, concentrate sunlight onto a solar collector in order to generate electricity[34]. There are four main types of concentrated solar power designs: tower, parabolic trough, parabolic dishes, and linear Fresnel systems. These designs can be direct or indirect depending upon the interaction of the solar energy with the heat transfer fluid[35, 36]. Parabolic trough and tower concentrated solar plants are currently the only designs capable of generating greater than 50 MW[34]. Linear Fresnel is another design that utilizes molten salt storage, yet few installations exist and none are greater than 30 MW.

The use of molten salts for thermal energy storage is a relatively new technology with some of the earliest projects with solar starting in 2010[37]. Molten salts are used in conjunction with existing solar power plants to store excess energy, provide energy during periods of low generation, improve overall system efficiency, and reduce capital and operating costs. In operation, molten salts are used as a heat transfer fluid, as a thermal storage medium found exclusively in a thermal storage tank, or both as a heat transfer fluid and as a thermal storage fluid[38]. Tower plants using molten salts as a heat transfer fluid as well as storage medium are

already commercially viable. Parabolic troughs using oil as the heat transfer fluid and molten salts as the storage medium are industrial scale alternatives.

Typical molten salt systems are nitrate eutectics. Their compositions range with the chief components being $Ca(NO_3)_2$, KNO_3, $NaNO_2$, and $NaNO_3$[39-41]. Their operating temperature range is approximately 200-580 °C, while their melting points range from 120-220 °C.

Molten salt energy storage systems use either one or two tanks. Initially, the two-tank system used oil as the heat transfer fluid and molten salts as the thermal storage medium. A common oil for use as a heat transfer fluid is Therminol VP-1, which has a melting point of 12 °C and is thermally stable to 400 °C[42]. However, oils that operate above 400 °C are very expensive. This constrains the Rankine steam turbine efficiency and make it necessary to use fossil fuels to heat the steam to the more efficient temperature[36].

Molten salts are often used in place of oils as they provided a low-cost material with the ability to operate at greater than 500 °C and facilitate higher temperature steam to improve turbine generation efficiency. However, their melting point is much higher relative to oils used for similar operation. This limitation requires additional heating in the system to prevent solidification within piping and storage equipment[42].

When excess energy is available, at times of high solar irradiation for solar plants, the heat transfer fluid cycles through the system. This cycling captures the excess energy that would otherwise be wasted. Insulated thermal storage tanks store this energy. A heat transfer fluid transports energy from the solar concentrator to the tank. Filler material, such as quartz, is often used in one tank systems as they allow for an improved thermocline and less expensive material used overall[43].

Further developments of the two-tank system, such as the 10 MW Solar Two Project shown in Figure 2-4, replaced the heat transfer fluid with molten salts. 1.5 million kg of 60 wt% $NaNO_3$, 40 wt% KNO_3 molten salt is pumped through the tower where it is heated to 565 °C. This particular composition of molten salt has a liquid phase range of 220-600 °C. From the tower, the hot molten salt is pumped to a hot molten salt storage tank. It is released from the hot storage tank to generate steam at 100 bar and 510 °C. Electricity is generated by a Rankine cycle steam turbine. Once the molten salt has passed through the steam generating system, it moves to the cold molten salt storage tank at 290 °C. The two thermal storage tanks are constructed of stainless steel to provide adequate corrosion resistance at 565 °C[40].

In the case of one tank, a thermocline is in use. A thermocline tank has both the warm and cool fluid in the same tank. Thermal stability is maintained by buoyancy forces[36]. Warmer fluid is drawn from the top while cooler fluid is drawn from the bottom. Study has shown a 35% cost reduction resulting from a one tank thermocline system relative to a two-tank system[44].

Adding nanoparticles to molten salts improves the thermal properties of a material by increasing the specific heat, thermal conductivity, and diffusivity while lowering the melting temperature[35]. This addition allows molten salts to store greater amounts of energy in less space, reducing the size and capital cost of equipment. Raising the specific heat of the thermal storage material also allows the system to operate at a higher temperature and greater efficiency[35].

2.2.1 Synergistic Molten Salt Storage

Plants that incorporate molten salt as part of the electricity generation process (Figure 2-4) have synergistic energy storage. For these configurations, the heating of the molten salt is independent of electricity generation, but still central to the normal operation of the plant.

Because thermal energy is converted to electrical energy in the same way, storing energy doesn't lead to conversion losses.

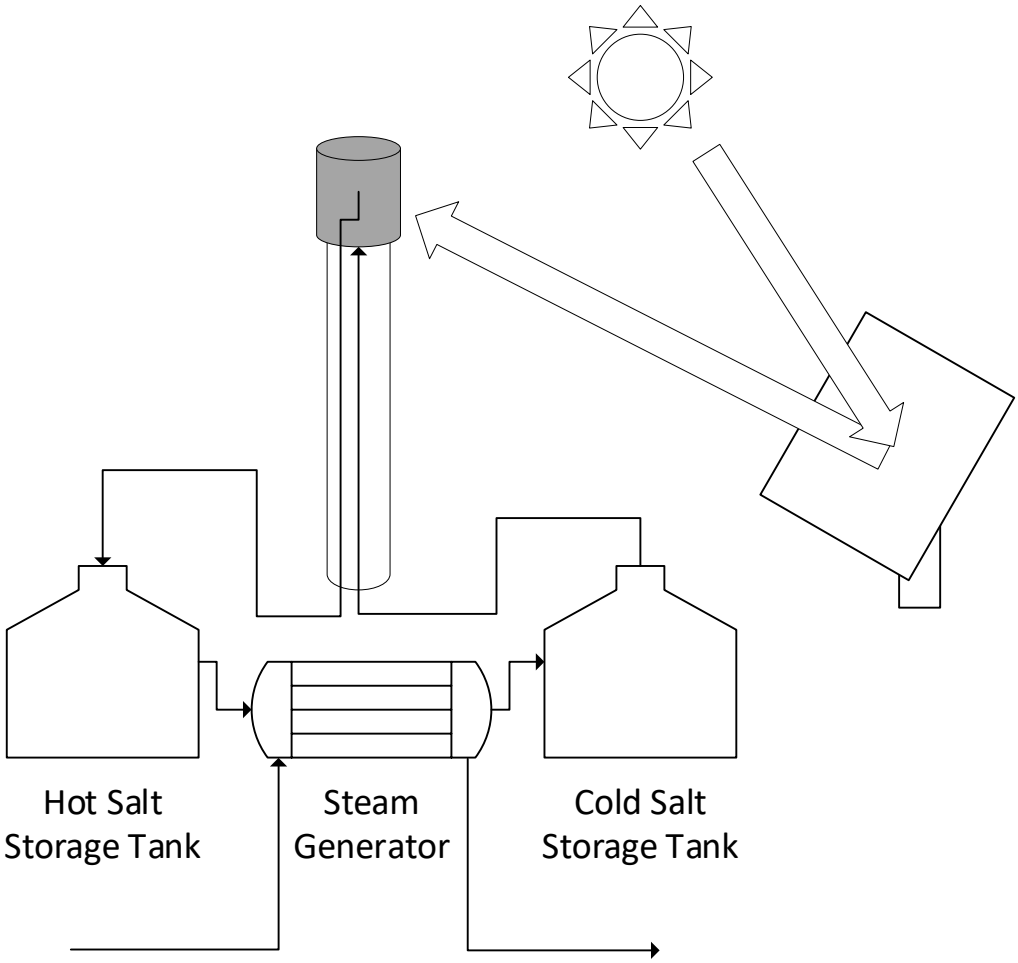

Figure 2-4: Basic Layout of The Solar Two Project in Barstow, CA, USA[40]

Solar plants frequently do not store energy in this manner because times of peak demand usually coincide with peak sunlight. However, most thermal power generation facilities that use a thermal carrier liquid can use this energy storage system. Additional examples of these include nuclear and geothermal power plants. These plants can take advantage of energy storage during low-demand periods. The main benefit to these plants is that they can continuously operate at peak capacity and efficiency using the molten salt to load follow and store energy.

2.2.2 Efficiency

Round trip efficiency definitions vary for concentrated solar power systems. The metric often measured for these applications is the solar-to-electricity efficiency, or the efficiency of the system from solar capture to electricity generation. Hameer et al[45] report a round trip efficiency of 86% for a dedicated two-tank system using thermal oil as the primary fluid and molten salt for storage and molten salt tank losses of 2.5%. Cocco et al[46] report thermocline tank cycle efficiencies of 75% and two-tank cycle efficiencies of 100% with less than 1% annual heat loss for a synergistic thermal oil system.

2.2.3 Dedicated vs. Synergistic Energy Storage

The synergistic molten salt system requires very little additional equipment in the construction of the plant aside from the storage tanks. Energy loss for the synergistic system is limited to heat loss from the storage tanks which is between 1-2.5%. This is a significant energy advantage compared to the 14% energy loss in a dedicated system. The single heat-transfer fluid also saves heat exchangers and the cost of a separate fluid loop.

2.3 Liquefied Gas Energy Storage

Liquefied Air Energy Storage (LAES)[47] is a dedicated storage system that stores energy from electricity in the form of liquid air, which can later be warmed and expanded to generate electricity. The process pressurizes air, cools it to room temperature using ambient sources, cools it to near cryogenic temperatures using refrigeration, and expands it through a turbine to produce a liquid phase (ambient pressures at -196 °C) that can be stored. The air and refrigeration compressors consume nearly all of the energy in the process. Liquefied air storage typically loses 0.05% of the liquid per day to heat leaks and subsequent vaporization.

To recover energy, a pump increases the liquefied air's pressure; the high-pressure liquefied air warms to near ambient temperature and expands nearly 700 fold by volume in a turbo-expander power generator. Heat recovery of the expanded air increases the efficiency of the system.

The process contains only 3 primary material streams: clean air, refrigerant in the chiller, and a waste heat stream. The refrigerant is a closed loop system with insignificant composition change in day-to-day operation. However, both the air and waste-heat streams are open systems, and thus may change constantly during operation.

Inlet air cleaning requires removing water (variable levels), CO_2 (near zero), CH_4 (2 ppm), SO_2 (1 ppm), N_2O (0.5 ppm), particulate (up to 180 ppb), NO_2 (20 ppb), and other species that may cause fouling in the heat exchangers depending on pressure and temperature. Due to the extensive commercialization of air purification for air liquefaction plants, optimized filtering methods have been developed with minimal relative energy impact.

Liquefied air energy storage relies heavily on refrigeration and heat integration design. While refrigerants can be optimized to maintain a small and consistent temperature gradient though the nearly linear temperature decline of the air in gas phase, it becomes difficult to optimize a refrigerant to handle the phase change of air from gas to liquid. Generally, a staged refrigerant, refrigerant with a similar phase change temperature, or an expansion turbine is used to handle the phase change of the air. Due to the extensive commercialization of air liquefaction, high-performance turbines handle the phase change of the air, with minimal supervision or maintenance.

Liquefied air storage requires low-grade waste heat since there is no thermal need for the cryogenic air. Thus, it can be considered as a method not of energy storage, but of electricity

production from low-grade heat. In the absence of waste heat, the process efficiency quickly drops off. The energy evaluation of the technology must consider both scenarios of waste-heat with the likely implementation being an installation with significant waste heat, i.e., coupled with a power plant.

2.3.1 Synergistic Liquefied Gas Storage: Energy Storing Cryogenic Carbon Capture

Energy Storing Cryogenic Carbon Capture (ES-CCC) is a bolt-on process for large stationary CO_2 emitting sources, such as coal-fired power plants[48]. ES-CCC is being researched and developed by Sustainable Energy Solutions LLC, in cooperation with Brigham Young University and currently holds a patent[49]. ES-CCC is an extension of Sustainable Energy Solutions' CCC process to provide energy storage for power plants incorporating Carbon Capture and Sequestration (CCS). Sustainable Energy Solutions began developing the baseline CCC process in 2008, and started expanding to ES-CCC in 2012. This technology is a relatively new energy storage process and most of the work is based on simulations or small- and mid-scale experiments[48, 50-68].

The CCC process consumes 10-15% of a power plant output to separate the CO_2 in the form of a 150 bar liquid stream. The energy storage system works in a similar way to the liquefied air system, with the major exception being the synergistic nature of ES-CCC. When excess electricity is available, a refrigerant used to perform the process is liquefied and stored in the liquid phase. Alternatively, when electricity demand is at peak levels, the refrigerant liquefaction process is turned off, and stored refrigerant is used to maintain operation. This eliminates the parasitic load on the power plant, and thus boosts its electricity output to nameplate value. However, without operating the refrigerant liquefaction during this operational regime, the now-gas-phase refrigerant must be stored. The refrigerant selected for the process is

methane (R-50), which is the primary component of natural gas. Rather than store the methane in gas phase, it is combusted to provide additional power to the electricity grid. Once peak electricity demand is over, the refrigerant loop is closed and additional makeup natural gas is fed into the system to store energy for the next cycle (Figure 2-5).

The ES-CCC system consists of two major subsystems: cryogenic carbon capture (CCC), and energy storage via natural gas liquefaction. The natural gas liquefaction in the energy-storing version of CCC cools the flue gas. Figure 2-5 illustrates this version of CCC.

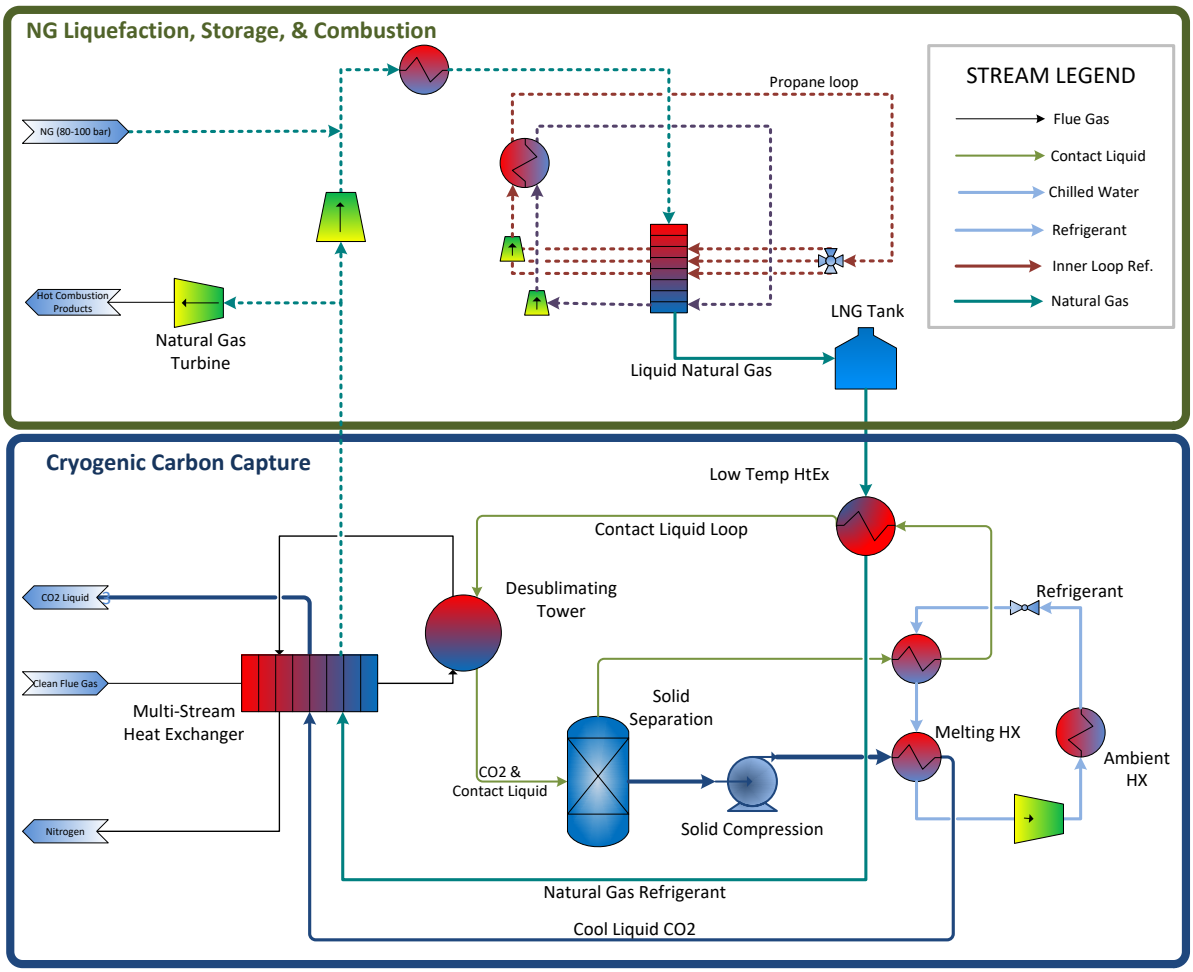

Figure 2-5: Simple ES-CCC Process Schematic

Flue gas that would otherwise be exhausted to the stack enters the CCC process, dries, and cools. After this preliminary cooling, it flows through a recuperative heat exchanger, cooling to -107 °C. Other pollutants, such as Hg, As, NO_2, HCl, and SO_x, condense or desublimate as the flue gas cools to approximately -120 to -130 °C, allowing ES-CCC to exceed the target removal of most criteria pollutants (NO being an exception), mercury, and hazardous gases. The CO_2 desublimates and leaves the light gas stream in the desublimating tower. At these temperatures, the CO_2 removal efficiency ranges from about 90% (-117 °C) to 99% (-132 °C). A solids-handling system pressurizes the CO_2 to at least its triple point and at most the final CO_2 product delivery pressure. The heat exchanger recuperates energy from the sensible heat of the light gas and from the cold solid CO_2 as it warms, melts, and further warms to room temperature. Most of these steps involve accepted industrial processes that would not require additional research to implement; the challenge is to cool the gas efficiently while desublimating the CO_2. Innovative desublimating heat exchangers accomplish this in several different configurations.

Natural gas liquefaction provides one of the refrigerants in the energy-storing CCC process. Once liquefied, the liquid natural gas storage losses from evaporation are less than 0.05% in volume per day[69]. If at any given time more renewable energy is available, this energy can be stored by liquefying natural gas at an accelerated rate. However, when the source of power is no longer available, liquefied natural gas production can stop abruptly using innovative dynamic heat exchangers to manage the transients[67]. When demand reaches peak capacity, the CCC process described above uses this liquefied natural gas, reducing the parasitic load dramatically. Transient heat exchangers[56] mitigate efficiency losses when the LNG production increases or decreases. An additional fluid runs through these heat exchangers that can store and release cooling duty for times of low and high LNG production rates, respectively.

Additionally, the open refrigeration loop allows warm natural gas to be fed into a simple cycle gas turbine. The fastest response to fluctuating demand in power generation is achieved with simple cycle gas turbines. A simple cycle turbine allows for ES-CCC to provide fast response time during peak electricity demand. Simple cycle turbines don't recycle flue gas to recover heat because it would interfere with response speed. However, because the turbine would be adjacent to a standing facility with a boiler, the effluent from this turbine could easily be fed to that boiler allowing combined cycle efficiency at simple cycle cost.

ES-CCC is a beneficial addition to carbon emitting power plants because it allows for carbon emissions to be reduced while providing additional backup power. This added capacity from the natural gas combustion is a powerful way to justify a portion of the equipment costs. Although CO_2 removal can have significant costs, the energy storage system leverages the capital already installed for efficiency and allows higher penetration of renewable energy sources because of improved ramping capabilities.

2.3.2 Efficiency

LAES relies heavily on heat integration for efficiency, with the largest non-recoverable efficiency losses stemming from the compressors, including compressors in the chiller refrigeration unit. The dedicated system lacks heat integration for the cooling and warming steps that are normally present for an air separation unit (ASU). When storing and releasing energy these integration techniques can't be used since the other half of the process isn't running. Thermodynamically, the differences in heat capacity and flow rate in each stream of the several heat exchangers have the potential for significant energetic losses. Most processes use multi-component refrigerants or staged refrigeration loops to best match cooling curves. Highview[47] represents their roundtrip efficiency (AC/AC) to be 70%, with 100 °C waste heat. A published

review of the Highview technology reports 43.3% thermodynamic efficiency with the waste heat provided at 26.85 °C, i.e. ambient air [70]. The liquid air storage tank should have high storage efficiency with minimal thermal losses. Commercialized storage technologies are already employed for storing liquefied oxygen and liquefied natural gas with losses less than 0.05% per day by liquid volume[69]. The cryogenic pump has high efficiency and minimal energy consumption. Similar pump technologies are used for pumping liquid CO_2 for enhanced oil recovery (EOR). The primary difference in technology is the decreased operation temperature depending on the pressure of the storage tank. This is considered a developmental problem rather than one requiring significant technical advancement.

ES-CCC efficiencies have not been demonstrated and may change significantly in application. The efficiency of LNG storage at atmospheric pressure and -164 °C is 99.95% for a 24 hour period using standard commercialized LNG storage technology[69]. Since CCC requires a refrigerant to drive the operation, the primary energy inefficiencies are ascribable to the CO_2 removal process. Thus, the efficiency of ES-CCC is best quantified as the energy difference between optimized CCC and ES-CCC processes. Since transient heat exchangers are very efficient[56, 67] at managing ramping effects of storage the difference is very small. CCC primarily changes for application with ES-CCC by removing the expensive turbomachinery in traditional Compressed Flue Gas (CFG) CCC and driving the entire CCC process with the natural gas refrigerant. The natural gas refrigerant is not the optimal refrigerant for the process, but comes close to matching the thermodynamic cooling curves of the flue gas when used in conjunction with CF_4 (R-14) to transfer heat between the CO_2 melting and CO_2 desublimation.

2.3.3 Dedicated vs Synergistic Energy Storage

LAES suffers from a lack of heat integration which lowers its round-trip efficiency to 43-70%, but has better response times and is minimally restricted by geography. Because the liquefaction step of ES-CCC is independent of the main process loop this process does not suffer such significant efficiency drops. Transient heat exchangers[56, 67] and process integration allow the energy storage piece of ES-CCC to achieve roundtrip efficiencies >90%. The ES-CCC is much more efficient than LAES, has a very small footprint if CCC is already at the plant, and can be almost half the cost of LAES.

2.4 Energy Storage Summary

An increasing rate in the development of energy storage technologies is needed to appropriately balance the timing of energy demand with adequate energy production. It is anticipated[5] that by 2040, worldwide energy production will increase by 48% from 2012 levels with a significant increase in renewable energy sources. Ensuring a stable grid requires energy storage to increase concurrently with renewable sources. Immediate needs exist for grid peak shaving and wind power leveling installations. Future needs will include large-scale load leveling, and on-site solar coupled energy storage.

Commercial technologies already exist, and are used, for grid load-leveling: pumped hydro, compressed air, and flywheels. Due to the excessive cost of flywheels and geographical constraint of pumped hydro and compressed air, it is necessary to develop better energy storage methods. With the eventual incorporation of CO_2 capture technologies on power plants, it becomes increasingly likely that cryogenic carbon capture technologies will become the preferred energy storage method due to high efficiency and low incremental implementation cost. And as thermal solar power becomes increasingly viable, thermal storage technologies will

become increasingly important. Although, thermal solar power will likely be many years in development and implementation, it is only expected to gain a small percentage of the electricity production market due to geographic constraints. Effective thermal storage technologies must be developed in tandem with solar technologies for the successful deployment of large solar installations. A critical component of thermal solar power storage will be responsiveness to rapidly changing light levels.

Utilizing these energy storage technologies in a synergistic manner improves the round-trip efficiency for the energy storage and generally reduces costs when compared to similar, dedicated storage systems. Synergistic energy storage systems also grant peak shaving, load leveling, and response time benefits to plants that allow them to operate without the need for additional support plants. A coal-fired power plant with ES-CCC, for example, would be able to operate as both a base-load power plant and as a rapid-response plant capable of load following. This could eliminate the need for an additional natural gas simple cycle plant to compensate.

Energy storage will not single-handedly solve all the energy problems of the future, but it can help in significant ways. Bringing intermittent energy storage online during peak hours, eliminating the need for backup plants, making a more robust and smarter grid, improving grid efficiency, and other benefits are all possible by incorporating energy storage at a national level.

3 CARBON CAPTURE: CLEANING THE CURRENT-GENERATION POWER PRODUCTION

To address the second issue, how to continue using fossil fuels in an environmentally sustainable manner, this research focused on carbon capture technologies, or technologies that remove carbon dioxide from point emission sources. This chapter places specific emphasis on the CCC process. An overview of the current state of carbon capture is first provided followed by an analysis of and applications of the cryogenic carbon capture system. The overview of technologies and the subsequent description and sensitivity analysis of the CCC system is published work performed together with Jensen et al. [48] This chapter also includes a novel validation of the CCC process model and a novel application of CCC to syngas processing.

3.1 Overview

Carbon dioxide (CO_2) affects the global climate in many ways. Within the USA, the Environmental Protection Agency proposed regulations limit CO_2 emissions from new electricity generation to 1,100 lbs. CO_2/MWh (500 kg CO_2/MWh)[71]. Even new supercritical coal-fired power plants require significant CO_2 capture because their current CO_2 emissions range from 1,800 to 2,000 lbs. CO_2/MWh (820-910 kg CO_2/MWh)[72]. Several technologies can achieve the necessary CO_2 standard. However, while the regulations are obtainable with current technologies, the associated energy penalties and costs of CO_2 capture pose significant, and possibly insurmountable, changes to energy economies. Because carbon capture is much easier at point

sources, these technologies are also being considered or used to capture CO_2 at many other point sources. Miller et. Al[73] discuss how the United States Department of Energy (US DOE) are working on and funding carbon capture projects so that carbon capture technologies can be implemented in less than 10 years. A brief review of some competing technologies is presented as a reference below.

3.1.1 Competing Technologies

CO_2 separation technologies target several industries, including energy production, cement production, aluminum and steel manufacturing, and natural gas production. Several reviews document the energy demands for these industries[74-77]. Technologies for coal-fired power plants generally fall into the categories of oxy-combustion, chemical looping, absorbents, adsorbents, membranes, and cryogenic processes. For most other applications absorbents are the gold standard for carbon capture with fewer competing technologies. The energy penalties vary among the technologies. The minimum work to separate 90% of an initial 15% dry basis CO_2 stream into one stream of pure CO_2 and a second stream dominated by nitrogen is 0.15 MJ_e/kg CO_2. The minimum work of compression from 1 to 150 bar is about 0.22 MJ_e/kg CO_2, for a total of about 0.37 MJ_e/kg CO_2 captured when CO_2 leaves the system at 298.15 K.

Table 3-1 lists energy penalties provided by NETL for some of the previously mentioned technologies. Energy penalties appear in units of MJ_e/kg CO_2 rather than MJ_{th}/kg CO_2 to provide a common basis for comparison, though several technologies consume primarily heat instead of electricity. The energy penalties presented indicate the equivalent amount of electricity consumed, regardless of whether the energy is actually electricity, heat, or a combination of each. Some plant integration steps unique to cryogenic systems can reduce the cryogenic carbon capture penalty further but are not included here. Here we focus on the predictions for a purely bolt-on system

with no integration. The energy demands for carbon capture vary widely among published reports. The numbers provided below come from the most detailed public information and follow the same procedures, with the same assumptions, as are used in this project.

Table 3-1: Summary of Energy Demand for Several Technologies

Process	Energy Penalty [MJ_e/kg CO_2]
PC-2012 Amine	1.143[78]
PC-Sorbent	1.135[78]
PC-Membrane Based	0.897[78]
SC/ITM Oxy-combustion	0.967[79]
Ideal Power Penalty	0.381[78]

3.1.1.1 Oxy-combustion

This method of CO_2 management uses a pre-combustion, cryogenic air separation unit that separates oxygen to combust with coal, resulting in nominally pure combustion products, CO_2 and H_2O. The resulting flue gas cools, condensing H_2O, and then nominally pure CO_2 is pressurized and sequestered or used for enhanced oil recovery. One full-scale power plant using this technology remains in consideration at White Rose (UK) while other major oxy-combustion projects in the US and Europe lost support for a variety of reasons. Hurdles for widespread adoption of oxy-combustion include its high energy penalty due to the extreme, low temperatures (~73 K) required for cryogenic distillation of O_2 from air[80]. The resulting energy penalty is in the range of 0.97-1.5 MJ_e/kg CO_2 captured[79, 81]. There is little expectation for reducing the energy

penalty due to the constraints in the air separation unit with similar molecular weights and vapor pressures of N_2 and O_2.

3.1.1.2 Chemical Looping

Chemical looping poses a similar approach to CO_2 management, but oxygen is introduced as part of an oxidized metal, such as iron titanium oxide[82], instead of as a gas. Oxygen, typically from air, binds to the solid metal carrier in a fluidized bed, and then the oxidized solid metal flows to a second fluidized in which it reacts with fuel to reduce the metal oxide and oxidize the fuel. The reduced solid metal returns to the first fluidized bed to be re-oxidized[83]. The combustion products undergo treatment similar to those of oxy-combustion. Some of the most significant concerns with the chemical looping include the effects of thermally cycling the oxidizing metal carrier. Deactivation with use and entropy losses due to heating and cooling of the solid particles significantly affect the energy penalty. While chemical looping systems exist at atmospheric conditions, energy penalties for these systems were not found in literature and have not been provided in this review. The energy penalty associated with carbon capture by pressurized chemical looping is less than if it were applied to the near atmospheric combustion of this study's base power plant. Disregarding the energy for compression, the energy penalty range is 0.2-0.5 MJ_e/kg CO_2 captured when applied to high-pressure combustion systems[84, 85]. Current research and development includes work at the National Carbon Capture Center on a 150 kW_e equivalent system[86]. NETL provides a summary of several other chemical looping projects[87]. Because chemical looping requires replacing most of an existing power plant, chemical looping usually competes better as an option for new installations rather than as a retrofit option.

3.1.1.3 Absorbents

Amine scrubbing processes are by far the most widely used form of CO_2 removal technology and have decades or industrial experience[88]. They are commercially available for multiple applications. Amine sorbents bind to the CO_2, removing it from the process stream. The data from several literature sources show a large variation in energy penalties despite similar sorbent composition. They range from 0.97-4.20 MJ_e/kg CO_2[88-97] depending on the power plant and the design of the system. Generally, NETL reports an amine carbon capture system to have an associated energy penalty of 1.3 MJ_e/kg CO_2 captured[98]. Variations on compressors, pressures, percent sorbent, and the sorbent composition used are all major contributors to the energy penalties experienced by these processes[93]. A major benefit of this system is that it is a very mature system, at least in its traditional uses in natural gas conditioning[88]. It is also commercially available for power plants, although many absorbents are not past the pilot scale. SaskPower's Boundary Dam[99] integrated Carbon Capture and Sequestration project in Canada is the largest and first project of its type to demonstrate post-combustion capture on a commercial coal-fired power plant. The repowered 110-120 MW_e power plant can produce about one million tons of captured CO_2 per year, about 95% of its total output, much of which supplies enhanced oil recovery at the Weyburn oil field. It uses an amine-based solvent developed by Cansolv, a wholly owned subsidiary of Shell Oil Co. Additionally, a Southern Company is constructing a Selexol process for the full-scale Kemper power plant[100] (USA). Some drawbacks include the size of the process as well as the toxicity of the chemicals and the energy cost to the system. Other amine-type sorbents include Fluor's Econamine system, MHI's KS-1 solvent, and mixtures of primary, secondary, and tertiary amines. These sorbents, while differing from each other, have approximately similar energy penalties to more traditional MEA sorbents.

Other types of sorbents, such as Opticap by B & W, have many drawbacks similar to those mentioned for amines, but additionally have far less research supporting them and are not as commercially available. They are, however, sometimes more efficient as shown by a comparison conducted at NCCC, where Opticap proved significantly more efficient under similar circumstances as MEA[92].

3.1.1.4 Adsorbents

Due to the physical attraction between CO_2 and other species, adsorbents find some uses for CO_2 capture. Typical CO_2 adsorbents include zeolites, molecular sieves, and activated carbon. These preferentially adsorb CO_2 from air-fired combustion products. Once the adsorbent saturates with CO_2, it generally regenerates with a pressure and/or temperature swing. The energy penalty of adsorbents depends primarily on the energy required for the cyclical change in conditions and is in the range of 2.0-5.6 MJ_e/kg CO_2 captured[88, 101]. More advanced adsorbents remain under development in several research programs.

3.1.1.5 Membranes

Membranes provide an alternative to chemicals. Membranes can either provide pre-combustion enrichment of O_2 or post-combustion CO_2 separation from a flue gas. CO_2 penetrates the membrane faster than other species, specifically N_2. The membranes are commonly made from polymers[102] and are sometimes made from other materials such as palladium[103]. The membrane selectively separates components in the stream, specifically the CO_2 molecules. Testing of membranes remains at small scale compared to amine processes. The distinct advantage they have is the absence of toxic chemicals. Membrane separation requires replacement membranes[104] as

well as significant pumping power[105], the latter resulting in energy penalties within the range of 0.95-1.9 MJ_e/kg CO_2 captured[103, 106]. They also struggle to produce high purity CO_2.

3.1.1.6 Cryogenic Processes

Cryogenic technologies come in several forms, including the thermal swing process, inertial carbon extraction system, and the cryogenic carbon capture with external cooling loop (CCC-ECL) system also referred to as ES-CCC discussed previously.

A thermal swing process freezes CO_2 as a solid directly on the surface of a heat exchanger. The heat transfer degrades with time as solid CO_2 fouls the surface. At some point, a second parallel heat exchanger begins processing the stream while the first warms and regenerates[107]. In the case of 90% CO_2 capture from a coal-fired power plant, Pan et al. report that the process energy penalty is 1.18 MJ_e/kg CO_2[108]. Significant energy losses occur with the temperature swing of the heat exchanger. In addition, heat transfer rates reduce as CO_2 solids form on the heat exchanger surfaces. The continual handling of CO_2 solids is a major hurdle for adoption common among all of the cryogenic processes. Mechanical cleaning provides one means for handling the solids formation. While Alstom has generally been interested in this basic process, Shell has also investigated similar processes and shown good agreement between predictions and experimentation[109]. Alstom has slowed the development of the thermal swing process because of minor energy penalty improvements and major capital costs compared with conventional amine systems.

Inertial Carbon Extraction System, an expansion process, forms solid CO_2 without any of the surface fouling issues[110]. Flue gas is expanded through a nozzle, and solid CO_2 particles form with the heat transfer coming from expansion rather than a surface. A cyclone separates the

gas/solid stream. The design, operation, and maturity of this process are significant obstacles to commercialization.

The CCC-ECL[48] likewise operates with the formation of CO_2 solid particles at cryogenic temperatures. The CCC-ECL removes up to 99+% of the CO_2 from flue gas in a continuous process while maintaining a low energy penalty of 0.74 MJ_e/kg CO_2. The technology works by cooling the flue gas to low temperatures, removing water before reaching 273 K, and passing the gas through patented desublimating heat exchangers at temperatures near 150 K. This causes desublimation of the CO_2 to occur, leaving solid CO_2 in a slurry. The solid CO_2 separates from the contact liquid and melts under pressure as it warms back to room temperature. The advantages of this system include low energy penalty, grid-scale energy storage potential, process simplicity, low cost, multipollutant capture, and lack of toxic chemicals.

CO_2 solids formation is the major technical problem with this technology. This has the potential to plug and foul heat exchangers and otherwise complicate the process. Sustainable Energy Solutions (SES) has patented three heat exchangers that operated at steady state with no compromise in performance when treating solids-forming fluids. With lab-, bench- and skid-scale validations completed at scales up to 1 ton of CO_2 per day, the technology is approaching pilot-scale in its development path. Process simulations using both Aspen Plus™ and an in-house SES code predict very similar results that compare favorably with alternative technologies. This section presents simulation results with Aspen Plus™ using the Peng-Robinson equation of state. The Gibbs energy and enthalpy of solid formation of CO_2 are adjusted to match SLE data.

3.2 Cryogenic Carbon Capture

While all of the mentioned carbon capture technologies show promise, this work focuses on the cryogenic carbon capture (CCC) process. This sub-chapter begins with an in-depth

walkthrough of the CCC-ECL process to describe the important streams and unit ops in the process. An outline of the techniques used to validate the model is then included with the results from the validation following. These earlier sections serve to present the model and its accuracy and are followed by full-scale model results and a novel application of this process to syngas processing.

3.2.1 The CCC-ECL Process: Coal-Fired Power Plant

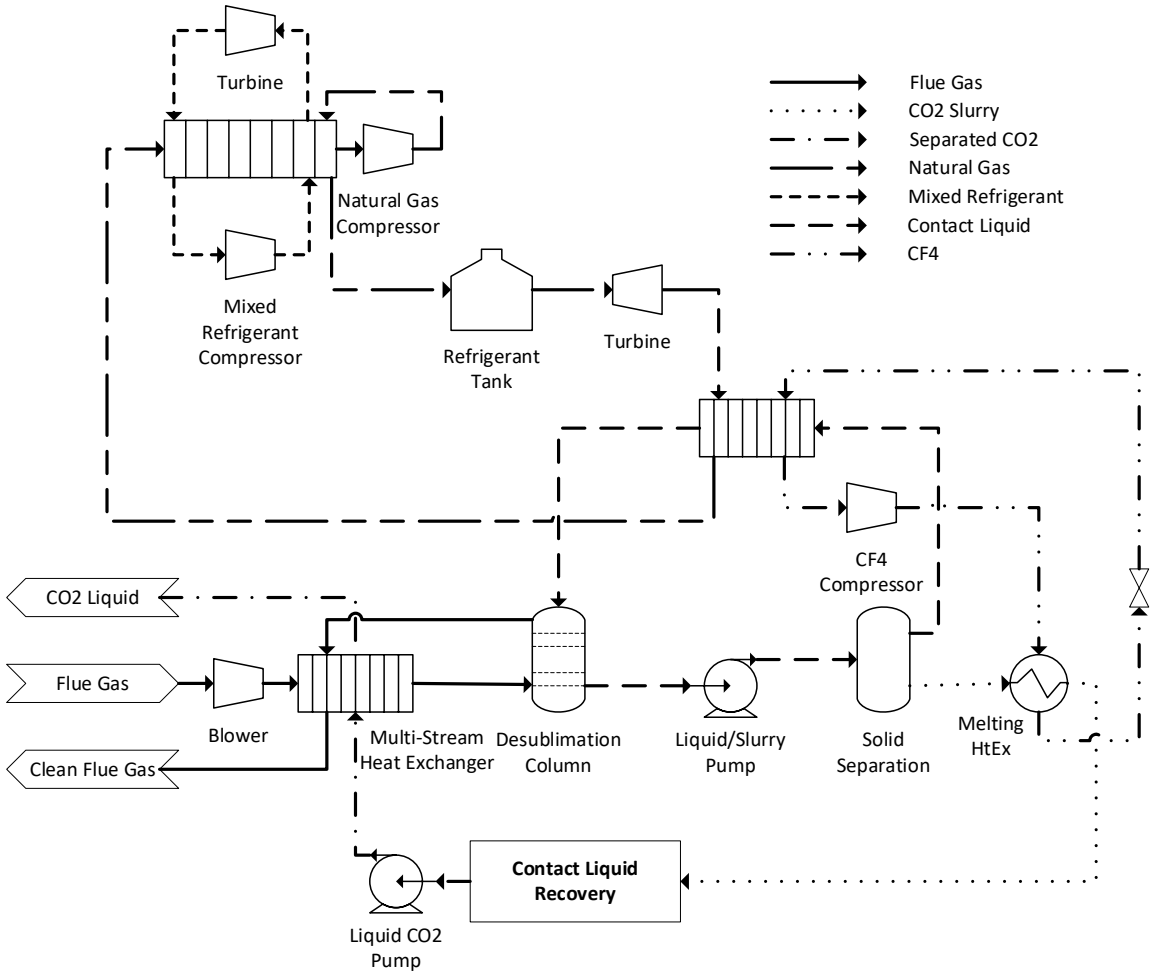

Figure 3-1: Simplified Schematic of CCC-ECL Process Flow

The CCC process provides a retrofit option to remove 90+% of the CO_2 from the flue gas of a coal-fired power plant. The following analysis is an Aspen Plus model which assumes a 550 MW_e net output prior to addition of CO_2 capture based off of an NETL base case[78].

The cryogenic carbon capture cools the treated power plant's flue gas to 175 K. The CO_2 in the flue gas forms solid particles as the flue gas further cools to 154 K in a staged column with direct cryogenic liquid contact. The clean flue gas warms against the incoming flue gas and vents to the atmosphere. The CO_2/contacting liquid slurry undergoes filtration and subsequently the nearly pure solid warms to 233 K and provides a CO_2 rich product. The CO_2 liquefies and leaves the process prepared for enhanced oil recovery (EOR) or sequestration. All contacting liquid streams cool and recycle back to the staged column. An internal refrigeration cycle with CF_4 transfers heat from melting CO_2 to desublimating CO_2. An external cooling loop of natural gas provides the additional heat duty to operate the cryogenic process. The streams and equipment discussions appear separately below. Figure 3-1 shows a simplified process flow schematic.

3.2.1.1 Flue Gas

This analysis assumes the feedstock has passed through a flue gas desulfurization unit (FGD). The CCC process has demonstrated potential as a SO_x, NO_x, Hg, PM_{xx}, and HC removal device as well as a CO_2 mitigation system[111], and this has been demonstrated many times to be very efficient, but the focus here is on CO_2. The flue gas from the FGD includes 2.4% O_2, 68.08% N_2, 13.53% CO_2, 15.17% H_2O, and 0.82% Ar at 330.15 K and 102.042 kPa. Cooling the gas to 290 K condenses approximately 90% of the water. To overcome subsequent pressure drops, a blower pressurizes the flue gas to 127.6 kPa. The flue gas cools to near 273 K and regenerating mol sieve beds remove the residual water to ensure no ice formation as the flue gas cools in a multi-stream heat exchanger to 175 K. These beds are assumed to be a negligible energy cost since

most of the water condenses before the flue gas enters the beds. The cooled flue gas enters the bottom of a 10-stage desublimating column and bubbles up through the tower while being cooled to 154 K by direct contact with a counter-current contacting liquid. The cleaned flue gas leaves the top of the heat exchanger with less than 10% of the incoming CO_2. It is possible to capture 99+% CO_2 with colder temperatures (144 K), and experiments and theory demonstrate this. However, this simulation uses the DOE benchmark of 90% CO_2 capture. The separated gas recuperatively warms against incoming flue gas. Before the light gas stream returns to the stack, it augments an evaporative cooler to cool process water to near freezing temperatures.

3.2.1.2 Contact Liquid

The contact liquid is in a closed loop with minor losses into the CO_2 byproduct and the light flue gas. In general, contacting liquids should have low vapor pressures to decrease losses through evaporation and otherwise be environmentally and physically benign. The contact liquid prevents CO_2 solids from forming on surfaces and greatly simplifies solid CO_2 transport as a slurry, thus preventing process freeze up. At its coldest temperature of 154 K, the contact liquid enters the top stage of a desublimating column and cools the flue gas through direct contact, leaving the bottom stage as a slurry with solid CO_2 entrained in the flow. A pump pressurizes the slurry prior to entering a solid-liquid separator. The separator consists of an auger-driven continuous filter press. The bulk contact liquid, now free of solids, re-cools against a closed-loop refrigeration system in preparation to reenter the desublimating column. Contact liquid recovered from the CO_2-rich stream returns to the process. To counter the minor losses, a makeup stream of pressurized contacting liquid cools from ambient temperature.

3.2.1.3 CF_4 Refrigeration

The CF_4 refrigeration loop moves the cooling duty of melting CO_2 to the colder temperature of desublimating CO_2. After condensing against the melting CO_2, and some sub cooling, it splits into five streams, each expanded by a valve to a different pressure defined by the stage of the CF_4 compressor to which it will return. This produces a stepping effect in the heat exchanger that overcomes entropy losses against contact liquid and other streams undergoing sensible heating/cooling.

3.2.1.4 CO_2-Rich Product

The CO_2 separates from the slurry at the bottom of the desublimation column in a hydrocyclone followed by a continuous press filter. After filtration, the CO_2-rich product is 93.3% CO_2 and warms and melts against condensing CF_4. After warming against the flue gas to 233 K, the CO_2-rich stream enters a contact liquid removal process for final separation (99.2% CO_2 purity). As part of the contact liquid removal, the CO_2-rich stream warms and flashes to remove the remaining contact liquid. The CO_2 vapor warms and recompresses before liquefying against the vaporizing CO_2-rich stream. After liquefaction, a liquid pump pressurizes it to 100 bar with cooling duty once again recovered before leaving the process for EOR or sequestration. Some studies suggest that a higher discharge pressure may be necessary[112-114], which case is investigated in the sensitivity analysis.

3.2.1.5 External Cooling

Even with significant heat integration, the CCC-ECL process requires additional refrigeration. Natural gas acts as a refrigerant due to its reasonable pressure/temperature refrigeration capability, high maturity and availability of compression, and its potential to enable

energy storage. It is nominally composed of 95% CH_4, 3% C_2H_6, and 2% C_3H_8. The natural gas liquefies and cools to 179 K before expanding in a turbine to 1,145 kPa resulting in a temperature of 153 K. The expansion vaporizes a significant fraction, 25.4%, with the remaining natural gas vaporizing to cool contact liquid in the CCC-ECL process for subsequent CO_2 desublimation. This expanded natural gas is the coldest temperature achieved in the CCC-ECL process. The natural gas recuperatively warms against incoming natural gas before being compressed to initial conditions. A mixed refrigerant loop supports the natural gas liquefaction and comprises nominally 4.2% CH_4, 84.5% C_2H_6, 2.8% C_4H_{10}, and 8.5% iso-C_5H_{12}. Because of the heavier hydrocarbons in the mixed refrigerant, the compressor intercoolers must have a phase separator, and a pump removes and pressurizes the liquid. Alternatively, the recirculating natural gas stream could be conditioned such that no liquids condense to simplify the compressor operation.

3.2.1.6 Pressurization

The flue gas blower is a single-stage compressor in Aspen Plus. The CF_4, natural gas, and mixed refrigerant compressors are 8-stage compressors with intercoolers after each stage of compression. The CO_2 vapor compressor is a single-stage compressor with no after-cooler. Compressor intercoolers have a 5 kPa pressure drop per pass, greatly affecting the efficiency of the lowest-pressure stages. Compressors operate with 90% polytropic efficiency, typical of commercial guarantees for such equipment at this scale. Compressor energy consumption is the primary energy demand in the CCC-ECL process, and thus under great scrutiny.

3.2.1.7 Heat Exchange

Brazed-plate heat exchangers are the primary heat exchange in the CCC-ECL system. They operate with a 1 K minimum internal temperature approach. The melting CO_2 heat exchanger is

similar in design to a jacketed, stirred tank with the CF_4 condensing in the jacketing tubes while the solid melts and is stirred on the inside of the tank. A conservative approach simulates this as a co-current heat exchanger with 1 K approach temperature on the exiting streams. A full-scale counter-current implementation of the melting heat exchanger would have higher efficiency.

Other, more traditional heat exchangers provide compression inter-stage cooling and water cooling. Basic compressor inter-stage coolers are shell and tube heat exchangers with a minimum internal approach temperature of 5 K, though brazed-plate systems would increase efficiency decrease cost. The evaporative cooler is a 10-stage cooling column. All heat exchangers have at least a 5 kPa pressure drop per pass. Designs from Chart Energy and Chemicals suggest pressure drops ranging from 2 kPa to 19 kPa and these are included in the sensitivity analysis.

A 10-stage desublimation column uses a series of Gibbs reactors in the simulation, allowing solids formation at each stage. The desublimation column has 5 cm of liquid height per stage, resulting in a 0.37 kPa pressure drop per stage. As an alternative to a desublimation column, experimental results on a desublimation spray tower have improved efficiencies for heat and mass transfer. Up to 96% CO_2 capture has been demonstrated and predictions of performance are within 2.3%[115].

3.2.1.8 Solid Separation

The CO_2 solids separator is a combination of a hydrocyclone, to concentrate the solid CO_2 particles, followed by a continuous press filter, removing contact liquid down to 6.7%. The press filter captures 100% of the solid CO_2. This does not take solubility into account, which may increase the concentration of CO_2 in the recycled contact liquid, but this will simply recirculate and should not affect energy or cost. It may help reduce viscosity.

3.2.1.9 Turbines

The two expansion turbines handle vapor-liquid phases. Turbines have 92% isentropic efficiency. The turbines operate at temperatures ranging from 154-195 K and expand the hydrocarbon liquids with a portion of the stream vaporizing. LNG operations employ cryogenic hydraulic turbines that operate at nearly the same conditions and on the same scale[116] as those in this model. Valves could replace the turbines to reduce capital expenditures with only a 2.4% increase in energy demand.

3.2.2 Model Validation

To further validate the full-scale CCC-ECL simulation, model predictions were compared to vapor-liquid and solid-liquid equilibrium data. Several equations of state (EOSs) were analyzed including the Peng-Robinson (PR), Predictive Soave-Redlich-Kwong (PSRK), and Non-Random Two-Liquid (NRTL) EOSs. Aspen Plus® v10 was used for all simulations. Data were taken from DeChema[117] and NIST databases and used for model comparisons. The full-scale model uses the PR EOS.

3.2.2.1 Vapor-Liquid Equilibrium (VLE) Comparison Setup

The process model includes a feed liquid and feed vapor stream that enter a flash drum. A vapor and liquid stream exit the flash drum. Sensitivity blocks changed flow rates and compositions for different components and CO_2. The sensitivity blocks used input conditions from the data for each data set to calculate the resulting equilibrium. Flash drum temperature was fixed based on the data value with no pressure drop. The pressure of both feed streams was also fixed based on the data input via the sensitivity block and a calculator block. This setup should produce an exact reproduction of the inlet streams as the outlet streams if the model matches the

data perfectly. Since the VLE data came from systems at equilibrium, deviations are therefore assumed to come from the model. In addition to the composition, temperature, and pressure the fugacity or activity coefficient values were also collected. The each data set was used in the simulation for each of the three EOSs. In some cases Aspen's convergence errors necessitated running individual points through the simulation for more accurate results. In this circumstance all values were specified using the stream inputs and the calculator block instead of the sensitivity block.

3.2.2.2 Solid-Liquid Equilibrium (SLE) Comparison Setup

The process model includes a feed liquid and feed solid stream that enter a Gibbs reactor. The Gibbs reactor accommodates solids formation, which is otherwise impossible in a standard flash drum, heat exchanger, or any other unit operation in this and most other commercial simulators. SLE data include liquid composition and temperature. Rarely is pressure included in the reported data since SLE behavior exhibits essentially no pressure dependence so long as no vapor phase is present. A sensitivity block at a fixed pressure determines the liquid feed conditions. The solid feed stream is pure CO_2 at the same conditions as the liquid stream set via a calculator block. The Gibbs reactor has no pressure drop and assumes that only CO_2 is capable of forming a solid when water is absent. The temperature of the Gibbs reactor is set to the temperature of the SLE measurement while the two feed streams have a temperature set 1 °C higher. This avoids any vaporization due to mixing in the Gibbs reactor, which is observed because the liquid stream is at the bubble point. Like with the VLE simulations, in some cases, data points were run individually due to Aspen convergence issues. These runs had inputs set via stream inputs, unit op inputs, and calculator blocks.

3.2.3 Validation Results

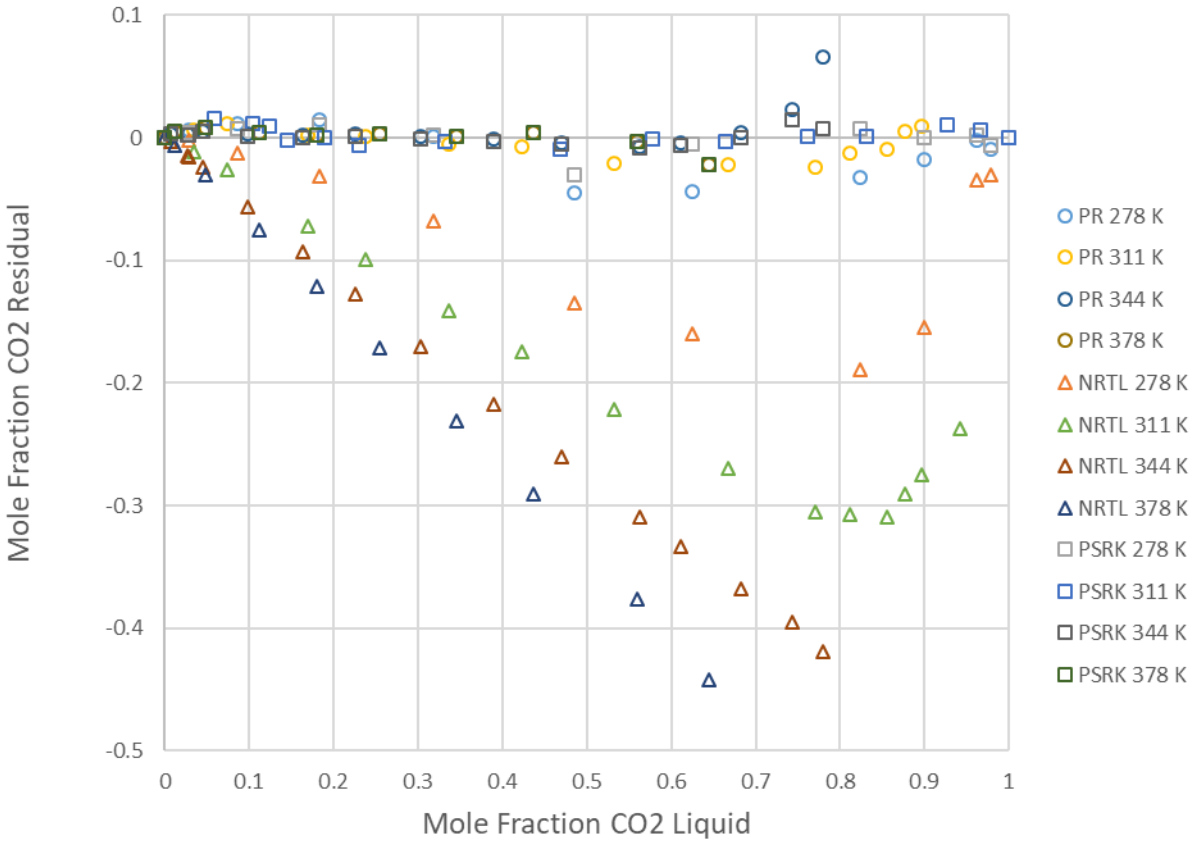

Figure 3-2: N-Pentane Isothermal Residuals (Liquid Phase)

Figure 3-4–Figure 3-5 display the difference between predicted and measured results in the form of residuals ($x_{measured} - x_{predicted}$) for liquid CO_2 mole fractions. VLE results are displayed for varying mole fractions and temperatures while the SLE results are a function of temperature. The Aspen simulations use the PR EOS, which provides accurate estimates of solid, liquid, and vapor equilibrium in this system. In these figures, PR's performance is compared to two other EOSs.

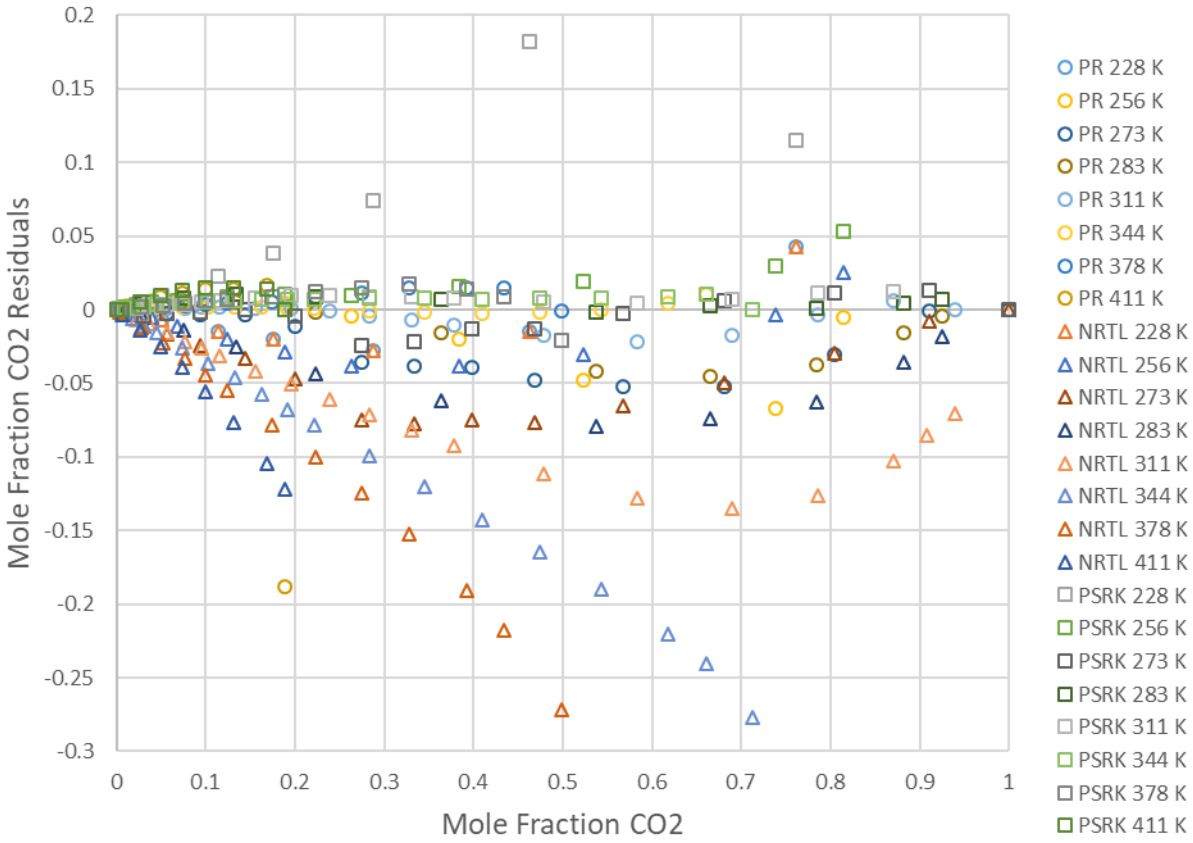

Figure 3-3: Butane Isothermal Residuals (Liquid Phase)

The isothermal residual plots for the liquid phases look favorable for both the PR and PSRK EOSs aside from some outliers. The NRTL EOS struggles for most of the range. The PR EOS also performs almost perfectly in SLE saturation point predictions for both iso-pentane and n-pentane. These results show the accuracy of the PR EOS for the Aspen simulation.

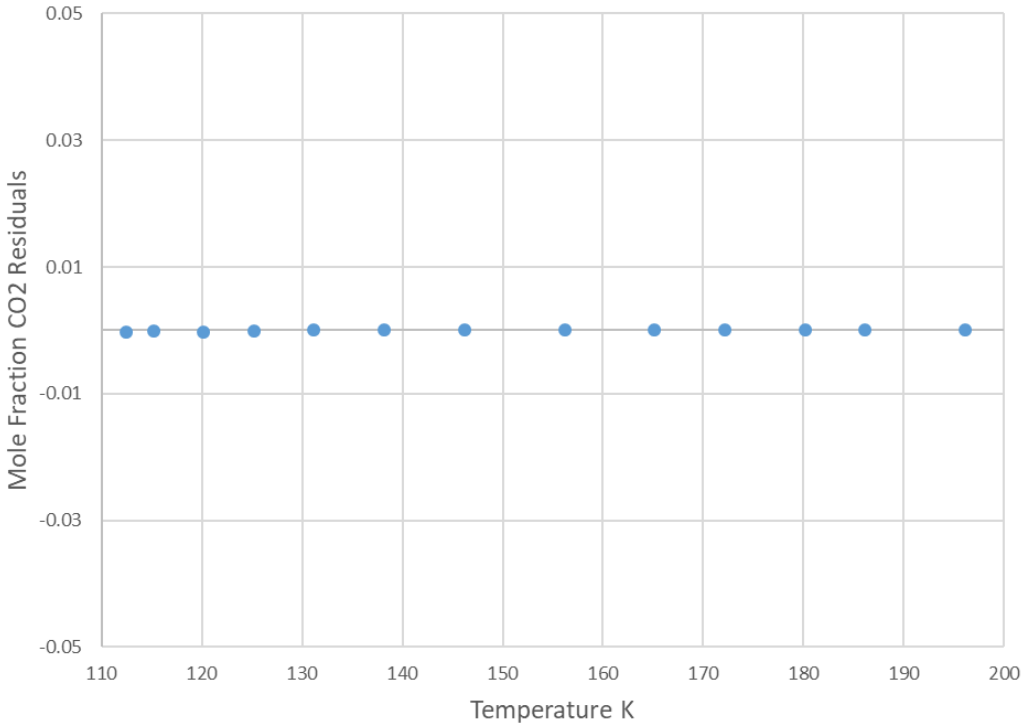

Figure 3-4: Iso-Pentane PR SLE Residual Plot

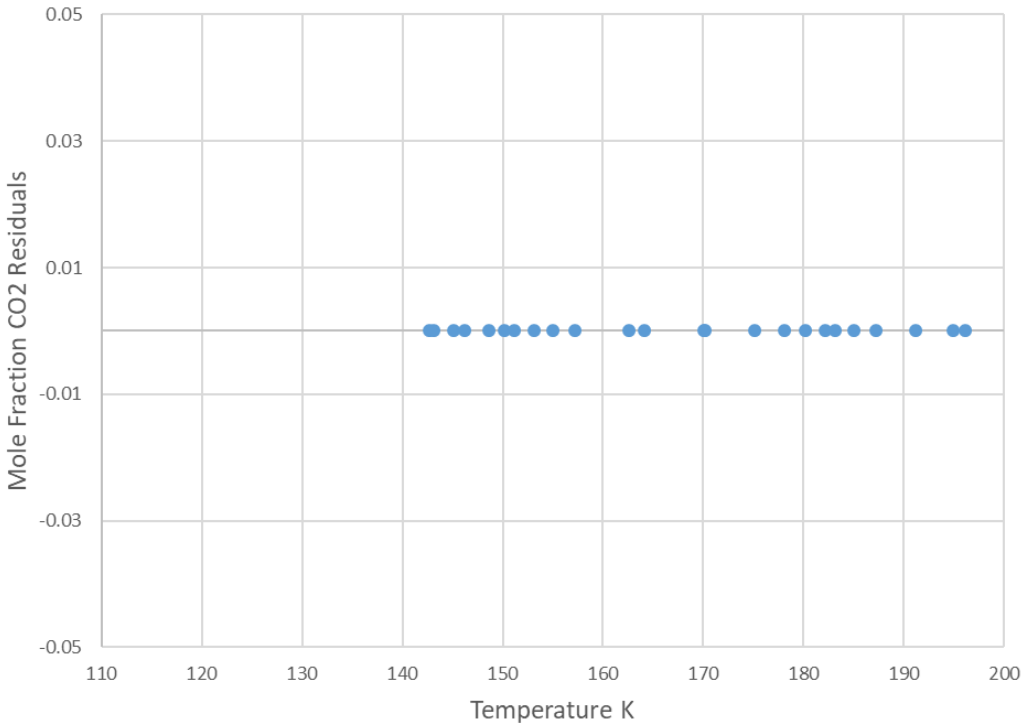

Figure 3-5: N-Pentane PR SLE Residual Plot

3.2.4 Model Predictions

The CCC-ECL process has demonstrated 90+% CO_2 capture[118] in the field. These field tests use skid-scale equipment and do not have heat-recovery compressors or similar equipment that is essential for efficient operation but unavailable at skid scale. Therefore, process simulations provide energy consumption estimates which, for 90% CO_2 capture at a 550 MW_e coal-fired power plant, is 0.74 MJ_e/kg CO_2. The PR EOS was chosen for this model based on an initial validation. Further validation, as shown in the previous section, justified its continued use in process simulations. PR was chosen because of its ability to effectively handle solids formation and its accuracy predicting VLE for CO_2-hydrocarbon systems.

Table 3-2: Energy Requirement by Unit for 550 MW_e Coal-Fired Power Plant (Major Units Shown in Figure 3-1)

Unit	Energy Required [MW_e]
Blower	13.76
CF_4 Compressor	27.93
CO_2 Compressor	0.70
Natural Gas Compressor	18.55
Mixed Refrigerant Compressor	20.37
Contact Liquid and Slurry Pumps	2.21
Liquid CO_2 Pump	0.98
Mixed Refrigerant Liquid Pumps	0.11
Natural Gas Turbine	-1.38
Mixed Refrigerant Turbine	-0.63
Total	82.59

Other EOSs could have been used for specific units, but the validation indicated PR was as good as, or better than, alternative EOSs. Table 3-2 summarizes the full-scale energy consumption.

Table 3-3: Energy Balance

	Sensible + Latent	Power	Total
Heat In	[MW_{th}]	[MW_e]	[MW_{th}]
Flue Gas	-1860.4		-1860.4
Makeup Contact Liquid	-3.8		-3.8
Cooling Water	-13426.4		-13426.4
Process Units		82.6	82.6
Totals	-15290.6	82.6	-15208.0
Heat Out			
Cooling Water	-14252.9		-14252.9
N_2-Rich Gas	-178.7		-178.7
CO_2-Rich Liquid	-1037.1		-1037.1
Water Condensate 991	157.0		157.0
E416A	-28.2		-28.2
E416B	29.2		29.2
E416C	-0.9		-0.9
C306 Cooling Water	32.7		32.7
C570 Cooling Water	21.4		21.4
C700 Cooling Water	44.2		44.2
Process Losses*	5.4		5.4
Totals	-15208.0	0.0	-15208.0
Difference			0.0

Three compressors drive the refrigeration and account for 80.9% of the total energy penalty. The majority of the remaining energy penalty is due to the flue gas blower. The flue gas blower overcomes pressure drop and accounts for 16.7% of the total energy penalty. The energy consumption of the blower may decrease by creating lower discharge pressures. Lower discharge pressures occur with improved cooling towers. The remaining power consumption is 2.4% of the total energy penalty and thus less significant potential for improvement from an energy penalty perspective.

Table 3-4: Mass balance (Flow Rates in kg/hr)

In	O_2	N_2	CO_2	H_2O	Contacting liquid	Ar	Total
Flue Gas	57726	1433810	447670	205464	0	24608	2169278
Makeup Contacting liquid	0	0	0	0	5483	0	5483
Water	0	28	44	3020154	0	0	3020226
Totals	57726	1433838	447714	3225618	5483	24608	5194987
Out	O_2	N_2	CO_2	H_2O	Contacting liquid	Ar	Total
N_2-Rich Gas	57726	1433782	43834	17439	72	24608	1577461
CO_2-Rich Liquid	0	0	403836	0	5339	0	409175
Water	0	56	88	3208179	0	0	3208323
Totals	57726	1433838	447758	3225618	5411	24608	5194959
Rel. Difference	0.000	0.000	0.000	0.000	0.003	0.000	0.000

Table 3-3 details the total energy balance, including the previously discussed 82.6 MW_e of power consumed by process equipment. Process losses match the heat in/out of the plant and are less than 0.27% of total heat as benchmarked by NETL[119].

Table 3-4 summarizes the mass balance based on the full-scale simulation. The total mass balance closes to within 0.01%.

Some contacting liquid in the system is lost during direct contact with the flue gas and during CO_2 separation in a flash drum. The concerns are primarily the environmental and economic impact of the combined losses. As simulated, the contacting liquid present in the exhausted N_2-rich gas is acceptable by EPA source guidelines for hydrocarbon emissions. Contacting liquid in the CO_2-rich stream is of lesser environmental concern since similar hydrocarbons exists in the ground where the CO_2 will be used for EOR. The economic impact of the contacting liquid losses at full-scale implementation of CCC-ECL will likely change with the economics of its supply and demand. However, hydrocarbons suitable as contacting liquid generally come from oil and gas fractionation, with potential supplies greatly outweighing any potential need. Experimental tests completed with many hydrocarbons generally indicate that losses will be minor.

A sensitivity analysis shows the effects of variations from the current base model. These variations reflect an industry review of common challenges, available technologies, and expected technological improvements. Table 3-5 shows the results of the sensitivity analysis. The 4% CO_2 inlet variation corresponds to a natural gas combined cycle power plant that has less CO_2 emissions per unit power produced. Excluding the natural gas case, the energy penalties ranges from 0.71-0.92 MJ_e/kg CO_2, which compare very favorably with other technologies.

If high-pressure is required for EOR or sequestration as suggested by some studies[112, 114], the energy penalty would increase by 0.004 MJ_e/kg CO_2. Without the turbines on the liquid natural

gas and mixed refrigerant streams, the process loses 2.1 MW_e and the energy penalty would increase by 0.016 MJ_e/kg CO_2.

An economic analysis used the same scenarios as the energy sensitivity analysis. All equipment prices came from Aspen Plus' built-in economic analysis, excluding multi-stream heat exchangers. A price quote from Chart Energy and Chemicals provided the basis for the multi-stream heat exchangers in the model. Deviations from the base scenario have a price difference equal to 86 \$/m^2 multiplied by the change in heat transfer area. The change in heat transfer area assumed that U and ΔT were constant in Equation 3-1.

$$Q = UA\Delta T \tag{3-1}$$

Table 3-5: Economic Analysis of Process Variations and Resulting Cost of Electricity (COE)

Case / Variable	Base Case	Variation	CAPEX [\$x10^6]	Energy Penalty [MJ_e/kg CO_2]	COE [cents/kWh]
No CO_2 Capture			-	-	5.89
Amine CO_2 Capture			469	1.379	10.65
Base CCC-ECL Case			361	0.738	8.96
CO_2 Inlet	16%	4%	217	1.669	6.67
		12%	345	0.920	8.74
		14%	357	0.819	8.89
CO_2 Capture	90%	89%	359	0.711	8.93
		91%	365	0.740	9.03
		99%	391	0.846	9.45
Cooling Water Temp	289 K	281 K	362	0.717	8.97
		303 K	367	0.772	9.06
Efficient Turbines[A]	92%	89%	364	0.738	9.00
		94%	366	0.737	9.07

Table 3-5: Continued

Case / Variable	Base Case	Variation	CAPEX [$x10^6$]	Energy Penalty [MJ_e/kg CO_2]	COE [cents/kWh]
HX Temp Approach	1 K	2 K	318	0.772	8.88
		4 K	299	0.863	8.95
Pressure Drop	5 kPa	Mfg. Quote	369	0.832	9.16
HX Temp Approach	1 K	2 K	318	0.772	8.88
Compressor Efficiency[B]	90%	85% CF_4	363	0.752	9.02
		92% CF_4	362	0.732	8.99
		85% NG	363	0.747	9.01
		92% NG	362	0.734	8.99
		85% MR	363	0.748	9.01
Blower Efficiency[B]	90%	85%	363	0.745	9.01
		92%	362	0.734	8.99

[A]Turbine efficiencies are isentropic. [B]Compressor and Blower efficiencies are polytropic.

where U is the heat transfer coefficient, A is the heat transfer area, ΔT is a correlation for the temperature difference inside a plate and frame heat exchanger, and Q is the heat duty. $U\Delta T$ is the quotient of the heat duty calculated by Aspen Plus for the base case and the area for the heat exchanger as determined by Chart. This value determined the new area with heat duties calculated by Aspen Plus for each scenario. Table 3-5 shows the capital expenditure (CAPEX) attributed to carbon capture, energy penalty, and cost of electricity (COE). The 4% CO_2 inlet case refers to a natural gas power plant and is the cheapest scenario in the analysis.

CCC-ECL simulations for retrofit of a 550 MW_e coal-fired power plant indicate an energy penalty for 90% CO_2 capture of 0.74 MJ_e/kg CO_2 captured. Reasonable best- and worst-case

scenarios are between 0.71-0.92 MJ_e/kg CO_2 captured. The estimated energy penalty is 1.67 MJ_e/kg CO_2 in the case of CCC-ECL implementation for a natural gas combined cycle power plant (4% CO_2 inlet concentration). The estimated cost of the CCC-ECL retrofit for this plant is $361 MM Capex. The financial result is an increased cost of electricity in the range of 2.85-3.56 cents/kWh. The energy and cost numbers compare favorably with alternative systems.

3.2.5 CCC-ECL for Syngas

This section focuses on decreasing CO_2 output of liquid fuels while generating such transportation fuels from domestic sources. Both coal and natural gas can produce transportation fuels, with the most efficient and established route involving Fischer-Tropsch synthesis (FTS). FTS converts coal and biomass to a light gas stream called syngas, which ideally contains high concentrations of H_2 and CO. The H_2 and CO catalytically react to form mostly aliphatic, straight-chain hydrocarbons fungible with petroleum-based diesel and jet fuel. In addition to the Fischer-Tropsch liquids, the process generates large amounts of water and CO_2. An FTS system that captures and stores CO_2 produces fewer greenhouse gases than a petroleum-based system[120-122].

The CO_2 footprint can be reduced further still by using biomass as part of the feedstock. Using biomass as a portion of this fuel may produce the biomass portion of the product as a renewable FTS liquid fuel, depending on the details of the biomass fuel cycle. Renewable liquid fuels differ in some important ways from their fossil counterparts[123-134] and require careful evaluation for each application. Jet fuel, for example, has strict requirements on viscosity, energy content, freezing/gelling point and volatility. These requirements prevent pure biodiesel and

similar renewable liquid fuels from aviation use, although they can blend with traditional fuels or with FTS fuels from coal or from biomass.

3.2.5.1 Coal and Biomass Gasification

Many methods exist to gasify coal and biomass[122, 135-141], but the general principles are similar. Gasification processes thermally decompose the feedstock to form gas-phase products. Additionally, water and CO_2 react with residual char to produce CO and H_2. Biomass gasification produces less CO_2 than combustion or biomass decomposition[127]. The feedstock, gasifier design, and operating conditions determine the composition of the syngas, which will determine the FTS products. The gasification process best suited to FTS applications optimizes the amounts of H_2 and CO in the resulting gas, called a synthesis gas or, almost universally, a syngas. This optimum mixture depends on the catalyst used in the process and ranges from a ratio of H_2 to CO_2 of a little over 1 for iron catalysts to 2 for cobalt catalysts. Syngas production combined with carbon capture and storage (CCS) and FTS produces liquid fuels with less greenhouse gas emissions than fuel production from petroleum without carbon capture[121, 122]. These benefits make gasification an attractive option to producing liquid fuels from an environmental standpoint.

3.2.5.2 FTS Process

The Fischer-Tropsch process has been around for more than 75 years[142, 143] with nearly continual improvement in catalysts and processes. The process is widely used to produce liquid fuels or chemicals from syngas when conditions prevent petroleum use, such as in Germany during World War II, South Africa during apartheid, and China now. Current processes use cobalt and iron catalysts and their alloys[144-151]. The FTS of hydrocarbons is a catalyzed reaction

with a product distribution that depends on the reactants. Raw syngas from coal and biomass has varying compositions, containing various amounts of CO_2 and H_2O and typically a H_2/CO ratio ≤ 1, which is lower than is ideal for the FTS process. Generally, a catalyzed water-gas shift reactor increases this ratio, which produces H_2 and adds additional CO_2 to the stream. CO_2 acts as an inert during the reaction across various catalysts[146, 148, 149] so long as CO is present. This decreases reactant concentration and therefore reaction rate. In addition, trace sulfur- and nitrogen-containing impurities in syngas poison FTS catalysts. Treatments prior to the catalysis step reduce these trace impurity concentrations to very low levels. CO_2 dilutes the stream and makes the impurity removal more difficult. CO_2 in low H_2/CO ratio mixtures can decrease the rate of hydrocarbon formation across the catalyst[149].

3.2.5.3 Model Predictions

Aspen Plus© commercial software simulated all variations of this process. The standard CCC process, which has already been validated[48], applies to coal-fired power plants and a detailed process overview has already been discussed. This investigation keeps the validated parameters from the standard CCC process and modifies the process to treat syngas (Figure 3-6).

The NETL baseline report[152] provides two syngas compositions (Table 3-6) that are used for an initial apples-to-apples comparison. The energy penalties for the two NETL cases were calculated using the differences between the capture and non-capture cases and adding the energy consumed by the acid gas removal (AGR) system. The energy penalty of AGR was included because the CCC process does both separation and compression of CO_2. Table 3-7 lists the energy penalties for the NETL and CCC capture processes. The CCC process requires ~25% less energy than the Selexol process used in the NETL cases.

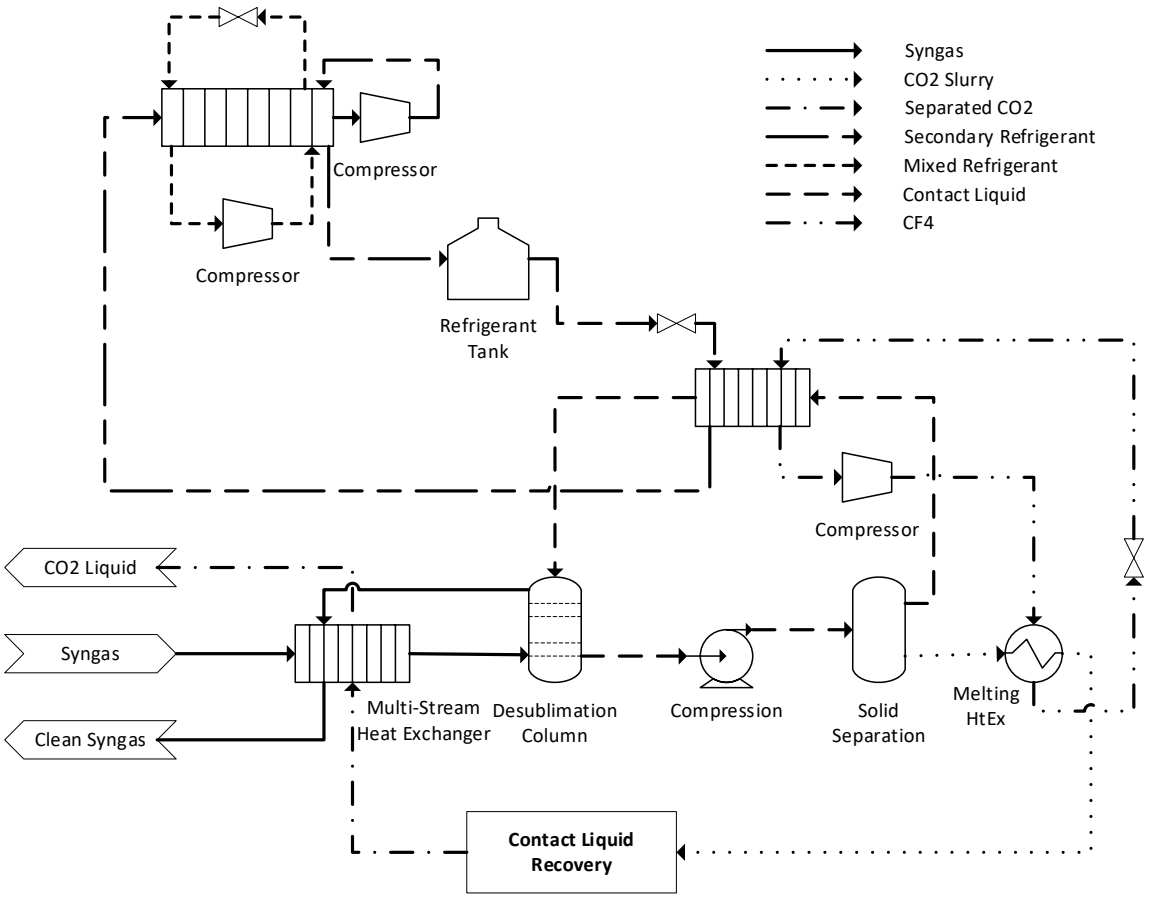

Figure 3-6: Simplified PFD of Syngas Treatment Process

The remaining analyses assume a base syngas composition as shown in Table 3-8 and several pressure and composition variations. Initial pressures ranged from 10 to 30 bar, with 22 bar as a base case. CO_2 capture percentages range from 90 to 99% with 90% as a base case, and CO_2 inlet compositions range from 4 to 6%, with 4% as a base case. CO_2 composition changes fixed the CO_2 content and scaled the composition of all other components.

Table 3-6: Syngas Composition for NETL Cases

Component	Value (Case 6)	Value (Case 8)
N_2	0.0030	0.0033
CO_2	0.3540	0.3758
CH_4	0.0001	0.0000
H_2O	0.0017	0.0017
H_2	0.4777	0.4609
CO	0.1589	0.1532
Ar	0.0021	0.0022
H_2S	0.0025	0.0028
COS	0.0001	0.0001

Table 3-7: Energy Penalties for NETL Cases

Method	Value (Case 6) [MJ/kg$_{CO2}$]	Value (Case 8) [MJ/kg$_{CO2}$]
NETL-Selexol	0.4360	0.4224
CCC	0.3232	0.3185

Table 3-8: Base Syngas Composition

Component	Value
N_2	0.476295
CO_2	0.040024
CH_4	0.007504
H_2O	0.001000
H_2	0.321199
CO	0.148092
C_2H_4	0.000180
Ar	0.005704

Table 3-9 shows the composition of the outlet gas after treatment. This corresponds to 90.53% capture of the inlet stream shown in Table 3-8. The associated energy penalty is 0.671 MJ_e/kg CO_2 captured.

Table 3-9: Base Syngas Composition After 90.53% CCC

Component	Value
N_2	0.494804
CO_2	0.003938
CH_4	0.007794
H_2O	0.00000
H_2	0.333681
CO	0.153847
Contact Liquid	1.13641E-05
Ar	0.005925

As is shown in the table, the process removes CO_2 while adding little contact liquid and leaving all of the CO and H_2 in the stream for conversion. This process sensitivity to pressure, inlet CO_2 percentage, and CO_2 capture percentage appear in Figure 3-7.

The CO_2 inlet and capture percentages have large changes in energy demand. However, assuming the same 25% advantage from the NETL results, the maximum CCC energy penalty will continue to be less energy-intensive than the Selexol process. These nonlinear curves reflect the increasing energy demand as the process approaches 100% CO_2 capture. However, the increase in energy demand from 90% to 95% carbon capture is relatively small. Simulations at different pressures indicate the pressure sensitivity of energy demand.

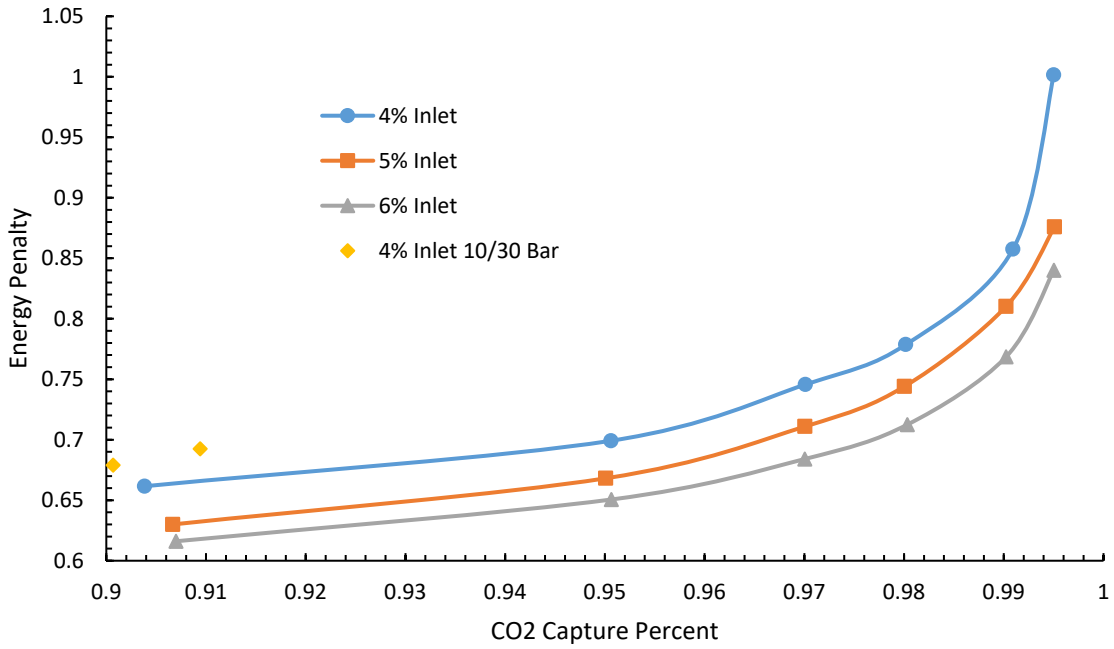

Figure 3-7: Energy Penalty [$MJ_e/kg\ CO_2$] for Different Inlets and Capture Percentages

3.2.5.4 Summary

Syngas streams with significant amounts of CO_2 appear commonly in chemical and fuel synthesis processes. Several forms of carbon capture exist to remove such CO_2, including amine and cryogenic systems. This investigation shows the effectiveness of the CCC process for syngas systems, the low energy cost, and the potential to capture as much as 99% of the CO_2 present in syngas. The specific energy demands for CCC processing range from 0.68 to 0.85 $MJ_e/kg\ CO_2$, depending on initial CO_2 content, removal efficiency, and pressure (in that order). These energy demands compete favorably with those for solvent-based systems as shown in the NETL cases (Table 3-7) where the CCC process uses up to 25.9% less energy.

The ability of the CCC process to effectively handle syngas demonstrates its versatility in handling both oxidizing and reducing streams. This is something difficult for amine systems to handle without significant modification. Other reducing environments, such as natural gas, could be treated in a similar fashion using the CCC process.

4 SOLVENT SYSTEMS: IMPROVING DECADES OF RESEARCH

The previous section discussed solutions for continuing to use fossil fuels in an environmentally sustainable manner. The CCC process, as with most other carbon capture processes, relies primarily on simulation results to determine energy costs, efficiencies, and effectiveness. Carbon capture systems for post-combustion applications have been in development for decades and have yet to be deployed in commercial systems[153]. Development is still ongoing and, despite proof-of-concept applications reaching pilot and small commercial plant size, simulations provide much more flexible and cost effective means to predict energy usage and cost for full-scale applications.

The problem with simulations, especially scaled simulations, is their uncertainty. The Carbon Capture Simulation for Industry Impact ($CCSI^2$)[154, 155] project has been working on building tools and methods to better predict and understand the uncertainty in full-scale simulations. Uncertainty quantification is one of the methods that helps in this endeavor. Previous work[155-157] used basic uncertainty quantification at a limited scope. This work builds off of the previous studies by expanding the scope to include multiple layers of models and significantly more parameters. The objective of this research is to quickly improve simulations of carbon capture processes to prepare for scale-up, addressing the third issue mentioned in the introduction.

This chapter begins with an overview of uncertainty quantification: what it is, how it works, and the benefits it provides. What follows are two case studies where uncertainty quantification is applied to carbon capture solvent systems. These two systems were chosen for the analysis based on funding provided by CCSI[2]. Neither time nor funding was available for applying uncertainty quantification to the CCC-ECL system. The first case, UT Austin's Independence model, was chosen to explore the possibility of multi-tier analysis. The multi-tier approach is important because it allows data to be properly matched with their respective models before the error is propagated to the full-scale simulation. The second case, Pacific Northwest National Laboratory's CO_2-Binding Organic Liquid, furthers the multi-tier approach by incorporating more parameters and more sub-models. This leads to a much more accurate estimate of the true uncertainty of the full-scale model results.

4.1 Uncertainty Quantification

Uncertainty quantification (UQ) is a statistical framework that systematically analyzes uncertainties and identifies data gaps in models. The current standard practice is discussed here briefly to provide context before discussing how UQ works and how it can be used to improve a model. The goal of using UQ is to accurately predict the uncertainty in full-scale model predictions by using data collected at smaller scales. The uncertainty can then be reduced by applying a discrepancy function.

The code used for this analysis is proprietary and will not be shared. It was written in R and can be adapted to a variety of systems given the user has appropriate knowledge to adjust the code. A more general code called FOQUS[158] is in development by CCSI[2] that performs basic UQ functions. It is freely available on Github.

4.1.1 Standard Practice

For most new systems, standard practice minimizes the sum of squared errors between model and experimental data values for each sub-model to obtain fitting parameters. Additionally, expert knowledge often provides values for parameters that have insufficient data to regress. The overall result is a fixed set of parameters for the model. These parameters provide one prediction for each data point and one overall prediction for energy penalty and carbon capture percentage. This approach effectively assumes that the model is completely accurate in its point estimate of all properties and results. A sensitivity analysis on these systems demonstrates robustness, but these investigations typically focus on model inputs rather than model parameters (i.e., temperature, pressure, mole fractions, etc. instead of EOS, kinetics, and mass transfer equation parameters). This provides a good sense of the predicted system response to changes in inputs, but it does little to show how model results will change if parameter values are inaccurate.

4.1.2 Bayesian Process: Uncertainty Quantification

UQ uses a Bayesian paradigm to minimize uncertainty through parameter selection [156]. UQ considers model parameters, model outputs, and other quantities as variables with individual distributions [155]. UQ progresses through each stage of the model with several steps. For simplicity the process is divided into 7 steps listed below.

1) For each sub-model, identify the equations, experimental data, inputs (x), outputs (y), and model parameters (θ) relevant for UQ analysis.
2) Obtain physically reasonable ranges for inputs and model parameters. These may have to be calculated from other quantities.

3) Identify prior distributions for model parameters.
4) Using an emulator (surrogate model)
    a. Develop a "space-filling" design over inputs/parameters that will be used to train the emulator (surrogate model).
        i. An LHS function samples from each parameter distribution to fill an n-dimensional space for combinations of parameter values which creates a space-filling design.
    b. Run model (e.g. Aspen) at design locations to obtain desired outputs that are comparable to experimental data.
        i. Because the parameter combinations may lead to unphysical regions or numerical convergence errors the model may fail to converge for certain combinations. Reconsider the design space if there are too many failures.
    c. Develop the emulator for the model.
5) UQ analysis: calibrate the model to experimental data to compute posterior distributions of model parameters. Involved in this step is the development of the emulator for the model.
6) Get predictions with uncertainty of outputs.
7) Propagate posterior distributions to the next stage if needed.

The analysis begins with each sub-model and its associated parameters. The inputs and outputs for the model should match those of the data used for calibration. For example, Pxy data would have temperature and feed concentrations as the input and pressure, vapor phase composition, and liquid phase composition as the outputs with vapor pressure correlations and binary interaction parameters as the parameters. Parameter down-selection occurs during this

step. Aspen Plus' property package has hundreds of default parameters for well-characterized components that often remain at default values for UQ because there is no estimate of parameter uncertainty. Parameters from sub-models with no supporting data from which to estimate uncertainty do not benefit from UQ and remain at original values. Parameters required for thermodynamic consistency require adjustments that maintain consistency during UQ or, if this is not possible, should remain unaltered. This process reduces the parameter count from several hundred to tens of parameters, which focuses UQ efforts.

Expert judgment and system knowledge determine physically reasonable ranges for the inputs and model parameters. If reasonable ranges for a property are known instead of individual parameters, then the parameter values are determined using that metric instead.

Prior distributions are identified only if enough information exists to justify their use. These prior distributions come from expert judgement, literature sources, or a sub-model analysis. Otherwise, a uniform distribution is assumed over the ranges determined in the previous step.

4.1.3 Emulator

A computationally rapid model can directly provide the UQ calibration. More complex models, such as a full-scale Aspen model, require an emulator[159, 160] that replaces the full model in UQ calibration. A space-filling design identifies the meaningful data and simulation ranges for the inputs and parameters. Latin hypercube sampling[161-163] (LHS) typically defines these ranges by producing a multi-dimensional grid of parameter values based on the given parameter ranges. The model predicts and saves outputs for each point in the space-filling design. A design that produces too many computational failures requires re-evaluation, which could include narrower

prior distributions or analyzing parameter interactions to narrow the distributions. Convergence failures are common in these analysis since combinations of parameters could produce unphysical results or convergence errors. By narrowing the prior distributions, i.e. forcing parameter values closer to the original value, the model is often easier to converge.

The emulator[164] is a weighted sum of basis function (e.g., smoothing splines) and trains on the results from the actual model to determine weighting. Typically a randomly selected 90% of the simulation results train the emulator while the remaining 10% validate the emulator's accuracy. R^2 and root-mean-squared values determine if the emulator is consistent with the model output. If the emulator does not predict the remaining 10% of the data, a different set of training and validation data may resolve the issue. More model runs may be necessary if the emulator fails validation too many times.

The model calibrates[164-166] to the experimental data as part of the uncertainty quantification process, which uses Bayesian inference. The result is a set of posterior distributions for model parameters that indicate the likelihood of the parameters to be a specific value. A broad range means that the model is fairly insensitive to that parameter and that a broad range of parameter values fit the data well. A narrow band indicates that the model is sensitive to that parameter and only a narrow range of parameters fit the data well.

Using the parameter distributions from the calibration step, the model predicts the data with uncertainty bounds. This helps determine which models suffer from poor data and can be used as the basis of a new experimental design. If the first-stage models are sub-models of a larger system, then the posterior distributions are propagated through the large system to determine the uncertainty in overall model predictions.

4.1.4 Discrepancy Function

A discrepancy function (δ) is an error function that attempts to adjust the model for errors in the model and parameters. Its use is shown in Equation 4-1 where η represents the model, δ represents the discrepancy function, or model error, ε represents the measurement error, ω is an array of inputs to the system (temperature, pressure, mole fraction, etc.), θ is an array of parameter values, and y represents the new model.

$$y = \eta(\theta, \omega) + \delta(\omega) + \varepsilon \tag{4-1}$$

Three approaches to derive a discrepancy function are presented here. These are a normal Gaussian Process[167] (GP), Gaussian Process Models for Simulation Analysis[165, 168] (GPMSA), and Bayesian Smoothing Spline ANOVA[164] (BSS-ANOVA). All three of these approaches implement a GP in different ways to derive the discrepancy function. This work focuses on the BSS-ANOVA method outlined in Equation 4-2 and 4-3. In these equations, β values are fitting parameters that correspond to specific inputs, ϕ functions are eigenfunctions (scaled by eigenvalues) of the BSS-ANOVA covariance function, and ω is the same as previously defined. $\beta_{j,i}$ values correspond to the effect of input ω_j on the discrepancy. In practice Equation 4-2 only includes select 3rd order terms and rarely includes anything above 3rd order. Equation 4-3 is also generally truncated after 15-25 terms.

$$\delta(\omega) = \beta_0 + \sum_{j=1}^{q} \delta_j(\omega_j) + \sum_{j<k}^{q} \delta_{j,k}(\omega_j, \omega_k) + \cdots, \tag{4-2}$$

$$\delta_j(\omega_j) = \sum_{I=1}^{\infty} \beta_{j,I} \phi_I(\omega_j) \tag{4-3}$$

UQ calculates distributions for β and θ based on data which are used in Equation 4-1 to show the uncertainty in the model. When the analysis is complete β and θ values can be chosen

from their calculated distributions using a maximum likelihood calculation. The resulting discrepancy function can provide a better fit to data than model regression by adjusting the model form and reduces the 95% confidence interval width. Unfortunately if used improperly it can lead to overfitting of the data. To fully implement a discrepancy function in an Aspen model would require modifying the physical property equations to include the discrepancy function. This would most likely necessitate a FORTRAN subroutine or equivalent, but it could result in the selection of another model form. Expert judgement can determine if the discrepancy function should be incorporated directly, if it looks like an additional model term that should be included, or if a different model should be used that more closely approximates the effects of the discrepancy function. Incorporating the discrepancy function improves the accuracy and reduces the uncertainty of the sub-model and model results.

4.2 UT Austin's Independence Model

The University of Texas (UT) Austin[169] developed a rigorous amine simulation framework in Aspen Plus® for use with piperazine (PZ) carbon capture systems named Independence. Independence, uses parameters for various sub-models in the framework regressed from in-house data. The chemical reactions occurring in the system are

$$2PZ + CO_2 \leftrightarrow PZH^+ + PZCOO^- \quad (4\text{-}4)$$

$$2PZCOO^- + CO_2 \leftrightarrow PZ(COO)_2^{2-} + H^+PZCOO^- \quad (4\text{-}5)$$

$$PZ + H^+PZCOO^- \leftrightarrow PZH^+ + PZCOO^- \quad (4\text{-}6)$$

The published data sets[170] for this analysis are:

- Low-temperature water/amine heat capacity data (Hilliard, 2008[171])

- High-temperature water/amine heat capacity data (Nguyen, 2012[172])
- Water/amine volatility data (Hilliard, 2008[171] and Nguyen, 2012[172])
- Low-temperature CO_2 solubility data (Dugas, 2009[173], and Fulk, 2016[174])
- High-temperature CO_2 solubility data (Xu, 2011[175])
- Loaded CO_2 heat capacity (Freeman, 2010[176])

4.2.1 Models and sub-models

Aspen Plus' ELECNRTL equation of state (EOS) modeled the thermodynamics of this system with default parameter values from Aspen used for any parameter not regressed. In addition to, or as part of, the EOS model there are sub-models for temperature-dependent properties, mass transfer, and kinetics. A few of these models replace the Aspen default behavior with custom FORTRAN subroutines, but most of the models use the Aspen default framework with custom parameters. The thermodynamics sub-model is the focus of this analysis, which uses Aspen's default EOS framework. This investigation builds upon the results of the initial Independence model.

The Non-Random Two-Liquid Electrolyte Model (ELECNRTL) activity coefficient model "satisfactorily represents physical interactions of true species in aqueous single electrolyte systems and multicomponent electrolyte systems over wide ranges of concentrations and temperatures"[177] using only binary interaction parameters and adapted from the original NRTL EOS developed by Renon and Prausnitz in 1968. It handles infinitely dilute systems, pure fused salts, mixed solvent electrolyte systems, and reduces to the original NRTL for non-electrolyte systems[177]. The model separates interactions to local and long-range ion-ion interactions. These interactions are added together to produce the excess Gibbs energy[170, 177-181]. The asymmetric

Pitzer-Debye-Hückel (PDH) model and the Born equation represent the long range interactions while the standard NRTL EOS provides the local interactions (*lc*).

$$\frac{G_m^{*E}}{RT} = \frac{G_m^{*E,PDH}}{RT} + \frac{G_m^{*E,Born}}{RT} + \frac{G_m^{*E,lc}}{RT} \tag{4-7}$$

$$\ln \gamma_i^* = \ln \gamma_i^{*PDH} + \ln \gamma_i^{*Born} + \ln \gamma_i^{*lc} \tag{4-8}$$

In these equations γ is the activity coefficient, x is the liquid mole fraction, R is the universal gas constant, G^E is the excess Gibbs free energy, and T is temperature with the $*$ denoting an asymmetric reference state . Additional information about these sub-models can be found in Aspen documentation and above-referenced literature.

The Independence model focuses on the local excess Gibbs energy equation and associated parameters so the parameters of the other two contributions are fixed. The local contributions are the same as the traditional NRTL excess Gibbs energy equation with some modifications for cations and anions.

$$\frac{G_m^{E,lc}}{RT} = \sum_B X_B \frac{\sum_j X_j G_{jB} \tau_{jB}}{\sum_k X_k G_{kB}} + \sum_c X_c \sum_{a'} \left(\frac{X_a}{\sum_{a''} X_{a''}} \right) \frac{\sum_j X_j G_{jc,a'c} \tau_{jc,a'c}}{\sum_k X_k G_{kc,a'c}} +$$

$$\sum_a X_a \sum_{c'} \left(\frac{X_c}{\sum_{c''} X_{c''}} \right) \frac{\sum_j X_j G_{ja,c'a} \tau_{ja,c'a}}{\sum_k X_k G_{ka,c'a}} \tag{4-9}$$

$$G_{cB} = \frac{\sum_a X_a G_{ca,B}}{\sum_{a'} X_{a'}} \tag{4-10}$$

$$G_{aB} = \frac{\sum_c X_c G_{ca,B}}{\sum_{c'} X_{c'}} \tag{4-11}$$

$$\tau_{BB'} = A_{BB'} + \frac{B_{BB'}}{T} + F_{BB'} \ln T + G_{BB'} T \tag{4-12}$$

$$\tau_{ca,B} = C_{ca,B} + \frac{D_{ca,B}}{T} + E_{ca,B} \left[\frac{(T^{ref} - T)}{T} + \ln \left(\frac{T}{T^{ref}} \right) \right] \tag{4-13}$$

$$\tau_{B,ca} = C_{B,ca} + \frac{D_{B,ca}}{T} + E_{B,ca}\left[\frac{(T^{ref}-T)}{T} + \ln\left(\frac{T}{T^{ref}}\right)\right] \quad (4\text{-}14)$$

$$X_j = x_j C_j \quad (4\text{-}15)$$

$$C_j = \begin{cases} z_j & \text{for ions} \\ 1 & \text{for molecules} \end{cases}$$

$$G_{ji} = e^{(-\alpha_{ji}\tau_{ji})} \quad (4\text{-}16)$$

$$\tau_{ji} = \frac{g_{ji}-g_{ii}}{RT} \quad (4\text{-}17)$$

In these equations, B denotes molecules, c denotes cations, a denotes anions, g is the energy of interaction between two components (how non-ideal two components mix) and is symmetric, X denotes an effective local mole fraction, α is the nonrandomness factor for two components and is symmetric, T^{ref} is 298.15 K, and other parameters are the same as previously defined. The "primes" denote molecules, cations, and anions different from non-prime counterparts. The effective mole fraction parameters estimate excess Gibbs energy in apparent binary systems. The system estimates separate activity coefficients for anions, cations, and molecules. Further explanation and derivations can be found in Aspen Plus' documentation[177].

In addition to the activity coefficient model described above, there are also models for Henry's constant (Eq. 4-18), heat capacity (Eq. 4-19), vapor-liquid equilibrium (Eq. 4-20), and chemical equilibrium. Henry's constant and heat capacity are purely empirical correlations and have many parameters within Aspen. Typically, only the first few parameters are used for analysis and the rest are left as zero. The equations for Henry's constant and the infinite dilution heat capacity model appear below. There are many models for heat capacity. They differ from the dilution state of the anion/cation and non-ionic molecules have different models still. The

intermediate form of the vapor-liquid equilibrium equation shown below includes the Henry's constant. The Henry's constant replaces the vapor pressure in this instance, which is only fully valid at near-infinite dilution, but meets the needs of this model by using γ_i^* to compensate for the problems associated with this assumption. On a theoretical basis, this isn't a valid use of γ_i^*, but it works well for the model and is convenient[171].

$$\ln H_{ia} = A_{ia} + \frac{B_{ia}}{T} + C_{ia} ln(T) + D_{ia} T + \frac{E_{ia}}{T^2} \tag{4-18}$$

$$C_{p,i}^{\infty,aq} = C_1 + C_2 T + C_{3i} T^2 + \frac{C_{4i}}{T} + \frac{C_{5i}}{T^2} + \frac{C_{6i}}{T^{\frac{1}{2}}} \tag{4-19}$$

$$y_i \phi_i P = x_i \gamma_i^* H_{i,H_2O} \tag{4-20}$$

In these equations a is a solvent, y is the vapor mole fraction, ϕ is the vapor fugacity coefficient, P is the total pressure, H is the Henry's constant, C_p is the heat capacity, i denotes a component, and A through E and C_1 through C_{6i} are independent parameters. This study focused on two sub-models in the system, namely: the heat capacity model and the Henry's constant model. The thermodynamics, kinetics, and mass transfer models include over 200 possible parameters that could be used for calibration. To simplify the problem to a more reasonable scale for calibration, most of these parameters remain constant.

4.2.2 Methodology

The complexity of the overall model suggests calibration is best done in two tiers. The first tier calibrates parameters to the sub-models while the second tier uses data from the overall model to calibrate parameters. The first tier includes five parameters: three for the Henry's constant and two τ values for the heat capacity (Table 4-1). The Henry's constants and unloaded

heat capacity mixing are the tier 1 sub-models. These parameters were chosen based on a sensitivity analysis and the data provided.

Table 4-1: Tier 1 Parameters

Parameter Name	Aspen Location	Equation Number / Parameter
τ_A	Properties>Methods>Parameters>Binary Interaction>NRTL>Component 1 = PZ, Component 2 = H_2O, AIJ	4-12 / $A_{BB'}$
τ_B	Properties>Methods>Parameters>Binary Interaction>NRTL>Component 1 = PZ, Component 2 = H_2O, AJI	4-12 / $B_{BB'}$
H_A	Properties>Methods>Parameters>Binary Interaction>Henry>Component 1 = PZ, Component 2 = H_2O, AIJ	4-18 / A_{ia}
H_B	Properties>Methods>Parameters>Binary Interaction>Henry>Component 1 = PZ, Component 2 = H_2O, BIJ	4-18 / B_{ia}
H_C	Properties>Methods>Parameters>Binary Interaction>Henry>Component 1 = PZ, Component 2 = H_2O, CIJ	4-18 / C_{ia}

The second tier originally included 18 parameters, but due to difficulties in model convergence this was later reduced to 10. The eight parameters removed were Gibbs energies and enthalpies of formation for four key chemical species. The ten remaining parameters include six loaded heat capacity parameters and four τ values for the NRTL EOS (Table 4-2). The tier 2 model is calibrated with the loaded heat capacity of the system and CO_2 partial pressure.

Table 4-2: Tier 2 Parameters

Parameter Name	Aspen Location	Equation Number / Parameter
$C_{p,aq}^{A1}$	Properties>Methods>Parameters>Pure Components>CPAQ0>Component = HPZCOO, Element 1	4-19 / C_1
$C_{p,aq}^{A2}$	Properties>Methods>Parameters>Pure Components>CPAQ0>Component = PZCOO-, Element 1	4-19 / C_1
$C_{p,aq}^{A3}$	Properties>Methods>Parameters>Pure Components>CPAQ0>Component = PZCOO-2, Element 1	4-19 / C_1
$C_{p,aq}^{B1}$	Properties>Methods>Parameters>Pure Components>CPAQ0>Component = HPZCOO, Element 2	4-19 / C_2
$C_{p,aq}^{B2}$	Properties>Methods>Parameters>Pure Components>CPAQ0>Component = PZCOO-, Element 2	4-19 / C_2
$C_{p,aq}^{B3}$	Properties>Methods>Parameters>Pure Components>CPAQ0>Component = PZCOO-2, Element 2	4-19 / C_2
τ_{a1}	Properties>Methods>Parameters>Electrolyte Pair>GMELCC>Pair 1 = H_2O, Pair 2 = [PZH+ PZCOO-]	4-14 / $C_{B,ca}$
τ_{a2}	Properties>Methods>Parameters>Electrolyte Pair>GMELCC>Pair 1 = PZ, Pair 2 = [PZH+ PZCOO-]	4-14 / $C_{B,ca}$
τ_{a3}	Properties>Methods>Parameters>Electrolyte Pair>GMELCC>Pair 1 = [PZH+ PZCOO-], Pair 2 = HPZCOO	4-13 / $C_{ca,B}$
τ_{b8}	Properties>Methods>Parameters>Electrolyte Pair>GMELCC>Pair 1 = [PZH+ PZCOO-], Pair 2 = CO_2	4-13 / $D_{ca,B}$

Separating the model into these tiers allows independent calibration which both eases computational stress and simplifies the problem to reduce the number of calibrated parameters. Once tier 1 calibration is complete the posterior distribution of the parameters are directly propagated to tier 2 calibration.

An emulator was used in this work due to the lack of an API (application programming interface) for linking pre-written R code to Aspen Plus. The speed of the Aspen simulation itself was less of an issue, instead, the time needed to write new code or adapt code to an unfamiliar API would have been excessive.

The Independence framework includes parameters regressed from the UT Austin data. Independence was used to calibrate the surrogate model by varying x's and θ's and matching the model outputs. Only converged solutions were used in training and validation. Approximately 10% of more than 500 Independence runs were set aside from model training to validate the surrogate model after training completed. This was done for both the sub-models in Independence and the overall Independence model meaning that the overall surrogate model used the intermediate surrogate models as inputs. If the validation wasn't within the specified tolerance then the data sets were randomized and a different 10% was reserved for validation.

4.2.3 Results

The parameters in Independence are already optimized. This investigation illustrates how UQ and collected data provide useful estimates of the prediction uncertainty. UQ does not regress new parameters for the model, but rather provides a distribution for the parameters and key outputs. Multivariate parameter distributions can be used to infer better parameter combinations based on where the distributions are centered, but that is not the focus of this analysis. Distributions for each of the outputs appear in the sections below. In addition to uncertainty distributions, UQ determines a discrepancy function that can be integrated into the sub-models to improve model accuracy.

4.2.3.1 Tier 1 Results

Figure 4-1 and Figure 4-2 show the original heat capacity and Henry's constant models' predictions at the 95% confidence level represented by red lines/planes with the black lines/planes representing the new calibration including discrepancy (also at the 95% confidence level) using the surrogate model. The black dots are the data points.

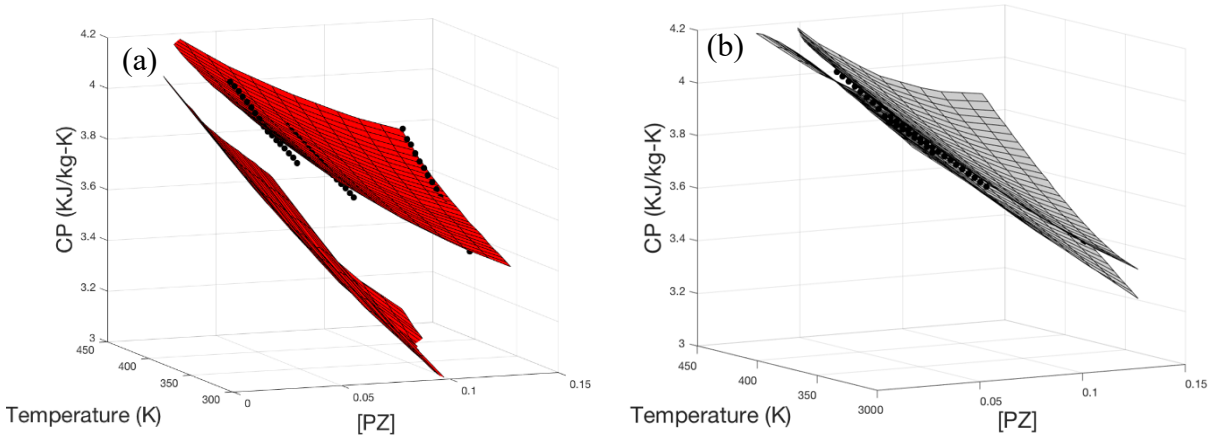

Figure 4-1: Calibrated Predictions of Heat Capacity. Black Dots Represent Experimental Data. Red Planes (a) are Uncertainty Bounds of the Original Model. Black Planes (b) are Uncertainty Bounds of the Model with Discrepancy[170].

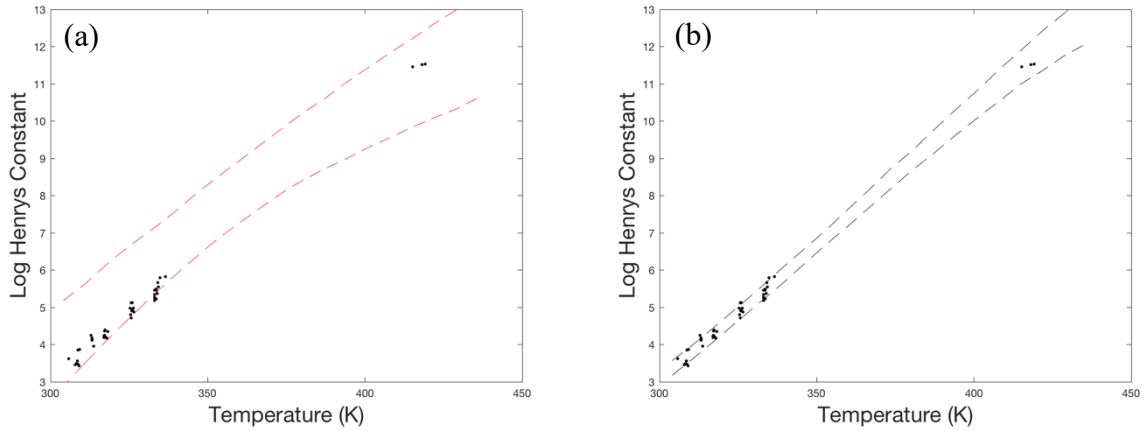

Figure 4-2: Calibrated Predictions of Henry's Constant. Black Dots Represent Experimental Data. Red Lines (a) are Uncertainty Bounds of the Original Model. Black Lines (b) are Uncertainty Bounds of the Model with Discrepancy[170].

The goal of this tier 1 calibration is to aid the tier 2 calibration, which is the overall model. Ideally this leads to an improvement in tier 1 parameters, but it's not required. Performing this calibration separately reduces computation time and eases the convergence by reducing the number of parameters for the tier 2 calibration. Figure 4-1 shows a significant improvement in heat capacity and parameters over the original models with data points moving within the 95% confidence interval bounds and the 95% interval shrinking. Figure 4-2 also shows a significant improvement to 95% confidence intervals with the inclusion of discrepancy.

4.2.3.2 Tier 2 Results

The tier 2 results assume fixed values for tier 1 parameters based on the calibration already performed. There are two sets of data used to calibrate the whole Independence model. These data sets include the partial pressure of CO_2 and the loaded heat capacity (C_p). The parameters are well-defined in this calibration with several having tight definitions relative to other parameters. This means that some parameters have very narrow posterior distributions, i.e. the analysis determined some parameters should be fixed or very slightly varied. Figure 4-3 shows the improvement in the fit when compared to Independence. Independence fits most of the data well, but it struggles for certain conditions. However, with UQ the fit is improved significantly.

This is quite an improvement in model results compared to Independence without UQ. To better illustrate the comparison Figure 4-4 shows a parity plot for the surrogate and Independence model results.

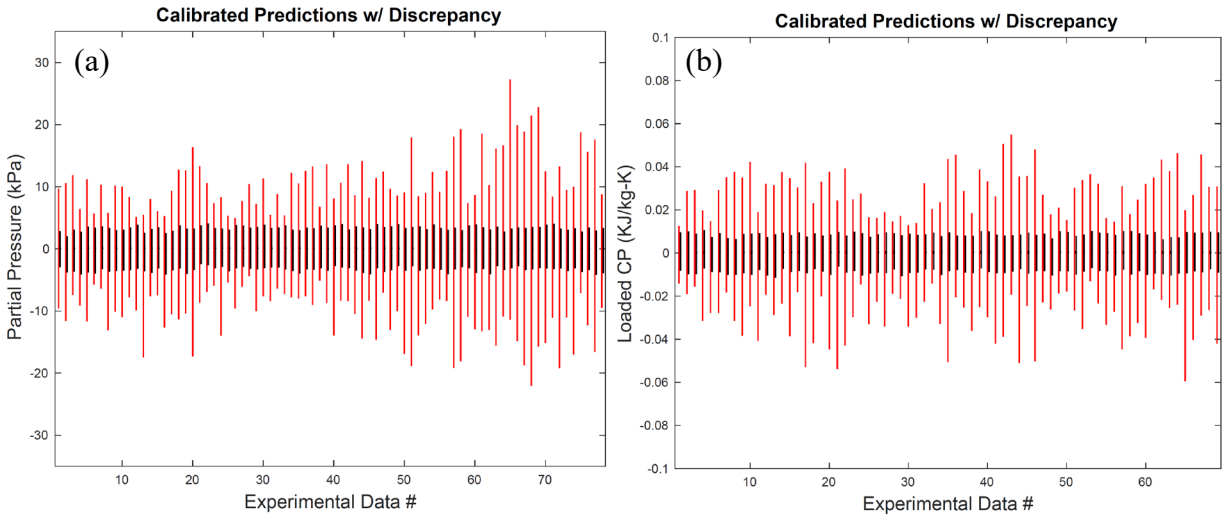

Figure 4-3: Calibrated Predictions of CO_2 Partial Pressure (a) and Loaded Heat Capacity (b). The Zero Line Represents the Normalized Experimental Value, Red Lines are Uncertainty Bounds of Calibrated Model-Only Predictions, Black Lines are Calibrated Predictions Including Uncertainty[182].

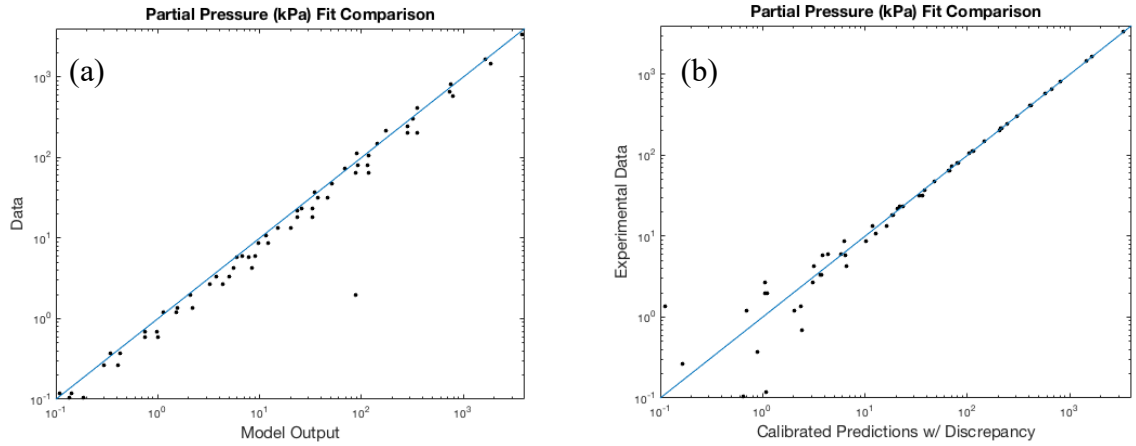

Figure 4-4: Partial Pressure Parity Plot. (a) UT Model Fit to Data. (b) Calibrated Model with Discrepancy[182].

The Independence model has an R^2 value of 0.9940 for the partial pressure predictions. By incorporating discrepancy this R^2 value increases to 0.9999, a 0.6% improvement. A visual inspection of Figure 4-4 would suggest that the fit is actually worse in the calibrated model, but

this is only true for small partial pressure values which don't influence the R^2 value as much as the higher values. The error with discrepancy is effectively the measurement error, which is given in absolute partial pressure thereby skewing the scatter in the log-log plot.

The Independence C_p model has an R^2 value of 0.7458. The original fit for C_p has some inherent bias, which can be seen in Figure 4-5 (a). The discrepancy term is able to overcome this bias when combined with the original model, which leads to the much better fit in Figure 4-5 (b). The calibrated model with discrepancy has an R^2 value of 0.9985, a 34% improvement.

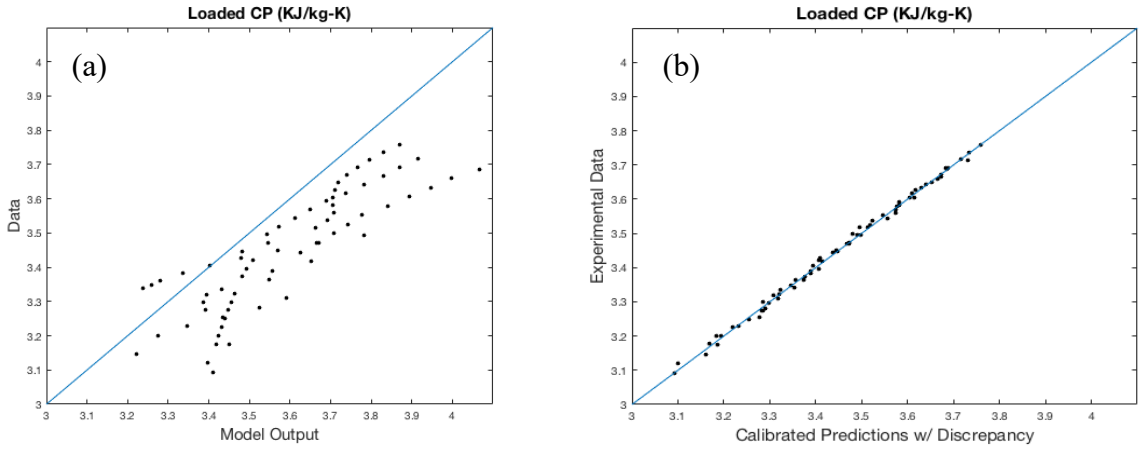

Figure 4-5: Loaded Heat Capacity Parity Plot. (a) UT Model Fit to Data. (b) Calibrated Model with Discrepancy [182].

4.2.4 Summary

As shown in the results there are clear benefits to applying uncertainty quantification to a model. The model fits the data much better when the discrepancy function is included with much narrower error bars and higher R^2 values. These results use a surrogate model with discrepancy included to demonstrate the impact on the model. To fully implement these results in the Aspen model would require modifying the physical property equations to include the discrepancy

function. This would most likely necessitate a FORTRAN subroutine or equivalent, but it could result in the selection of another model form. Expert judgement can determine if the discrepancy function should be incorporated directly, if it looks like an additional model term that should be included, or if a different model should be used that more closely approximates the effects of the discrepancy function. In addition to improving the model fit for tier 1 and tier 2 results incorporating the discrepancy function will improve the accuracy of the full-scale model decreasing the uncertainty in energy usage and carbon capture percent.

4.3 CO_2BOLs System

CO_2BOLs (CO_2-Binding Organic Liquid) is a novel non-aqueous polarity-swing solvent with a predicted energy penalty less than that of traditional amine systems[183]. The Pacific Northwest National Laboratory (PNNL) developed CO_2BOLs as a competitive alternative to amine processes. The CO_2BOLs system mirrors a standard amine process with an absorption column and a stripper column to capture and release CO_2, respectively. The CO_2BOLs solvent benefits from polarity-swing-assisted regeneration (PSAR) to lower the energy penalty when compared to monoethanolamine (MEA) systems. The PSAR design lowers the temperature in the stripper reboiler to reduce the required heat duty[183]. More details about the CO_2BOLs system can be found in the literature[184-193]. The Aspen Plus simulation and FORTRAN subroutines associated with it were provided by PNNL for this analysis.

4.3.1 Sub-Models

A sub-model is any model that feeds into a larger model. Sub-models can be nested as is the case with viscosity feeding into mass transfer feeding into the large-scale model. The Aspen Plus® model of the CO_2BOLs process involves several sub-models with specific parameters

chosen for the analysis of the CO_2BOLs PSAR system. The analyzed models are discussed in this section. Parameters were chosen following the previously mentioned technique of a sensitivity analysis followed by determining which parameters could have distributions inferred from the provided data.

4.3.1.1 Thermodynamics

The ELECNRTL EOS predicts vapor-liquid equilibrium (VLE) behavior for this model. Unpublished PTx data were provided for validation of this model. PTx data use the system temperature and component mole fractions to determine the pressure exerted by the mixture. Key parameters (bolded in Equations 4-21 through 4-25) were selected for UQ based on sensitivity and available data. Well-characterized parameters, such as pure-component parameters for water, kept at the original values in this study. Thermodynamic consistency was maintained throughout the analysis by keeping enthalpy of formation, heat capacity, and chemical equilibrium parameters constant. In these equations γ_i is the activity coefficient, H_{ia} is the Henry's constant, P_i^{vap} is the vapor pressure, X_i is the mole fraction, and $\alpha_{i,j}$ is a fitting parameter for the binary interaction of species i and j. Equation 4-21 is the standard NRTL EOS for mixtures containing only molecular components. More terms are added when ions appear in the mixture.

$$\ln \gamma_i = \frac{\sum_j X_j G_{j,i} \tau_{j,i}}{\sum_k X_k G_{k,i}} + \sum_j \frac{G_{i,j} X_j}{\sum_k G_{k,j} X_k} \cdot \left(\tau_{i,j} - \frac{\sum_m X_m G_{m,j} \tau_{m,j}}{\sum_k X_k G_{k,j}} \right) \quad (4\text{-}21)$$

$$\ln H_{ia} = \boldsymbol{A_{ia}} + \frac{\boldsymbol{B_{ia}}}{T} \quad (4\text{-}22)$$

$$\tau_{i,j} = A_{i,j} + \frac{B_{i,j}}{T} \quad (4\text{-}23)$$

$$\ln P_i^{vap} = \boldsymbol{A_i} + \frac{\boldsymbol{B_i}}{T+\boldsymbol{C_i}} \quad (4\text{-}24)$$

$$G_{i,j} = e^{(-\boldsymbol{\alpha_{i,j}}\tau_{i,j})} \quad (4\text{-}25)$$

4.3.1.2 Mass Transfer

Mass transfer relies on empirically calculated dimensionless numbers in addition to stream properties to calculate the mass flux from the vapor to the liquid stream. The key parameter (bolded) in this equation was used for UQ. Equation 4-26 is based on the Billet and Schultes equation[194]. k_G is the mass transfer coefficient and C_G is a fitting parameter.

$$k_G = D_G \boldsymbol{C_G} \left(\frac{a}{d_H}\right)^{0.5} {Sc_G}^{0.333} Re_G^{0.75} \sqrt{\frac{1}{\varepsilon - h_L}} \quad (4\text{-}26)$$

4.3.1.3 Viscosity

The viscosities of individual components as well as mixtures are calculated with Equations 4-27 through 4-30. Additional components not listed were added to Equation 4-30 using the standard Andrade mixing model. The key parameters (bolded) are used in UQ. In these equations μ is viscosity, T is temperature, MW is the molecular weight of a component, and α is the ratio of a component to the solvent.

$$\ln \mu_{BOLs} = \boldsymbol{A_{BOLs}} + \frac{\boldsymbol{B_{BOLs}}}{T} + \boldsymbol{C_{BOLs}} \cdot \ln T \quad (4\text{-}27)$$

$$w_{H2O} = \frac{\alpha_{H2O} \cdot MW_{H2O}}{\alpha_{H2O} \cdot MW_{H2O} + MW_{BOL}} \quad (4\text{-}28)$$

$$\mu_{BOLs-H2O} = \mu_{BOLs} \cdot (1 - w_{H2O}) + \mu_{H2O} \cdot w_{H2O} + \boldsymbol{D_{Binary}} \cdot w_{H2O} \cdot (1 - w_{H2O}) \quad (4\text{-}29)$$

$$\mu_{BOLs-CO2-H2O} = \mu_{BOLs-H2O} \cdot \mathrm{e}^{\alpha_{Co2} \cdot \boldsymbol{E_{CO2}}} \quad (4\text{-}30)$$

4.3.1.4 Kinetics

The selected chemical kinetics equation parameters (bolded) maintain thermodynamic consistency while still allowing UQ analysis. The two reaction mechanisms are given in Eqs. 4-31 and 4-33. The reaction rates for the two mechanisms are given in Eqs. 4-32 and 4-34. In these equations a is the component activity defined as the product of the mole fraction and the activity coefficient, T^{ref} is 313.15 K, and K is the chemical equilibrium constant. Other terms are taken from the standard Arrhenius equation.

$$2CO_2 + 2BOL \leftrightarrow (BOL - CD^+) + (BOL - CD^-) \tag{4-31}$$

$$r_1 = \boldsymbol{k_1} \exp\left(-\frac{\boldsymbol{E_1}}{R}\left(\frac{1}{T} - \frac{1}{T^{ref}}\right)\right) a_{CO_2} a_{BOL} \left(1 - \frac{a_{BOL-CD^+} a_{BOL-CD^-}}{(a_{CO_2} a_{BOL})^2 K_1}\right) \tag{4-32}$$

$$CO_2 + BOL + H_2O \leftrightarrow BOLH^+ + HCO_3^- \tag{4-33}$$

$$r_2 = \boldsymbol{k_2} \exp\left(-\frac{\boldsymbol{E_2}}{R}\left(\frac{1}{T} - \frac{1}{T^{ref}}\right)\right) a_{CO_2} a_{BOL} a_{H_2O} \left(1 - \frac{a_{BOLH^+} a_{HCO_3^-}}{K_2}\right) \tag{4-34}$$

4.3.2 Results

4.3.2.1 Parameter Distributions

Most parameters start with a uniform distribution; e.g., the distribution for the NRTL binary interaction parameter is shown in Figure 4-6. The UQ procedure, previously outlined, determines the distribution that results in the best fit to data for each parameter. These are called posterior distributions.

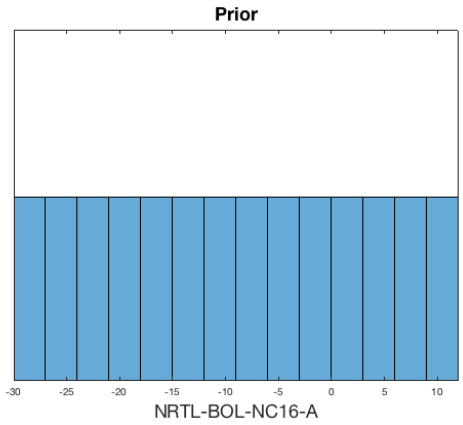

Figure 4-6: Uniform Prior Distribution for an NRTL Binary Interaction Parameter

Figure 4-7 shows univariate posterior distributions, distributions for only one parameter without respect for any other. In Figure 4-7–Figure 4-8, Elec denotes a binary electrolyte parameter, NRTL denotes an NRTL binary interaction parameter (A and B corresponding to the same letters in Equation 4-23 and C corresponding to α in Equation 4-25), Viscosity denotes a viscosity parameter from Equations 4-27 through 4-30, and Vapor Pressure denotes parameters of the same letter in Equation 4-24. Most of these distributions are still centered on the base parameter value, but several have distributions that suggest the model will provide a better data fit by adjusting the parameter to a different value. While these parameters have fairly narrow distributions, others had fairly wide distributions indicating data were lacking, the parameter is insensitive, or the parameter is redundant.

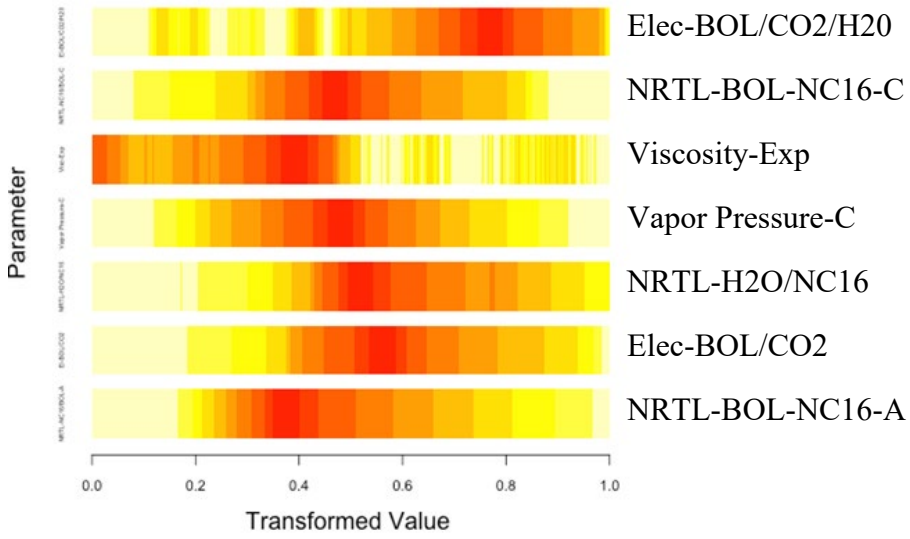

Figure 4-7: Posterior Distributions for 7 Key Parameters. Red Indicates High Probability for Parameter Value. 0.5 Indicates the Parameter's Base Value with 0.0 Being the Lowest Value and 1.0 Being the Highest Value in the Original Uniform Distribution.

Multi-modal distributions can occur when multiple parameters are correlated, leading to several combinations that fit the data well. Posterior distributions that lie on the max or min of the prior distribution indicate improper starting bounds and require UQ to be re-run with a wider distribution.

Figure 4-8 shows bivariate posterior distributions, densities that show how the distribution of one parameter affects the value of another parameter, on the off-diagonals. Univariate posterior distributions are shown on the diagonal. The bivariate posteriors are mirrored across the diagonal. The dark regions of the bivariate posterior distributions indicate parameter combinations with high likelihood. These bivariate distributions are derived from an n^{th}-order multivariate distribution, where n is the total number of parameters in the full distribution, which is used to determine how all parameter values affect each other. This is

especially useful for parameters that are part of a set of correlated parameters, such as binary interaction parameters, Henry's constant parameters, and viscosity parameters.

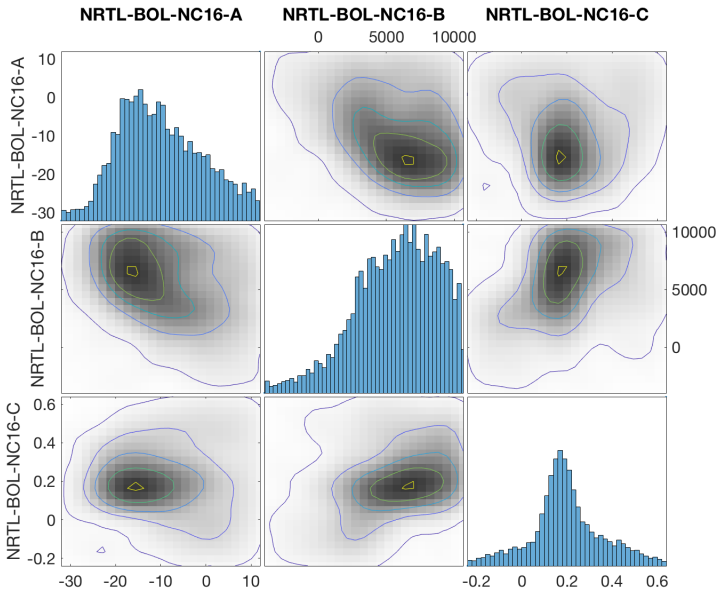

Figure 4-8: Bivariate Posterior Distributions for 3 Parameters

Taking the example of NRTL-BOL-NC16-A, the prior distribution is uniform as shown in Figure 4-6. UQ uses the given data to calculate a univariate posterior distribution represented in Figure 4-7 and the upper left of Figure 4-8. UQ also calculates bivariate distributions showing the distribution of a pair of parameters seen in the off-diagonals of Figure 4-8. These distributions are used for sub-model results and, ultimately, full-scale model results.

4.3.2.2 Sub-Model Results

Parameter distributions from the model calibration determine model uncertainty for the individual sub-models. They also determine a discrepancy function that can improve model accuracy. Figure 4-9 shows how including the discrepancy term can shrink the 95% confidence

interval. In Figure 4-9 uncertainty bounds for the blue line (40 °C), green line (50 °C), and red line (60 °C) improved by 65-81%, 59-76%, and 64-70% respectively. This discrepancy function can also improve the full-scale model by modifying the sub-model equations to incorporate discrepancy. In Aspen Plus this would be the equivalent of specifying a FORTRAN subroutine to replace a property sub-model.

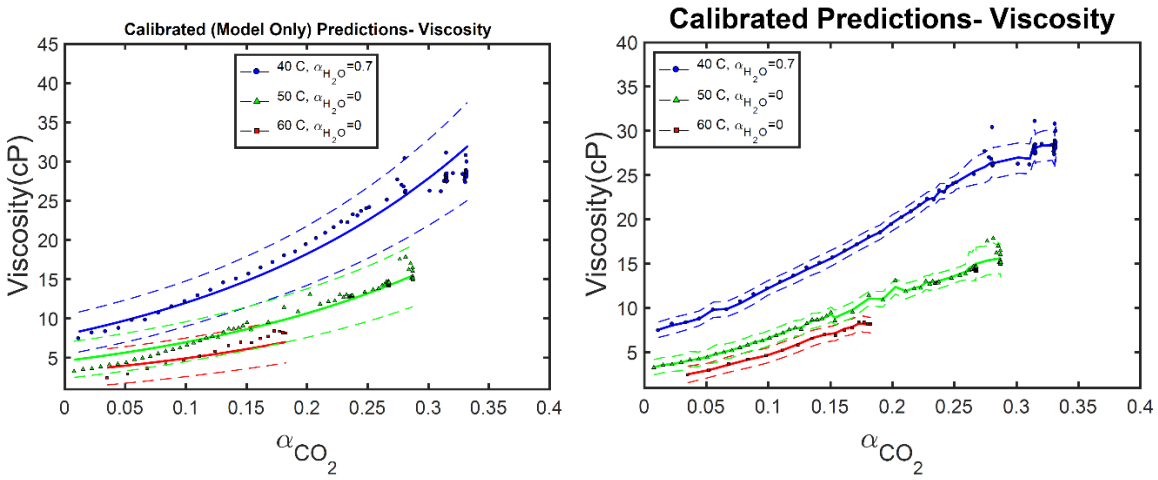

Figure 4-9: Calibrated Predictions for the Viscosity Sub-Model. Left: Model-Only Results (Model-Fit Uses Average Temperature) Right: Model with Discrepancy Term (Model-Fit Uses Temperature Taken from Each Data Point). Model is Solid Line and Dashed Line Represents 95% Uncertainty Bounds. α_x is the Ratio of Component x to CO_2BOL

Discrepancy can also help determine a better sub-model form. Figure 4-10 shows model results with discrepancy for part of the thermodynamic sub-model where uncertainty bounds for the blue line (40 °C), green line (60 °C), and red line (80 °C) improved by 42-58%, 28-57%, and 35-63% respectively.

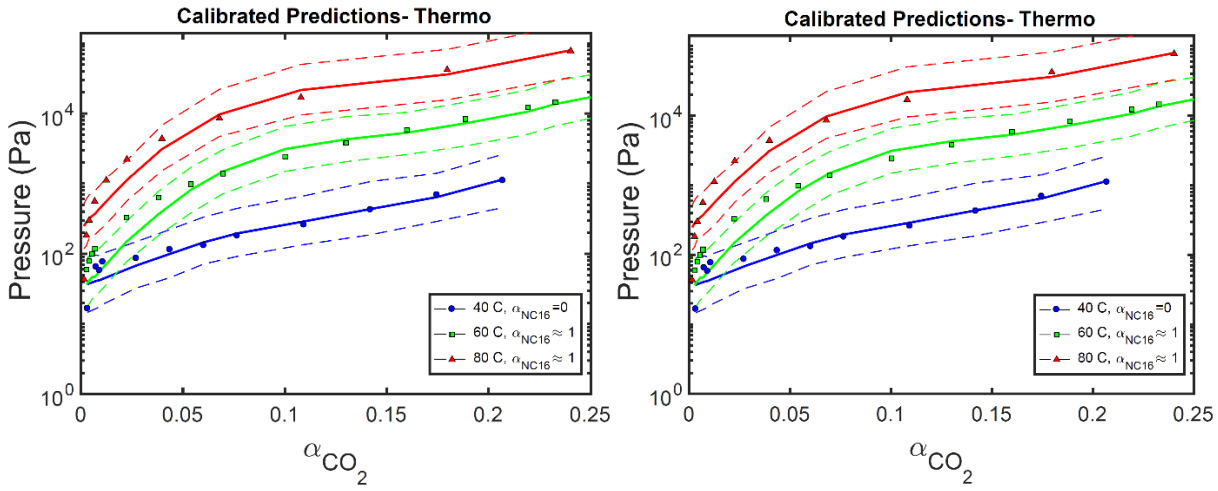

Figure 4-10: Calibrated Predictions for the Thermodynamics Sub-Model (PTx Data Shown). Left: Model-Only Results (Model-Fit Uses Average Temperature) Right: Model with Discrepancy Term (Model-Fit Uses Temperature Taken from Each Data Point). Model is Solid Line and Dashed Line Represents 95% Uncertainty Bounds. α_x is the Ratio of Component x to CO_2BOL

4.3.2.3 Full-Scale Model Results

After analysis of the parameters and sub-models finishes, the distributions for all 37 parameters are propagated through the full-scale model to determine the uncertainty in final model predictions. For the CO_2BOLs system, the full-scale model predicts 90% capture of CO_2 under normal operating conditions. Figure 4-11 shows the resulting distribution in CO_2 capture percent when the model parameters vary according to their posterior distributions with the same operating conditions as the base model; no discrepancy terms are included here. It is unsurprising that a novel solvent with limited data has a wide distribution in full-scale results. However, the results are still centered around 90% capture with some parameter values actually increasing the predicted percentage of CO_2 captured by the system under these operating conditions.

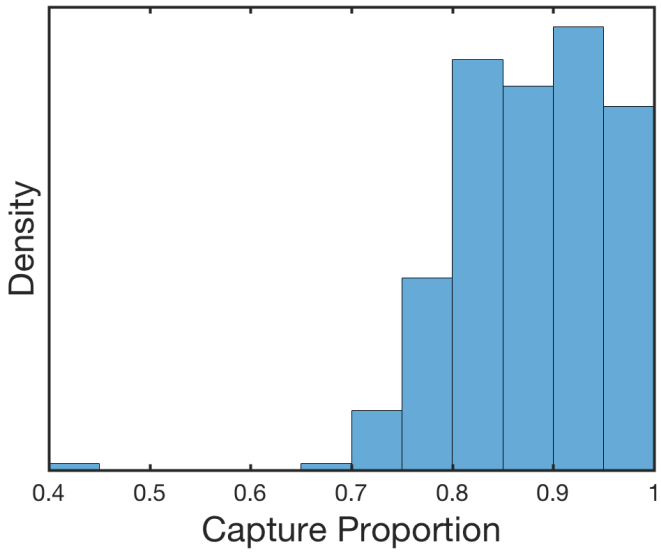

Figure 4-11: Carbon Capture Percent Distribution from Model Calibration Results

4.3.3 Summary

Uncertainty quantification is a powerful tool that provides valuable information about new models and their underlying data. This study has shown the steps necessary to perform uncertainty quantification for the novel CO_2BOLs system. Novel solvent systems often lack sufficient data to accurately model a full-scale simulation. However, model improvements require additional useful data. UQ results can help guide new data acquisition by determining regions of high uncertainty that would benefit from additional data. This can save time, effort, and money in achieving full-scale model results and can direct a project towards larger-scale experiments more quickly.

5 CONCLUSIONS

This research aims to address three issues: how to appropriately incorporate renewable resources into the electrical grid, how to continue using fossil fuels in an environmentally sustainable manner, and how to quickly improve simulations of carbon capture to prepare for pilot plant scale-up. This work suggests energy storage solutions, cryogenic carbon capture, and uncertainty quantification applied to solvent carbon capture systems to solve these issues. A summary of these solutions is provided in this section.

5.1 Energy Storage Solutions

A review on current and future energy storage technologies was conducted and key metrics were provided for each technology. Synergistic energy storage systems were compared to their dedicated counterparts and shown to be much more efficient. With the anticipated increase in renewable energy sources these energy storage technologies will play a prominent role in keeping the grid stable, responsive, and adaptable while incorporating many intermittent power sources. A cryogenic carbon capture technology was presented that can store energy for fossil-fuel-fired power plants while reducing carbon emissions.

These energy storage technologies will be critical in designing a “Smart Grid” for power distribution. This comparison between synergistic and dedicated storage systems is a first-of-its-kind analysis which argues that incorporating energy storage with infrastructure is key to storing

energy efficiently and effectively. Previous reviews[27-29, 31] commonly compare energy storage technologies by type, without mention of how these synergistic capabilities could increase efficiencies.

By ensuring that these energy storage technologies are synergistic the power loss of grid will be reduced and renewable sources can load follow. In addition to having a smarter grid these energy storage technologies can reduce or eliminate the need for backup power plants to be constructed alongside renewable power. Future work can be done to analyze the amount of power wasted from renewable sources and how the efficiency of the grid as a whole would be affected by the introduction of synergistic energy storage.

5.2 Carbon Capture

Current carbon capture technologies were introduced and compared with emphasis on cryogenic carbon capture, a major simulation endeavor of this work. The CCC-ECL process was shown to capture upwards of 90% of all CO_2 from the flue gas of a coal-fired power plant. The process was validated by comparing model predictions to data. The validation of the CCC-ECL model proved that the PR EOS was able to correctly predict SLE and VLE behavior. This validation was a significant step in confirming energy, economic, and performance results. Costing and sensitivity analyses were performed to confirm that the process is cheaper and less energy-intensive than rival carbon capture processes and provides additional advantages such as the energy storage solution. The CCC-ECL process was additionally shown to be versatile with its application to the transportation sector. This is a novel application of the CCC-ECL process, which can clean syngas of CO_2. When this process is used with biomass, it can even create carbon-negative transportation fuels.

This work is an important step forward for the CCC process as a whole, validating its results and showing its versatility. The CCC process can be applied to other streams, such as natural gas, with similar benefits. As a whole carbon capture can dramatically decrease the carbon footprint of fossil fuel-fired power plants and now even some fuel production processes. These simulations are promising and future work could include validation of the thermodynamic interactions of CO and the contact liquid for the syngas system. There is also work to be done to improve the model to properly handle SO_x and NO_x.

5.3 Uncertainty Quantification

Carbon capture with solvents has been studied for more than half a century and new solvents are constantly being developed to address the growing need for clean energy from fossil fuels. Uncertainty quantification is a statistical tool that aims to reduce the time for development of these new solvents from bench scale to pilot scale. UQ was applied to two solvent systems and the methodology was presented. UQ showed weaknesses in the model where additional data could be collected to reduce uncertainty. UQ also constructed discrepancy functions which were used to reduce uncertainty in the model by accounting for error inherent to the model. Results were shown at both the sub-model and full-model levels.

A UQ analysis of this scale has not previously been conducted on novel carbon capture systems. The splitting of data groups, necessary due to the number of parameters, was an innovative application of UQ techniques that led to a successful full-scale analysis. This work is also a unique application of discrepancy functions, which are able to reduce model error in carbon capture systems, something often overlooked in full-scale process analysis.

Future work would include an intuitive way to interface a discrepancy function into Aspen Plus to improve overall model uncertainty. Additionally work could be done on a more open system to explore how fully incorporating all sub-models into the analysis would affect full-scale model results. The techniques used here are not solely for use in carbon capture modeling, they can be applied to any model of any process to quantify the uncertainty in the model predictions.

6 BIBLIOGRAPHY

1. *International Energy Outlook 2017*, US Energy Information Administration, 2017.

2. *BP Statistical Review of World Energy June 2017*, BP, 2017.

3. United Nations, *World Population Prospects: The 2017 Revision*, New York, 2017.

4. WorldBank, PovcalNet: the on-line tool for poverty measurement developed by Development Research Group of the World Bank, http://iresearch.worldbank.org/PovcalNet/povDuplicateWB.aspx, (accessed August 17, 2017).

5. EIA, World energy demand and economic outlook, http://www.eia.gov/forecasts/ieo/world.cfm).

6. International Energy Agency, *World Energy Outlook 2012*, Paris, France, 2012.

7. BBC, Hundreds of millions without power in India, http://www.bbc.co.uk/news/world-asia-india-19060279, (accessed March 7, 2013).

8. K. H. LaCommare and J. H. Eto, *Understanding the Cost of Power Interruptions to U.S. Electricity Consumers*, Lawerence Berkeley National Laboratory, Berkeley, CA, 2004.

9. U. S. E. I. Administration, *Monthly Energy Review - Transportation Sector Energy Consumption*, U.S. Energy Information Administration, 2018.

10. U. S. E. I. Administration, *Monthly Energy Review*, U.S. Energy Information Administration, 2018.

11. U. S. E. I. Administration, *2017 International Energy Outlook*, U.S. Energy Information Administration, 2017.

12. P. Gładysz and A. Ziębik, *Biomass and Bioenergy*, 2016, **85**, 109-118.

13. U.S. Energy Information Administration, *Annual Energy Outlook 2017*, 2017.

14. I. E. Agency, *Key World Energy Statistics*, 2017.

15. International Energy Agency, *Solar Energy Perspectives*, International Energy Agency, Paris, France, 2011.

16. EIA, *International Energy Outlook 2017*, 2017.

17. U. S. E. I. Administration, *Levelized Cost and Levelized Avoided Cost of New Generation Resources in the Annual Energy Outlook 2017*, U.S. Energy Information Administration, 2017.

18. GE Energy, *Western Wind and Solar Integration Study*, National Renewable Energy Laboratory, 2010.

19. U.S. Energy Information Administration, *Annual Energy Outlook 2013*, 2013.

20. Compressed Air Energy Storage (CAES), http://energystorage.org/compressed-air-energy-storage-caes, (accessed 01/23/2019).

21. Advanced Adiabatic Compressed Air Energy Storage (AA-CAES), http://energystorage.org/advanced-adiabatic-compressed-air-energy-storage-aa-caes, (accessed 01/23/2019).

22. N. M. Jubeh and Y. S. H. Najjar, *Applied Thermal Engineering*, 2012, **44**, 85-89.

23. B. Elmegaard and W. Brix, Novi Sad, Serbia, 2011.

24. I. Gyuk, S. Eckroad, L. Mears, H. Gotschall, H. Kamath and T. Key, *EPRI Report*, 2003, **1001834**.

25. Isothermal CAES, http://energystorage.org/energy-storage/technologies/isothermal-caes, (accessed 01/23/2019).

26. SustainX Inc. Isothermal Compressed Air Energy Storage, https://www.smartgrid.gov/project/sustainx_inc_isothermal_compressed_air_energy_storage.html, (accessed 1/23/2019, 2019).

27. F. S. Barnes, Levine, Jonah G, *Large Energy Storage Systems*, CRC Press, Boca Raton, FL, USA, 2011.

28. H. Chen, T. N. Cong, W. Yang, C. Tan, Y. Li and Y. Ding, *Progress in Natural Science*, 2009, **19**, 291-312.

29. I. Hadjipaschalis, A. Poullikkas and V. Efthimiou, *Renewable and Sustainable Energy Reviews*, 2009, **13**, 1513-1522.

30. R. B. Schainker, 2004.

31. J. Kondoh, I. Ishii, H. Yamaguchi, A. Murata, K. Otani, K. Sakuta, N. Higuchi, S. Sekine and M. Kamimoto, *Energy Conversion and Management*, 2000, **41**, 1863-1874.

32. E. Drury, P. Denholm and R. Sioshansi, *Energy*, 2011, **36**, 4959-4973.

33. H. M. Kim, J. Rutqvist, D. W. Ryu, B. H. Choi, C. Sunwoo and W. K. Song, *Applied Energy*, **92**.

34. T. M. Pavlović, I. S. Radonjić, D. D. Milosavljević and L. S. Pantić, *Renewable and Sustainable Energy Reviews*, 2012, **16**, 3891-3902.

35. M. Schuller, F. Little, D. Malik, M. Betts, Q. Shao, J. Luo, W. Zhong, S. Shankar and A. Padmanaban, *Molten Salt-Carbon Nanotube Thermal Energy Storage for Concentrating Solar Power Systems Final Report*, Report DOE/GO18154; TRN: US201209%%258, 2012.

36. Z. Yang and S. V. Garimella, *Solar Energy*, 2010, **84**, 974-985.

37. N. R. E. Laboratory, Concentrating Solar Power Projects, https://www.nrel.gov/csp/solarpaces/index.cfm, (accessed August 18, 2017, 2017).

38. R. Pitz-Paal, A. Amin, M. O. Bettzuge, P. Eames, G. Flamant, F. Fabrizi, J. Holmes, A. Kribus, H. van der Laan, C. Lopez, F. G. Novo, P. Papagiannakopoulos, E. Pihl, P. Smith and H.-J. Wagner, *Journal of Solar Energy Engineering*, 2012, **134**, 024501-024506.

39. D. Ray, M. Edgar, K. Chisman and B. Emms, *Journal of Solar Energy Engineering*, 2005, 109-117.

40. J. E. Pacheco and R. Gilbert, Maui, Hawaii, 1999.

41. U. Herrmann, B. Kelly and H. Price, *Energy*, 2004, **29**, 883-893.

42. Z. Yang and S. V. Garimella, *Applied Energy*, 2013, **103**, 256-265.

43. X. Yang, X. Yang, J. Ding, Y. Shao, F. G. F. Qin and R. Jiang, *Applied Thermal Engineering*, 2012, **48**, 24-31.

44. H. Price, *National Renewable Energy Laboratory. January*, 2003, **3**.

45. S. Hameer and J. L. Van Niekerk, *Energy Procedia*, 2016, **93**, 25-30.

46. D. Cocco and F. Serra, *Energy*, 2015, **81**, 526-536.

47. Highview-Power, Liquid Air Process, http://www.highview-power.com/wordpress/wp-content/uploads/2012/08/process.jpg, (accessed February 4, 2013).

48. M. J. Jensen, C. S. Russell, D. Bergeson, C. D. Hoeger, D. J. Frankman, C. S. Bence and L. L. Baxter, *International Journal of Greenhouse Gas Control*, 2015, **42**, 200-212.

49. 9410736, 2012.

50. F. Fazlollahi, A. Bown, E. Ebrahimzadeh and L. L. Baxter, *Energy*, 2016, **103**, 369-384.

51. F. Fazlollahi, A. Bown, E. Ebrahimzadeh and L. L. Baxter, *Energy*, 2015, **90**, 244-257.

52. A. Sayre, D. Frankman, A. Baxter, K. Stitt and L. Baxter, 2017.

53. F. Fazlollahi, S. Saeidi, M. S. Safdari, M. Sarkari, J. J. Klemes and L. L. Baxter, *Energy Technol-Ger*, 2017, **5**, 1588-1598.

54. L. Baxter, P. Terrien, P. Tessier and C. Hoeger, *Journal*, 2017.

55. F. Fazlollahi, A. Bown, S. Saeidi, E. Ebrahimzadeh and L. L. Baxter, *Applied Thermal Engineering*, 2016, **109**, 775-788.

56. F. Fazlollahi, A. Bown, E. Ebrahimzadeh and L. L. Baxter, *Energy*, 2016, **103**, 369-384.

57. E. Ebrahimzadeh, P. Wilding, D. Frankman, F. Fazlollahi and L. L. Baxter, *Applied Thermal Engineering*, 2016, **93**, 1006-1019.

58. E. Ebrahimzadeh, P. Wilding, D. Frankman, F. Fazlollahi and L. L. Baxter, *Energy*, 2016, **96**, 545-560.

59. S. M. Safdarnejad, L. Kennington, L. L. Baxter and J. D. Hedengren, 2015.

60. S. M. Safdarnejad, J. D. Hedengren and L. L. Baxter, *Applied Energy*, 2015, **149**, 354-366.

61. S. M. Safdarnejad, J. Hedengren and L. Baxter, *American Institute of Chemical Engineers (AIChE)*, 2015.

62. F. Fazlollahi and L. L. Baxter, Salt Lake City, UT, 2015.

63. F. Fazlollahi and L. L. Baxter, presented in part at the International Conference on Green Energy & Expo, Orlando, FL, September 21-23, 2015.

64. F. Fazlollahi and L. L. Baxter, Salt Lake City, UT, 2015.

65. F. Fazlollahi and L. L. Baxter, Salt Lake City, UT, 2015.

66. F. Fazlollahi and L. Baxter, *EM: Air and Waste Management Association's Magazine for Environmental Managers*, 2015, **65**, 28-35.

67. E. Ebrahimzadeh, P. Wilding, D. Frankman, F. Fazlollahi and L. L. Baxter, Salt Lake City, UT, 2015.

68. L. L. Baxter, *Cornerstone*, 2015, **3**, 53-56.

69. J.-h. K. Young-myung Yang, Heung-seok Seo, Kangwon Lee, Ihn-soo Yoon, *Journal*, 2006.

70. B. Ameel, C. T'Joen, K. De Kerpel, P. De Jaeger, H. Huisseune, M. Van Belleghem and M. De Paepe, *Applied Thermal Engineering*, 2013, **52**, 130-140.

71. Environmental Protection Agency, *Journal*, 2014, 34829 -34958.

72. J. Kislear, presented in part at the Research Experience in Carbon Sequestration, Birmingham, AL, 2014.

73. D. C. Miller, J. T. Litynski, L. A. Brickett and B. D. Morreale, *AIChE Journal*, 2016, **62**, 2-10.

74. D. Berstad, R. Anantharaman and P. Nekså, *International Journal of Refrigeration*, 2013, **36**, 1403-1416.

75. J. Davison and K. Thambimuthu, *Proceedings of the Institution of Mechanical Engineers, Part A: Journal of Power and Energy*, 2009, **223**, 201-212.

76. T. E. Rufford, S. Smart, G. C. Y. Watson, B. F. Graham, J. Boxall, J. C. D. da Costa and E. F. May, *J Petrol Sci Eng*, 2012, **94-95**, 123-154.

77. J. Wilcox, R. Haghpanah, E. C. Rupp, J. He and K. Lee, *Annual Review of Chemical and Biomolecular Engineering*, 2014, **5**, 479-505.

78. K. Gerdes, *Journal*, 2014.

79. J. Ciferno, *Pulverized Coal Oxycombustion Power Plants*, NETL, 2008.

80. D. E. Herzog H, Tester J, Rosenthal R. , *A research needs assessment for the capture, utilization and disposal of carbon dioxide from fossil fuel-fired power plans.* , Massachusetts Institute of Technology, Energy Laboratory, 1993.

81. A. Gopan, B. M. Kumfer, J. Phillips, D. Thimsen, R. Smith and R. L. Axelbaum, *Applied Energy*, 2014, **125**, 179-188.

82. N. Berguerand and A. Lyngfelt, *Fuel*, 2008, **87**, 2713-2726.

83. P. Cho, T. Mattisson and A. Lyngfelt, *Fuel*, 2004, **83**, 1215-1225.

84. L.-S. Fan, L. Zeng, W. Wang and S. Luo, *Energ Environ Sci*, 2012, **5**, 7254-7280.

85. L.-S. Fan, presented in part at the NETL CO2 Capture Technology Meeting, Pittsburgh, PA, 2012.

86. A. Tong, S. Bayham, M. V. Kathe, L. Zeng, S. Luo and L.-S. Fan, *Applied Energy*, 2014, **113**, 1836-1845.

87. National Energy Technology Laboratory, *Advanced Carbon Dioxide Capture R&D Program: Technology Update*, U. D. o. Energy, 2013.

88. M. H. L. Zaman, Jay, *Korean J Chem Eng*, 2013, **30**, 1497-1526.

89. A. Skorek-Osikowska, K. Janusz-Szymańska and J. Kotowicz, *Energy*, 2012, **45**, 92-100.

90. E. Sanchez Fernandez, E. L. V. Goetheer, G. Manzolini, E. Macchi, S. Rezvani and T. J. H. Vlugt, *Fuel*, 2014, **129**, 318-329.

91. F. Porcheron, A. Gibert, M. Jacquin, P. Mougin, A. Faraj, A. Goulon, P.-A. Bouillon, B. Delfort, D. Le Pennec and L. Raynal, *Energy Procedia*, 2011, **4**, 15-22.

92. F. Morton, R. Laird and J. Northington, *Energy Procedia*, 2013, **37**, 525-539.

93. Y. Le Moullec and M. Kanniche, *International Journal of Greenhouse Gas Control*, 2011, **5**, 727-740.

94. L. Duan, M. Zhao and Y. Yang, *Energy*, 2012, **45**, 107-116.

95. S. M. Cohen, G. T. Rochelle and M. E. Webber, *International Journal of Greenhouse Gas Control*, 2012, **8**, 180-195.

96. Z. Amrollahi, P. A. M. Ystad, I. S. Ertesvåg and O. Bolland, *International Journal of Greenhouse Gas Control*, 2012, **8**, 1-11.

97. M. E. Boot-Handford, J. C. Abanades, E. J. Anthony, M. J. Blunt, S. Brandani, N. Mac Dowell, J. R. Fernandez, M.-C. Ferrari, R. Gross, J. P. Hallett, R. S. Haszeldine, P. Heptonstall, A. Lyngfelt, Z. Makuch, E. Mangano, R. T. J. Porter, M. Pourkashanian, G. T. Rochelle, N. Shah, J. G. Yao and P. S. Fennell, *Energ Environ Sci*, 2014, **7**, 130-189.

98. National Energy Technology Laboratory, *Journal*, 2013, **1**.

99. BD3 Status Update: December 2018, https://www.saskpower.com/about-us/our-company/blog/bd3-status-update-december-2018, 2019).

100. M. Nelson, R. Rush, D. Madden, T. Pinkston and L. Lunsford, *Kemper County IGCCTM Project Preliminary Public Design Report*, 2012.

101. M. Ishibashi, H. Ota, N. Akutsu, S. Umeda, M. Tajika, J. Izumi, A. Yasutake, T. Kabata and Y. Kageyama, *Energy Conversion and Management*, 1996, **37**, 929-933.

102. E. Chabanon, D. Roizard and E. Favre, *Chemical Engineering Science*, 2013, **87**, 393-407.

103. M. Gazzani, D. M. Turi, A. F. Ghoniem, E. Macchi and G. Manzolini, *International Journal of Greenhouse Gas Control*, 2014, **25**, 62-78.

104. M. Sjardin, K. Damen and A. Faaij, *Energy*, 2006, **31**, 2523-2555.

105. P. Shao, M. M. Dal-Cin, M. D. Guiver and A. Kumar, *Journal of Membrane Science*, 2013, **427**, 451-459.

106. C. A. Scholes, M. T. Ho, A. A. Aguiar, D. E. Wiley, G. W. Stevens and S. E. Kentish, *International Journal of Greenhouse Gas Control*, 2014, **24**, 78-86.

107. D. Clodic, R. El Hitti, M. Younes, A. Bill and F. Casier, Alexandria, Virginia, 2005.

108. X. Pan, D. Clodic and J. Toubassy, *Greenhouse Gases: Science and Technology*, 2013, **3**, 8-20.

109. M. J. Tuinier, M. van Sint Annaland, G. J. Kramer and J. A. M. Kuipers, *Chemical Engineering Science*, 2010, **65**, 114-119.

110. A. Castrogiovanni, V. Balepin, A. Robertson and B. Calayag, Pittsburgh, PA, 2012.

111. S. E. Solutions, Cryogenic Carbon Capture: Additional Benefits, https://sesinnovation.com/technology/carbon_capture/#additionalbenefits, (accessed 1/14/2019, 2019).

112. E. A. Chukwudeme and A. A. Hamouda, *Energies*, 2009, **2**, 714-737.

113. G. Chen, X. Wang, Z. Liang, R. Gao, T. Sema, P. Luo, F. Zeng and P. Tontiwachwuthikul, *Energy Procedia*, 2013, **37**, 6877-6884.

114. K. Su, X. Liao, X. Zhao and H. Zhang, *Energy & Fuels*, 2013, **27**, 378-386.

115. B. J. Nielson, Master of Science, Brigham Young University, 2013.

116. L. L. Johnson and G. Renaudin, *Journal Name: Oil and Gas Journal; Journal Volume: 94; Journal Issue: 47; Other Information: PBD: 18 Nov 1996*, 1996, Medium: X; Size: pp. 31-36.

117. *Journal*, 1991-2014, **1-15**.

118. Sustainable Energy Solutions: Demonstrations, https://sesinnovation.com/technology/demonstrations/, (accessed 1/12/2019, 2019).

119. N. E. T. L. US Department of Energy, *Pulverized Coal Oxycombustion Power Plants Volume 1: Bituminous Coal to Electricity: Revision 2*, 2008.

120. K. E. Hatfield, L. D. Smoot, R. L. Coates, L. L. Baxter, presented in part at the 28th Oil Shale Symposium, Golden, Colorado, USA, 2008.

121. D. Serpa, CO2 EMISSIONS FROM REFINING GASOLINE, http://www.afteroilev.com/Pub/CO2_Emissions_from_Refining_Gasoline.pdf).

122. Y. Man, S. Yang, D. Xiang, X. Li and Y. Qian, *Journal of Cleaner Production*, 2014, **71**, 59-66.

123. R. Datta, M. A. Maher, C. Jones and R. W. Brinker, *Journal of Chemical Technology & Biotechnology*, 2011, **86**, 473-480.

124. T. Kandaramath Hari, Z. Yaakob and N. N. Binitha, *Renewable and Sustainable Energy Reviews*, 2015, **42**, 1234-1244.

125. M. Specht, *International Journal of Hydrogen Energy*, 1998, **23**, 387-396.

126. A. B. M. S. Hossain, A. Salleh, A. N. Boyce, P. chowdhury and M. Naqiuddin, *American Journal of Biochemistry and Biotechnology*, 2008, **4**, 250-254.

127. NETL, Alternatives/Supplements to Coal - Feedstock Flexibility, http://www.netl.doe.gov/research/coal/energy-systems/gasification/gasifipedia/biomass).

128. P. Šimáček, D. Kubička, I. Kubičková, F. Homola, M. Pospíšil and J. Chudoba, *Fuel*, 2011, **90**, 2473-2479.

129. M. Lapuerta, M. Villajos, J. R. Agudelo and A. L. Boehman, *Fuel Processing Technology*, 2011, **92**, 2406-2411.

130. H. T. Mikkonen S, Kuronen M,Saikkonen PHVO, *Hydrotreated vegetable oil—a premium renewable biofuel for diesel engines*, Neste, 2012.

131. L. M. Aatola H, Sarjovaara T,Mikkonen S, *Hydrotreated vegetable oil (HVO) as a renewable diesel fuel: trade-off between NOx, particulate emission and fuel consumption of a heavy duty engine*, SAE international, 2008.

132. O. D. Hileman JI, Bartis JT,Wong HM,Donohoo PE,Weiss MA, *Near-Term Feasibility of Alternative Jet Fuels*, 2009.

133. Y. Gong, O. Kaario, A. Tilli, M. Larmi and F. X. Tanner, 2010, **1**.

134. R. Arvidsson, S. Persson, M. Fröling and M. Svanström, *Journal of Cleaner Production*, 2011, **19**, 129-137.

135. H. Zhao, G. Song, L. Shen and Y. Yu, *Energy & Fuels*, 2012, **26**, 2934-2941.

136. N. Siefert, D. Shekhawat, S. Litster and D. Berry, *Energ Environ Sci*, 2012, **5**, 8660.

137. D. J. Roddy and P. L. Younger, *Energ Environ Sci*, 2010, **3**, 400.

138. V. Prabu and K. Geeta, *Energy*, 2015, **84**, 672-683.

139. Y. Jiang and D. Bhattacharyya, *Industrial & Engineering Chemistry Research*, 2016, **55**, 1677-1689.

140. H. An, T. Song, L. Shen, C. Qin, J. Yin and B. Feng, *International Journal of Hydrogen Energy*, 2012, **37**, 14195-14204.

141. A. W. Bhutto, A. A. Bazmi and G. Zahedi, *Progress in Energy and Combustion Science*, 2013, **39**, 189-214.

142. R. B. Anderson, 1984, **19**, 457-461.

143. M. E. Dry, *Catalysis Today*, 2002, **71**, 227-241.

144. H. Jahangiri, J. Bennett, P. Mahjoubi, K. Wilson and S. Gu, *Catal. Sci. Technol.*, 2014, **4**, 2210-2229.

145. I. C. Yates and C. N. Satterfield, *Industrial & Engineering Chemistry Research*, 1989, **28**, 9-12.

146. M. K. Gnanamani, W. D. Shafer, D. E. Sparks and B. H. Davis, *Catalysis Communications*, 2011, **12**, 936-939.

147. F. Pöhlmann and A. Jess, *Energy Technol-Ger*, 2016, **4**, 55-64.

148. C. G. Visconti, L. Lietti, E. Tronconi, P. Forzatti, R. Zennaro and E. Finocchio, *Applied Catalysis A: General*, 2009, **355**, 61-68.

149. D. H. Chun, H.-T. Lee, J.-I. Yang, H.-J. Kim, J. H. Yang, J. C. Park, B.-K. Kim and H. Jung, *Catalysis Letters*, 2012, **142**, 452-459.

150. B. G. Johnson, M. Rameswaran, M. D. Patil, G. Muralidhar and C. H. Bartholomew, *Catalysis Today*, 1989, **6**, 81-88.

151. K. M. Cook, H. D. Perez, C. H. Bartholomew and W. C. Hecker, *Applied Catalysis A: General*, 2014, **482**, 275-286.

152. NETL, *Cost and Performance Baseline for Fossil Energy Plants Volume 2: Coal to Synthetic Natural Gas and Ammonia*, 2011.

153. N. E. T. Laboratory, Carbon Capture Project Portfolio, https://www.netl.doe.gov/research/coal/carbon-capture/project-portfolio, (accessed Nov, 6th, 2017).

154. t. C. C. S. f. I. Impact, https://www.acceleratecarboncapture.org/, (accessed Nov 6th, 2017).

155. D. C. Miller, M. Syamlal, D. S. Mebane, C. Storlie, D. Bhattacharyya, N. V. Sahinidis, D. Agarwal, C. Tong, S. E. Zitney, A. Sarkar, X. Sun, S. Sundaresan, E. Ryan, D. Engel and C. Dale, *Annual Review of Chemical and Biomolecular Engineering*, 2014, **5**, 301-323.

156. D. S. Mebane, K. S. Bhat, J. D. Kress, D. J. Fauth, M. L. Gray, A. Lee and D. C. Miller, *Phys Chem Chem Phys*, 2013, **15**, 4355-4366.

157. D. S. Mebane, J. D. Kress, C. B. Storlie, D. J. Fauth, M. L. Gray and K. Li, *The Journal of Physical Chemistry C*, 2013, **117**, 26617-26627.

158. FOQUS: Framework for Optimization and Quantification of Uncertainty and Surrogates, https://github.com/CCSI-Toolset/FOQUS, 2019).

159. J. Sacks, W. J. Welch, T. J. Mitchell and H. P. Wynn, *Statist. Sci.*, 1989, **4**, 409-423.

160. W. J. Welch, R. J. Buck, J. Sacks, H. P. Wynn, T. J. Mitchell and M. D. Morris, *Technometrics*, 1992, **34**, 15-25.

161. S. Leary, A. Bhaskar and A. Keane, *Journal of Applied Statistics*, **30**, 585-598.

162. M. D. McKay, R. J. Beckman and W. J. Conover, *Technometrics*, **21**, 239-245.

163. B. Tang, *Journal of the American Statistical Association*, **88**, 1392-1397.

164. C. B. Storlie, W. A. Lane, E. M. Ryan, J. R. Gattiker and D. M. Higdon, *Journal of the American Statistical Association*, 2015, **110**, 68-82.

165. D. Higdon, J. Gattiker, B. Williams and M. Rightley, *Journal of the American Statistical Association*, 2008, **103**, 570-583.

166. M. C. Kennedy and A. O'Hagan, *Journal Of The Royal Statistical Society Series B-Statistical Methodology*, **63**, 425-450.

167. T. M. Holland, PhD Dissertation, Brigham Young University, 2017.

168. J. Gattiker, K. Myers, B. J. Williams, D. Higdon, M. Carzolio and A. Hoegh, in *Handbook of Uncertainty Quantification*, eds. R. Ghanem, D. Higdon and H. Owhadi, Springer International Publishing, Cham, 2017, DOI: 10.1007/978-3-319-12385-1_58, pp. 1867-1907.

169. P. Frailie, J. Plaza, D. Van Wagener and G. T. Rochelle, *Energy Procedia*, 2011, **4**, 35-42.

170. T. M. Holland, *Journal*, 2017, DOI: 10.2172/1367827.

171. M. D. Hilliard, PhD Dissertation, University of Texas at Austin, 2008.

172. B.-T. N. Nguyen, PhD, The University of Texas at Austin, 2013.

173. R. E. Dugas, PhD Dissertation, The University of Texas at Austin, 2009.

174. S. M. Fulk, PhD Dissertation, The University of Texas at Austin, 2016.

175. Q. Xu, PhD Dissertation, The University of Texas at Austin, 2011.

176. S. A. Freeman, PhD Dissertation, The University of Texas at Austin, 2011.

177. AspenTech, *Journal*, Help File.

178. C.-C. Chen, H. I. Britt, J. F. Boston and L. B. Evans, *AIChE Journal*, 1982, **28**, 588-596.

179. C.-C. Chen and L. B. Evans, *AIChE Journal*, 1986, **32**, 444-454.

180. B. Mock, L. B. Evans and C.-C. Chen, *AIChE Journal*, 1986, **32**, 1655-1664.

181. I. Peter Thompson Frailie, PhD Dissertation, The University of Texas at Austin, 2014.

182. K. S. Bhat, Holland, T., Marcy, P., Storlie, C.B. , unpublished work.

183. F. Zheng, D. J. Heldebrant, P. M. Mathias, P. Koech, M. Bhakta, C. J. Freeman, M. D. Bearden and A. Zwoster, *Energy & Fuels*, 2016, DOI: 10.1021/acs.energyfuels.5b02437.

184. D. C. Cantu, D. Malhotra, P. K. Koech, D. J. Heldebrant, F. Zheng, C. J. Freeman, R. Rousseau and V.-A. Glezakou, *Green Chemistry*, 2016, **18**, 6004-6011.

185. D. J. Heldebrant, P. K. Koech, V. A. Glezakou, R. Rousseau, D. Malhotra and D. C. Cantu, *Chem Rev*, 2017, **117**, 9594-9624.

186. D. J. Heldebrant, P. K. Koech, J. E. Rainbolt and F. Zheng, *Energy Procedia*, 2011, **4**, 216-223.

187. D. J. Heldebrant, P. K. Koech, J. E. Rainbolt, F. Zheng, T. Smurthwaite, C. J. Freeman, M. Oss and I. Leito, *Chemical Engineering Journal*, 2011, **171**, 794-800.

188. D. J. Heldebrant, P. K. Koech, R. Rousseau, V.-A. Glezakou, D. Cantu, D. Malhotra, F. Zheng, G. Whyatt, C. J. Freeman and M. D. Bearden, *Energy Procedia*, 2017, **114**, 756-763.

189. P. M. Mathias, K. Afshar, F. Zheng, M. D. Bearden, C. J. Freeman, T. Andrea, P. K. Koech, I. Kutnyakov, A. Zwoster, A. R. Smith, P. G. Jessop, O. G. Nik and D. J. Heldebrant, *Energ Environ Sci*, 2013, **6**.

190. P. M. Mathias, F. Zheng, D. J. Heldebrant, A. Zwoster, G. Whyatt, C. M. Freeman, M. D. Bearden and P. Koech, *ChemSusChem*, 2015, **8**, 3617-3625.

191. G. A. Whyatt, C. J. Freeman, A. Zwoster and D. J. Heldebrant, *Industrial & Engineering Chemistry Research*, 2016, **55**, 4720-4725.

192. G. A. Whyatt, A. Zwoster, F. Zheng, R. J. Perry, B. R. Wood, I. Spiry, C. J. Freeman and D. J. Heldebrant, *Industrial & Engineering Chemistry Research*, 2017, **56**, 4830-4836.

193. J. Zhang, I. Kutnyakov, P. K. Koech, A. Zwoster, C. Howard, F. Zheng, C. J. Freeman and D. J. Heldebrant, *Energy Procedia*, 2013, **37**, 285-291.

194. R. Billet and M. Schultes, *Trans. IChemE.*, 1999.